Integrated optical devices based on liquid crystals embedded in polydimethylsiloxane flexible substrates

Department of Information, Electronics and Telecommunication Engineering
PhD degree in Information and Communication Technology – XXXI Cycle

Luca Civita
ID number 799451

Thesis Advisor
Prof. Antonio d'Alessandro

A.A. 2018-2019

A thesis submitted in partial fulfillment of the requirements for the degree of Doctor of Philosophy in Information and Communication Technology

This page intentionally left blank

Per aspera sic itur ad astra

Summary

Introduction

The contribution of this thesis is to find possible solutions for the creation of interconnections and optical switches to be used in microoptofluidic systems in the frame of the research activities of the Optoelectronic laboratory of the Department of Information Engineering, Electronics and Telecommunications (DIET). The main goal is to explore a new technology for integrated optic based on a low cost technology to produce low driving power devices. Optofluidics is the science which links the field of photonics with microfluidics, for the creation of innovative and state-of-the-art devices. Liquid crystals (LC) can be used for optofluidic applications because they have the possibility to change without external mechanical actions, the average direction of the molecules through the application of electric fields, reorienting the crystal molecules in such a way as to alter their optical properties [1-2].

The research on LC is more than a century old, but only since the '80s of the past century these materials were employed in various fields, from flat panel displays used for televisions, tablets, and smartphones, to biomedical and telecommunication applications [3-5]. The results reported in this thesis include simulation, design and preliminary fabrication of optofluidic prototypes based on LC embedded in polydimethylsiloxane (PDMS) channels, defined as LC:PDMS, with co-planar electrodes to control LC molecular orientation and light propagation. Fabrication techniques which were used include microelectronic processes such as lithography, sputtering, evaporation, and electroplating. The simulations were performed through the combined use of COMSOL Multiphysics® and BeamPROP®. I used COMSOL Multiphysics® to determine the positioning

of the molecules in a LC:PDMS waveguide. The LC are the core through which light propagates in a PDMS structure. In addition to these simulations, I used COMSOL Multiphysics® to determine the orientation of the LC under the effect of an electric field [6-7] to create low-power optofluidic devices [8], [11]. I used BeamPROP® to explore the optical propagation of various optical devices such as: optical couplers, the zero gap optical coupler, and a multimodal interferometer. All these devices have been simulated through various combinations of geometries which will be extensively explained in the following chapters. The fabrication of prototypes was made in the Microelectronic Technologies laboratory of DIET. The optofluidic prototypes that I designed could be used in interconnection systems on biosensing devices for chemical or biological applications [10-11], wearable [12], or lab on chips [13], which are increasingly being applied in many research fields [14]. Many of these devices need to interface with electronics for processing signals coming from the interaction between the device with molecules, liquids or other biological substances. Moreover it is necessary to create flexible and biocompatible interfaces, whose features are not guaranteed in classic metal tracks. As it will be clear in the first chapter, metal interconnections must be designed with spatial, energy and throughput restrictions. To develop the optofluidic prototypes, I chose to use a combination of two materials for their commercial availability and ease of use: E7 and 5CB LC produced by Merck® as the transmissive medium and PDMS Sylgard 184 produced by Dow Corning® for the cladding [15-16]. The molecules of the LC are anisotropic, whose shape is elongated like that of a cigar. Under appropriate temperature conditions these molecules retain a state of aggregation in which, while retaining some mechanical properties of the

fluids, they have the characteristics of crystals such as birefringence or x-ray reflection. These properties are due to two factors that characterize the various phases of LC: the orientational and positional order that vary according to the temperature. E7 was used in its nematic mesophase. The material used for the cladding of my prototypes was PDMS, a thermosetting polymer, flexible, biocompatible, economical, easy to work, and suitable for the creation of optical and optofluidic devices due to its transparency.

The thesis is organized in six chapters whose contents are briefly outlined below:

- In the first chapter there is a brief description of optofluidics and the transport phenomena of the liquids in the microchannels. The essential parameters for a correct interpretation of the behavior of the materials in the devices will be defined. Some examples of microfluidic devices, Optofluidic Optical Components (OOC) will be mentioned.

- In the second chapter, LC's will be presented, along with their general characteristics and their behavior in the presence of electric fields. An overview of integrated optic devices based on LC will be reported.

- In the third chapter the experimental results will be presented concerning the fabrications and the technologies used to obtain electro-optical LC:PDMS waveguides.

- The fourth chapter will be dedicated to a brief description of COMSOL Multiphysics® and BeamPROP® simulators, and the implementation of the model of LC channels in PDMS both in 2D

and 3D. Also a brief description of Monte Carlo simulations based on Lebwohl-Lasher potential will be mentioned.

- In the fifth chapter an LC:PDMS optical directional coupler and the most significant results will be described.

- The sixth chapter is dedicated to the multimodal interferometer and its field of application, the theory behind this device and the results obtained from the simulations using the BeamPROP®

- In the conclusion, a brief recap of the results obtained in this thesis and future developments will be presented.

Chapter 1: Optofluidics

1.1 Overview

Optofluidics is the merging of two fields: microfluidics and photonics. Before an in-depth explanation of the advantages of this field, it is important to know the difference between metal and optical interconnections. The motivations of the development of optofluidic devices, but more in general of the optical ones, [17-19] are to be found in the big problems that currently afflict micro-electronics. Currently, the production of devices in VLSI CMOS technology has various problems including delays in synchronizing data from different electronic components through a generic clock, the increase in bandwidth, and the power dissipated by the copper tracks to carry the signals through the communication bus [20-25]. If optical components were used for connections in current microelectronic devices, many of these problems could be resolved. The advantages in using optical interconnections compared to metal interconnections are:

- the estimated time of arrival of an optical signal is a predictable and reliable approximation, because the light always travels at the same speed except for scattering phenomena within the guide [17-19],

- an optical signal does not need the synchronization circuits with the results to save energy, area, or design complexity [17-19],

- when optical channels are used for interconnections, there would not be energy absorption from the power supply so that the signal can be transmitted [17-19],

- light sources are insensitive to the phenomenon of electric cross-talk [17-19],

- there are no problems related to the temperature, contrary to the copper tracks in which the resistivity depends on the temperature itself. Above 100 ℃ there is an increase in the resistivity of the copper of about 40% and the rise time of an electric line is typically proportional to the resistance of the line [17-19],

- stability of the system when there are current peaks or voltage fluctuations that may come from the power supply circuit, which we must take into account in the electrical interconnections, since it is true that with the dimensions, the tensions cannot be the same as the currents, which do not scale like the dimensions of the power lines [17-19],

- through an anti-reflective coating placed around the guides, specifically the cladding, reflections and signal degradation can be avoided which cannot be in the electrical interconnections caused by capacitive loads. [17-19].

The term OOC, (optofluidic optical component), refers to a class of devices that use microfluidics to create optical devices through various and variable parameters. It is possible to obtain different characteristics of light propagation including transmission, absorption, and dispersion. All these parameters obviously depend on the choice of the combination between the refractive index of core, whether in liquid or solid form, and on the liquid or solid cladding. Applications of various examples of these devices can be found in fields ranging from Telecommunications with

experimental fiber guides [24] or in Medicine with equipment for virus analysis [25-27] such as for processes of electrophoresis [28].
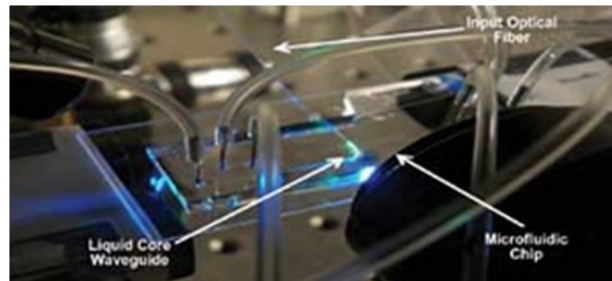
Fig. 1.1. Example of an optofluidic devices where we have more components interacting with each other. [19].

A key motivation for the production and study of optofluidic devices is their ease of manufacture through rapid prototyping and the flexibility in the design of more or less complex geometries combined with a simplicity in varying the refractive index which allows one to obtain infinite optical uses. Fig. 1.1. shows a prototype circuit where the interaction between several components of different natures such as optical fibers with a liquid core carry an optical signal so that it can react with molecules placed through channels perpendicular to the structure. In fig. 1.1 the signal from the optical fiber is routed on a micro-fluidic chip through an LCW (Liquid Core Waveguide) The relationship between light and matter gives rise to interaction mechanisms such as fluorescence, phosphorescence, Raman scattering, polarization, elastic refraction dispersion, second harmonic generation, or stimulated emission. These parameters can be obtained by combining the refractive index with the geometries of the devices, thanks to which it is possible to control the various devices statically or dynamically, by varying their optical properties while maintaining the same optical path. Results are obtained through the integration of an

incremental product between the physical path and the refractive index of the medium having as extreme the distance between the two points.

The advantages of optofluidics are varied. First of all, one related to the surface tension, since if an immiscible fluid comes into contact with the regular interfaces it does not alter its viscosity and density properties. Liquids can have an extremely affordable price compared to other materials used in microelectronics. In optofluidic devices, liquids can be replaced within the same device without having to be redesigned with clear savings on design and production costs. It is important to underline that geometric optimization can play a key role in the functionality of the devices but a greater contribution can be given by the application of an electric field, which can vary the optical properties of the material as long as it has ferroelectric properties.

Among the devices we can cite as examples are lasers, which can use a specific liquid [29] as an active medium, so that through it, an active medium in the cavity, a specific wavelength is selected. Most optofluidic devices are made of polymers, such as PDMS, because it's very ductile and transparent, whose properties will be analyzed in the following chapter. For example, dielectric guides in which optical signals can be passed [29-30], such as ring resonators in the fig. 1.2 a) and b), or for the development of micro-lenses for the construction of optofluidic microscopes. The dynamic properties of the fluids give the possibility to adjust, in a targeted way, the properties of the lens so that only the focusing power can be adapted, all obtained in a very small space as shown in fig. 1.3 a) and b).
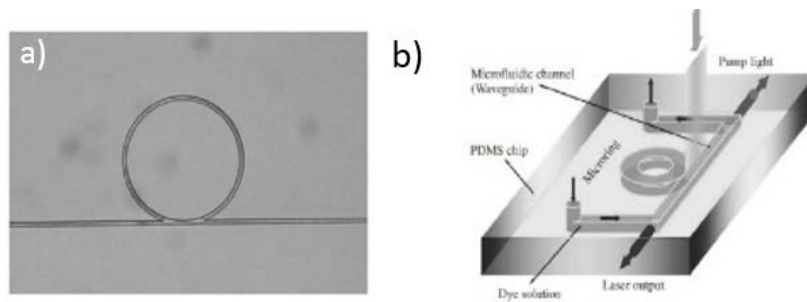
Fig. 1.2. In the picture a) we have a photograph taken through a microscope at S.E.M. of a fluid-optic resonator created on PDMS. In b) we have the scheme of operation of the same device [29].
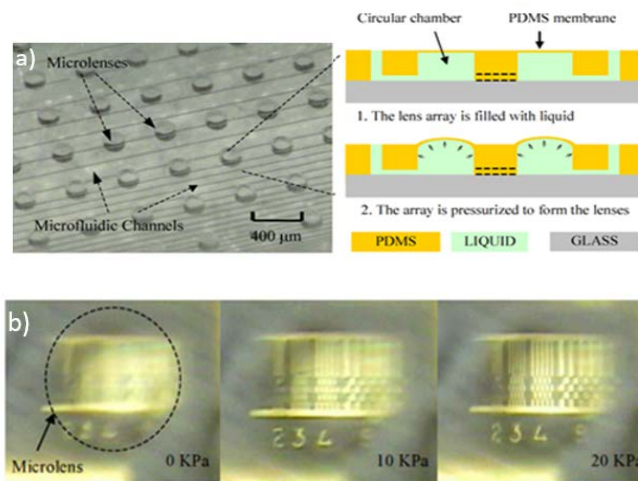
Fig. 1.3. a) Microscopic image of a microlens array, fabricated using a combination of glass, PDMS, and liquid. b) Variable focusing results two to a pressure change [29], [30-32].

The propagation of light can be explained through the principle of total internal reflection or TIR, mechanical confinement on which light propagation is based in the modern waveguides that can be replicated in the optofluidic waveguides. The transmission mechanism of light through the liquid core occurs through the TIR (Total Internal Reflection), in which the index of refraction must be lower than that of the core to avoid loss of the optical mode within the guide. Another advantage of liquid

substitution is that it can be done "off-chip", by replacing the liquid contained through an external tank or "on-chip", or using an integrated mixer that can allow the mixing of liquids with different refractive index. The refraction index of a material can be defined as the ratio between the speed of light in the vacuum or in the medium with the speed of the radiation of the medium. A list of liquids is shown in the table in fig. 1.4.

Name	Formula	n_D
Acetic acid [1]	CH_3COOH	1.3720
Acetone [1]	$(CH_3)_2CO$	1.3588
Benzene [1]	C_6H_6	1.5011
Bromine [1]	Br_2	1.6590
Butanoic acid [2]	$C_4H_8O_2$	1.3960
1-Butanol [2]	$C_4H_{10}O$	1.3990
Calcium chloride (aqueous, 1 mol kg^{-1}) [1]	$CaCl_2$-H_2O	1.3575
N,N-Dimethylformamide (DMF) [1]	C_3H_7NO	1.4306
Dimethyl sulfoxide (DMSO) [1]	$(CH_3)_2SO$	1.4170
1,2-Ethanediol (ethylene glycol) [1]	$(CH_2OH)_2$	1.4318
Ethanol [1]	C_2H_5OH	1.3611
Glycerol [1]	$CH_2OHCHOHCH_2OH$	1.4746
Hydrogen peroxide [1]	H_2O_2	1.4061
Methanol [1]	CH_3OH	1.3288
2-Propanol (isopropyl alcohol, ISO) [1]	$CH_3CHOHCH$	1.3776
Styrene [2]	C_8H_8	1.5440
Toluene [1]	C_7H_8	1.4961
Trichloroethylene [3]	C_2HCl_3	1.4760
Water [1]	H_2O	1.3330

Fig. 1.4. Table of refractive indices of the most common substances that can be used in optofluidic [29].

1.1.1 Equation of Flow

To understand how the behavior of a liquid can vary within a microscopic channel, one must consider the validity of the continuity approximation from macroscopic scales to microscopic scales and then study the principles of classical fluid mechanics in microscopic devices. This approximation uses the mean values characterizing the flow of the fluid which are taken into consideration instead of considering the single interactions that occur between the molecules of the fluid. The

incompressibility of liquids determines the fact that, according to the continuity equation, the flow must be constant in every section of the channel. If it has different sections, the equality is still valid $Q_1 = Q_2 = Q_i$. Since the flow can be expressed as the product of the area A of the cross section of the channel for the average velocity v_m of the fluid passing through this section it follows that:

$$Q_i = v_{m,i} \cdot A_i \qquad (1.1)$$

As the section decreases, the velocity of the fluid increases inversely proportionally, in order to maintain the constant flow as required by the continuity equation. Reynolds in 1883 determined that the critical velocity of a fluid, i.e. the velocity beyond which the fluid's motion regime changes is proportional to its viscosity η and is inversely proportional to its density ϱ and to the diameter d of the duct through which it flows:

$$v_c = \frac{k \cdot \eta}{\rho \cdot d} \qquad (1.2)$$

The proportionality constant k is about 2000 for many liquids. By rewriting the previous equation with the actual velocity of the fluid, the factor k is no longer a constant but a variable called the Reynolds number (Re which expresses the relationship between inertial and viscous forces. Depending on the Re, dimensionless, we distinguish between laminar regime and turbulent regime. Values above 2000 indicate turbulent regime and lower values laminar values. At the microscopic level, the flow is generally laminar, i.e. the flow is made up of many infinitesimal layers that flow with respect to each other without mixing. The flow, in the laminar regime,

is governed by the viscous forces and is of a stationary nature, that is, its velocity profile does not vary with time. Viscosity is the measurement of the resistance to the flow of a liquid, and its unit of measure is the product Pascal (Pa) per second (s), this quantity varies from fluid to fluid and with temperature. In the hypothesis of stationary motion, laminar flow and Newtonian fluid, the Poiseuille law is:

$$Q = (P_1 - P_2) \cdot \frac{\pi}{8} \cdot \frac{1}{\eta} \cdot \frac{R^4}{L} \tag{1.3}$$

$P_1 - P_2$ is the difference in pressure between the two ends of the channel section of length L and radius R with the viscosity η of the liquid. Due to the viscosity of the liquids and the friction of the latter against the walls of the channels, the flow does not have a velocity front $\frac{dv}{dy}$; where y represents the axis relative to the width of the channel, and x the axis relative to its length. The velocity has a uniform higher value in the middle and gradually lower as you approach the walls. This characteristic is peculiar to the laminar flow and the difference in velocity between the center and the boundaries is even more marked the more the channel has a small section. If the velocity of a flow in a conduit is gradually increased by decreasing its section, it will reach a critical value after which the flow will no longer be laminar but turbulent with vortexes and suction. In this case the Poiseuille law is no longer valid. Another physical phenomenon widely used in microfluidic devices is diffusion or a stochastic process in which the molecules, due to the thermal agitation, are guided from one region to another of the microchannel, arranging themselves homogeneously in the volume of interest. In microchannels, diffusion

transport is often combined with the convective flow of the bulk fluid. The ratio between mass transfer by convection and diffusion is calculated through the Sherwood number (dimensionless):

$$Sh = k \cdot \frac{d}{D} \tag{1.4}$$

where k is the mass transfer coefficient, D is the diffusion coefficient, d represents the diameter of the channel. As microfluidic channels are characterized by a small d, it turns out that the diffusion transport is dominant over that by convection. A further dimensionless parameter useful for understanding the behavior of a fluid within a microchannel is the Bond number which allows to evaluate the surface tension that is dominant with respect to the gravitational force at the interface with the fluid:

$$B_0 = \frac{\Delta\rho \cdot g \cdot L^2}{\gamma} \tag{1.5}$$

where $\Delta\rho$ is the density difference at the interface, g is the gravitational acceleration, L is the characteristic dimension of the channel, γ is the surface tension. Fluids subject to surface tension and gravity can be described through the capillary length:

$$\lambda = \left[\frac{\gamma}{(\Delta\rho \cdot g)} \right] \tag{1.6}$$

therefore, it appears that $B_0 = \frac{L^2}{\lambda^2}$. Very small values for the Bond number imply that the surface tension has a dominant value with respect to the gravitational force. Through the manipulation of the surface tension forces it is however possible to implement and control the transport of the fluid. To complete the brief description of the principles of microfluidics, the liquid flow at the micro scale and nanofluidic devices can be described by the mechanics and the Navier-Stokes equations, that are used in traditional fluid mechanics. The equations of continuity and the Navier-Stokes for an incompressible Newtonian fluid with constant fluid are as follows:

$$\nabla \cdot v = 0 \tag{1.7}$$

$$\rho(\frac{\partial v}{\partial t} + v \cdot \nabla v) = -\nabla p + \eta \nabla^2 v \tag{1.8}$$

In the 1.9 b the elimination of the time-dependence define, physically, the transient period when the flow conditions change rapidly, and in many cases, it can be assumed that the flow response is instantaneous [30].

1.2 Optofluidic Optical Components

1.2.1 PDMS

PDMS has been the most widely used material in the research and development of microfluidics. PDMS is an optically transparent elastomer whose stiffness can be controlled from very soft (easily deformed by finger pressure) to much stiffer. The fabrication of systems of microchannels in

PDMS is particularly straightforward. The use of PDMS as a material allows rapid prototyping of devices, and facilitates the demonstration and the testing of new concepts. The physical and chemical properties of PDMS also make possible the fabrication of devices with a useful range of functions, ranging from molecular analysis to frequency-tunable lasing. PDMS is elastomeric and it has tunable Young's modulus typically around 750 kPa [28]. It deforms easily, conforms to surfaces, and PDMS is elastomeric, it is possible to form optical components whose dimensions can be tuned mechanically.

The surface of PDMS is hydrophobic as it contains repeating units of $-O-Si(CH_3)_2-$groups. By exposing it to oxygen or air plasma, this surface can be made hydrophilic. Exposure to plasma introduces silano (Si–OH) groups, and destroys methyl groups (Si–CH_3). PDMS can be wetted by aqueous, polar solvents, and eutectic gallium-indium, a liquid metal alloy. On standing, a hydrophilic, oxidized PDMS surface becomes hydrophobic, as the surface reconstructs and as non-crosslinked components of the pre-polymer bloom to the surface. It is possible to keep PDMS that has been plasma treated hydrophilic indefinitely by keeping the surfaces in contact with water or polar organic solvents. The silanol groups on the surface of PDMS allow it to react with a wide range of silanes (Si–R) that are terminated with important functional groups (i.e., R = NH_2, COOH, SH) [33].

By using different functional groups, it is possible to adjust the surface of PDMS to be hydrophilic or hydrophobic, or to introduce other reactive groups. Grafting a poly(ethylene glycol)di-(triethoxy)silane onto an oxidized PDMS surface makes the surface hydrophilic permanently, and reduces nonspecific adsorption of proteins. These modified polar surfaces

can, however, become hydrophobic again through blooming of mobile, nonpolar siloxanes. Application of a sol-gel coating may be more protective, but has not been extensively developed PDMS is compatible with water and most polar organic solvents (such as methanol and glycerol); it swells, however, in nonpolar organic solvents (such as pentane and chloroform), and will absorb nonpolar solutes from aqueous solutions.

To reduce the absorption of small molecules and the swelling by nonpolar organic solvents, one can modify PDMS with silica particles, or coat the surface with a glass-like layer using sol-gel chemistry. PDMS is nontoxic to proteins and cells. It is permeable to oxygen and carbon dioxide but only slowly permeable to water. It is therefore suitable for biological studies: for example, mammalian cells can be cultured on it directly. PDMS is optically transparent and has a refractive index around 1.41, and it has negligible birefringence. It is therefore possible to enclose optofluidic components in PDMS, and couple light through PDMS, with minimal loss due to absorption [31-32].

Commercially available PDMS, Silgard® 184, does, unfortunately, contain nanoparticles of silica that introduce unwanted scattering of light. In the devices we and others have fabricated, the thickness of PDMS for enclosure of microfluidic components is limited (usually < 1 cm), and thus scattering due to passage of light through PDMS does not cause significant loss during the coupling of light into and out of the devices. We have not identified a polymer that lacks these scatterers, and still possesses the other desirable qualities of PDMS. The Norland® optical adhesives (photocurable polyurethanes), for example, contain no scattering particles, but they are not soft, and cannot be processed the same way as PDMS. This

need for an elastomeric polymer with high optical transparency and easy scalability presents an opportunity for future research in material science. PDMS can be a conductive elastomer if nanoparticles of precious metals such as silver and gold, are dispersed in the polymer matrix. In this case the flexibility of the nanoparticles-PDMS composite is retained. However, the transparency of the materials is lost [33-36]. In fig. 1.5, a PDMS film with embedded gold nanoparticles [36].
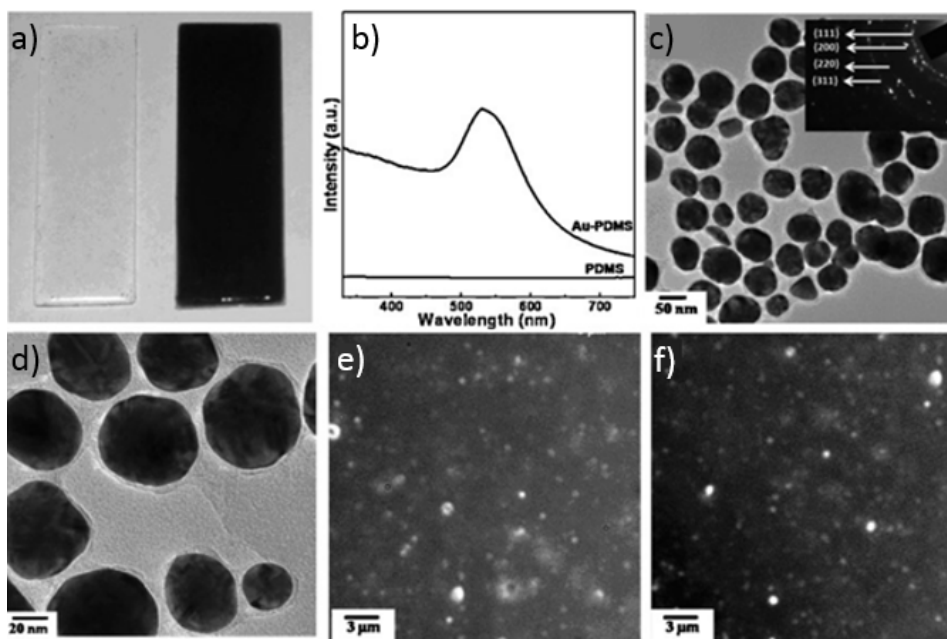
Fig. 1.5. a) PDMS plus nanoparticles of Au. b) UV spectra of the film. c) and d) TEM images of the gold nanoparticles formed in a PDMS matrix. In e) and f) is shown optical images of gold nanoparticles embedded in PDMS film [36].

To summarize, PDMS has attractive features that make it useful for a wide range of applications in laboratory, and for prototyping in research, though it may not be the ultimate material used in large-scale manufacturing [37-39].

1.2.2 Solid core and liquid cladding

A first example of an optofluidic device is the fabrication of a waveguide consisting of a solid core and a liquid cladding (SCLC) [29] represented in the fig. 1.6 below.
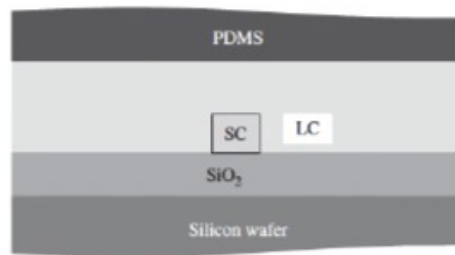
Fig. 1.6. Cross-section of a SCLC waveguide [29].

The fabrication of this guide takes place by placing successive layers of silicon. Starting with a wafer of Si, it is placed in the air and the recombination of pending ties with oxygen creating a thin layer SiO_2 on which subsequently another layer of silicon was deposited. Through a dry etching it's obtained a rectangular guide in silicon with a higher refractive index (n = 3) and surrounding it, there is LC (n = 1.60). Subsequently, a polydimethylsiloxane (PDMS) structure was created to cover the upper part and the side walls of the structure. The LC were filled by capillarity through the use of micro- fluidic pumps. The mechanism of propagation of the light beam in most of these structures is based on the principle of internal reflection. A small fraction of the light tends to disperse in these types of structures, called evanescent waves, due to the non-perfect relative cladding to the external liquid that can vary its index of refraction if subjected to great powers. Depending on the geometry and the combination of materials used in the guide, we can have single-mode or

multimode transmission, or in other words we have the fundamental way or its degenerations depending on the quasi TE or TM polarization that crosses the structure. The advantage of these structures is to have the core as a solid part, very easy to make and a geometry that can be scaled at will. In fig. 1.6 it is shown how, when the refractive index changes, a consistent variation of light propagation occurs in this type of guide. Obviously, the variation of the refractive index is due to multiple internal causes, that is, from the material itself, or from external factors, perhaps impurities introduced during the filling process.
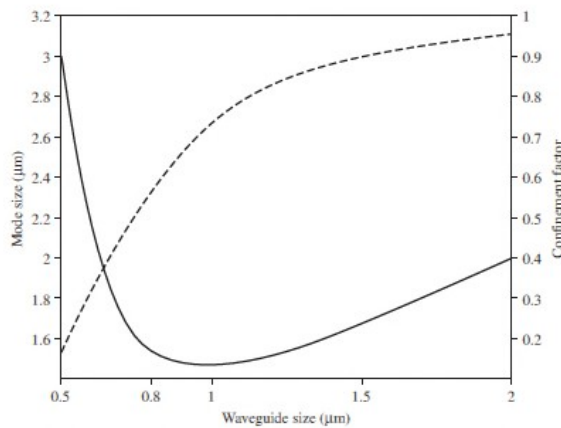
Fig. 1.7. Confinement of the guide mode according to the dimension of the core relative to a rectangular guide with the refractive index of the core n = 1.56 corresponds to the refractive index of the SU-8 surrounded by a liquid with refractive index n = 1.45, the wavelength of the light beam is 1.55 μm [29].

As can be seen from the fig. 1.7 we have that the confinement mode decreases from 95% of a 2 μm guide to an 18% with an increase of the overlap between the core and the liquid mode. This, however, comes at the expense of an increase in mode size to more than 3 μm because the waveguide becomes weakly guided.

1.2.3 Liquid core and solid cladding

As seen in the previous paragraph the disadvantage of the SCLC structures is related to the dispersion of the guided modes in the liquid that functions as a cladding structure, as showed in fig. 1.7. To ensure a solution to this problem, research groups are attempting to fabricate devices that use a liquid core (LCW) and solid cladding as shown in the fig. 1.8 [29]. These are prototypes very similar to the device of this thesis [37].
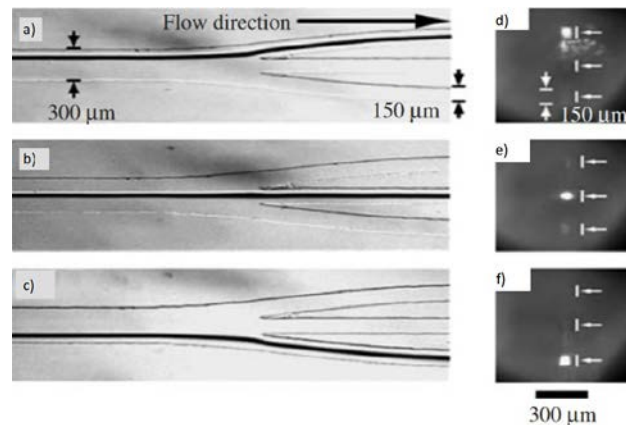
Fig. 1.8. Example of a three-channel optical switch using polymeric waveguides. Channels a), b), c) made up of PDMS are shown in which a contrast liquid, not used for optical transmission, has been introduced to show the individual channels. Next, d), e), f) optical myographies of the cross-section of the end of the micro-fluidic channels, while the white arrows indicate the position of the ends of the branches of the channel [31].

A different approach of LCW is the defined structure "Arrow", shown in fig. 1.9. The anti-resonant reflection wave guide (ARROW) [38-39], the border of light in the core is obtained through an interferential phenomenon in the cladding layers. Each of the cladding is designed appropriately to act as a highly reflective Fabry-Perot mirror at the specific

wavelength. Silicon nitride and silicon dioxide, first and second cladding respectively, are compatible with the standard processes widely used in microtechnology processes. By using the advantages of the integrated PDMS-based microfluidic chip to process the fluid sample, the authors demonstrated a LOD of 0.2 pfu/mL, comparable with other amplification-free methods like PCR analysis and more than four orders of magnitude lower than other chip-based approaches. Some uses of these structures are for biomolecular detection to distinguishing analyte signals from unwanted background. In this case and in contrast to the previous examples the waveguide does not base its operation on propagation according to the TIR theory but on a totally different approach due to the structure with which it is constructed. This guide is fabricated by superimposing several dielectric planes that perform the cladding function for which they are produced [38-39].
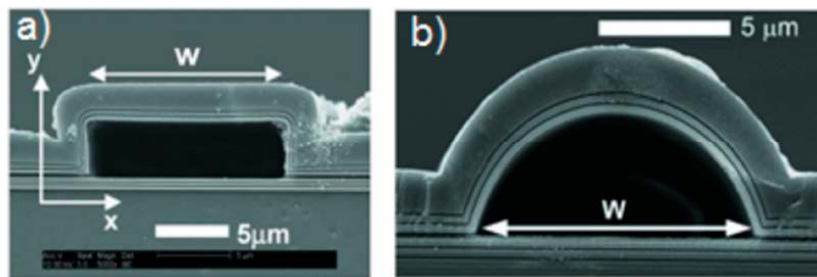

Fig 1.9. Pictures taken at SEM. Hollow-core ARROWs with a) rectangular and b) arch shaped cross-section [38-39].

1.2.4 Liquid Core and Liquid Cladding

In addition to the previous waveguides, L^2 (Liquid-Liquid optical devices) guides can be created, although they are not very widespread, and have undoubted advantages [40-44]. These devices are so called because they

consist of two or more channels in which the core and the cladding are liquid, fig. 1.10 a) and b). The rest of the device is made of polymers, to have an optical confinement, of the incoming beam thanks to the different indices of refraction of the liquids. The operation of these guides is based on the modification to the interface due to the variation of the flow between the two liquids which determines a variation of the path of the light beam inside the guide itself.
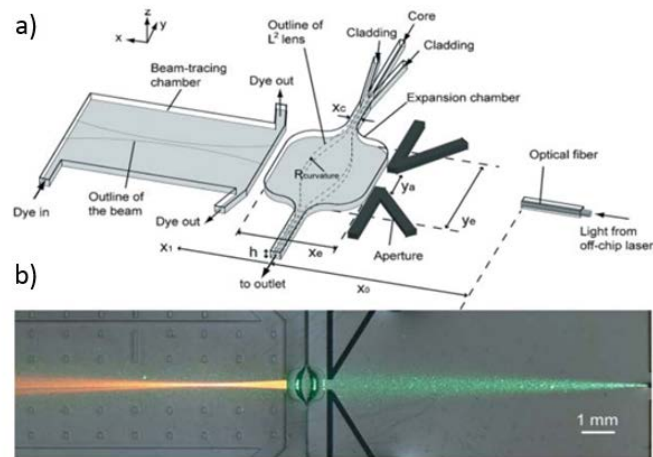
Fig. 1.10. a) Schematic representation of b) experimental setup for focusing light through liquid core and liquid cladding. The input light is at 633 nm and the aperture is formed by two channels filled with black ink after fabrication [27-28].

The waveguides are easily reconfigurable, due to the mixture composition of the medium can be reversibly tuned by adjusting the flow rates of the liquids or tunable in wavelength and intensity [47-49] to achieve the result expected. Unlike other types of optical guides, these do not require high precision manufacturing methods, since microfluidic systems are the same laminar flow that guarantees excellent fluidity between the interfaces. It is very easy to obtain the desired refractive index by carefully selecting the desired liquid thanks to the immiscibility of liquids and the extreme ease

of production of the channels, as they are produced, as shown in fig. 1.11 a) and b).
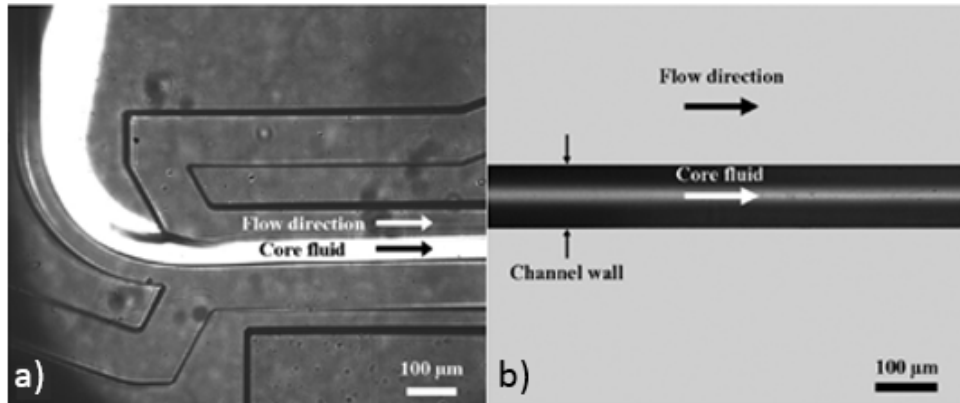
Fig. 1.11. a) Top view and b) side view of the microfluidic channel [27-28].

One of the common characteristics of the L^2 optofluidic devices is that of being able to replenish the liquids already present, since having lost their intrinsic characteristics or because they become incompatible due to use. This can be explained if lasers are used as light sources. After a few seconds, they can make the liquid unusable due to a "bleaching" of the same and consequent variation of the refractive index. To overcome this problem, a few sets of open channels are used to refill the liquids in order to maintain the operation of the device according to specifications. To redesign a device from scratch like the guides seen in the first two cases may not always be easy and risk-free. The switching time of liquids as already underlined is of the order of a few seconds, too slow for the current optical applications. As already pointed out in the previous points, it is not necessary to use a very high manufacturing process to obtain smooth surfaces in which the liquids must be infiltrated, since using flows with a low Reynolds coefficient, and there are no scattering problems between the liquid interfaces. If we examine the devices with liquid core and solid

cladding the only irregularities we can have are exclusively in the production of the channels in polymers.

Conclusions

Optofluidics is a rapidly growing field. The evolution of optics and microfluidics combinations are numerous and exciting to explore, we can reasonably expect this field to continue its rapid growth over the next decade. Optofluidics have brought about new and potentially better ways to build or use established optical structures and devices. The range of light-matter interaction mechanisms is remarkably broad, to name a few of these mechanisms such as fluorescence, phosphorescence, Raman scattering, polarization, elastic scattering, refraction, second harmonic generation, and stimulated emission. These mechanisms form the basis of optical sensing methods that are broadly used for chemical and biological sensing, because of their fast response and high specificity and sensitivity that are ideal for sensing applications [28].

Several studies concerning Arrow waveguides have revealed that the fundamental propagation loss (FPL) depends on the geometry. For instance, Testa et al. [42] have reported an FPL (at λ= 635 nm) of 10.56 dB/cm and 5.22 dB/cm for an Arrow guide cross section of 5 x 8 μm and 5 x 10 μm, respectively. D. Yin et al. [43] achieved an FPL equal to 0.26 dB/cm (at 633 nm and for a 4.5 μm^2 cross section). Finally, S. K. Fan et al. [44] have investigated the effect of core and cladding material concentrations on the FPL of L^2 waveguides (at 555 nm). Specifically, they employed γ-butyrolactone (GBL, n_{core}= 1.4341, ε_{core} = 39) as core medium, while different concentrations of R6G silicone oil ($n_{cladding}$= 1.401, $\varepsilon_{cladding}$ = 2.5) functioned as cladding liquid. Needless to say, the propagation loss turned out to increase as the concentration of the cladding liquid into the

core GBL is raised. Indeed, FPL values of 2.09, 2.33 and 2.68 dB/cm were measured for R6G concentration equal to 0.01, 0.1 and 1 mm, respectively.

Chapter 2: Liquid Crystals

2.1 Overview

LC were discovered at the end of the 19th century, thanks to studies performed by the Austrian botanist Reinitzer on cholesterol benzoate. He realized that the substance that he was examining, presented two different melting points. The first formation presented a rather translucent liquid phase, and a second characterization showed limpidity when the temperature was increased. From Reinitzer's experiments, it was clear that it was possible to have many types of phases, more commonly called mesophases, which define the properties of the LC as a function of temperature variation in correlation with the geometry of the molecule. In a crystalline solid, the atoms have a defined position. In an isotropic liquid, the molecules do not have positional order. In LC, the molecules are asymmetric and have a particular shape depending on the type of LC. If a sample is in the crystalline phase when it is heated, above a certain critical temperature, reaches the crystalline liquid mesophase. In this state, the three-dimensional positional order is lost partly or entirely while the molecules remain oriented towards a common direction [50].

2.2 Types of mesophase

LC are classified according to how they change their mesophases. If dissolved in a solvent at a given concentration, they are lyotropic but if mesophases are generated from temperature changes we have a thermotropic LC. In general, these LC have found important applications

in photonic and optoelectronic devices. Lyotropic ones are used in cosmetics and biological applications [51-52].

2.2.1 Thermotropic LC

The fundamental characteristic of LC is their geometric anisotropy, as shown in fig. 2.2. An example of a calamitic molecule is the 4-pentyl-4-cyanobiphenyl molecule (5CB) synthesized around the '70s and it has been widely used since it is chemically very stable and has a nematic phase at room temperature (25 °C). These molecules show a large electric dipole moment that aligns along the molecular axis of the crystal. This particularity makes them extremely susceptible to variations in electromagnetic fields and for this reason it is used for optoelectronic applications. The presence of a rigid and anisotropic central nucleus defines different optical properties. The achiral molecules, such as CB5, show a reflection symmetry, contrary to achiral molecules that have no reflection like CB15 [50]. Both of these types of LC are depicted in fig. 2.1.
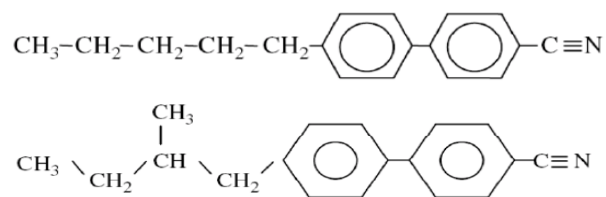

Fig 2.1. The structural formulas of the two molecules 5CB and CB15 are showns [50].

2.2.2 Main crystalline mesophases

The figure below shows various mesophases characterizing all the thermotropic LC as a function of temperature variations. The phases differ from each other for the positional and orientational order of the director's LC represented by the vector $\hat{n}$ named director. The molecules are arranged on a periodic lattice along three directions determined by three crystallographic vectors $\hat{a}$, $\hat{b}$, $\hat{c}$. The orientation of the molecules is referred as Cartesian coordinates $\hat{x}$, $\hat{y}$, $\hat{z}$, as shown in fig. 2.2 [50].
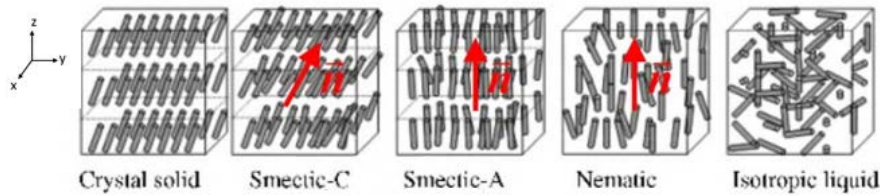
Fig. 2.2. Mesophasis of a calamitic LC. The director $\hat{n}$ defines the average orientation of the molecules of the LC [53].

2.2.3 Crystalline solid phase

It is characterized by having both a positional and an orientational order of crystalline solids and is the first phase in fig. 2.2.

2.2.4 Smectic C phase

This phase is generally indicated by the letters S_C in which molecules are arranged on overlapping layers, but the molecular average axes are aligned in such a way as to form an angle θ with the normal layers. The angle thus formed indicates that the inclination breaks the rotation symmetry. If $\hat{x}$ indicates the axis that is perpendicular to the director. The $\hat{x}$, and $\hat{y}$,

directions are no longer equivalent. As a consequence, the macroscopic properties of the LC can no longer be represented through a uniaxial axis but instead serve two axes, described from two tensors [50].

2.2.5 Smectic A phase

In this phase, indicated with the letters S_A, the molecule's centers of gravity are distributed on overlapping layers, and they are parallel to the plane $\widehat{xy}$,. The presence of these layers was observed during an X-ray analysis, in which the images produced Bragg peaks. This mesophase has a positional order compared to nematic LC where the molecules in each layer can move freely. This behavior is the same as a fluid, but molecules are not allowed to have transitions between one layer and another because in the nematic phase, there are no layers. The orientation of the molecules in a smectic phase presents a spatial periodicity along the z-axis perpendicular to the other layers and the molecules orient themselves along the direction parallel to the normal axis. Generally, the dimensions of these layers are of the order of some tens of angstroms and the viscosity of these materials is slightly higher than those of nematic LC and also do not have ferroelectric properties [50].

2.2.6 Nematic phase

In this configuration, conventionally indicated by the letter N, the gravity centers of the molecules are arranged randomly in space, in other terms, there is no positional order. The molecular axes are aligned along a common direction identified by the vector $\hat{n}$. The presence of a privileged direction, represented by the direction of the director's LC, defines the

average direction of all the molecules of the LC, making the system macroscopically anisotropic and uniaxial. The name of the parallel index refers to the refractive index of the LC when the polarized lightwave's axis is parallel to the director $\hat{n}$, and corresponds to the extraordinary index in a bulk sample of aligned LC. The index of refraction that is seen by a wave polarized perpendicular to the director $\hat{n}$, takes the name of perpendicular index that corresponds to the ordinary index in a bulk sample of aligned LC [50].

2.2.7 Isotropic phase

At this stage the centers of gravity of the molecules are randomly distributed, and therefore all the macroscopic properties such as electrical conductivity or magnetic permeability, are isotropic [50]. If the LC are used as dielectric medium, the isotropic phase is the only mesophase that can fill capillars since in a LC mesophase has a higher viscosity and density than water [53].

2.3 LC interaction with surfaces and modelization

2.3.1 Surface interaction

The molecules of LC tend to orient themselves along a common direction identified through the director $\hat{n}$. In the absence of interactions with external fields there are no privileged directions in space and the director's orientation can be indeterminate. The isotropy of space is broken only if external electric or magnetic fields are present, in this case the director orients himself along the direction that minimizes the energy. The free

energy per surface unit depends on the director's orientation and is minimal only at one or more privileged directions defined as easy axes. These two axes depend on the type of material with which it comes into contact. The orientation of the director in contact with the surface is determined through two angles: the zenith θ_s and the azimuth φ_s that respectively indicate the position perpendicular to the z axis and parallel to the contact surface's x axis as indicted in fig. 2.3.
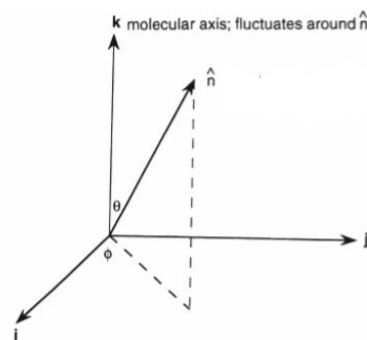
Fig. 2.3. Coordinate system defining the microscopic order parameter of a nematic LC molecule, in which i, j, k are the molecular axes, and $\hat{n}$ defines the average direction of LC alignment [50].

The orientation of the easy axes, on the other hand, is determined by two angles, θ_f and φ_f. If the medium in contact with the LC is an isotropic medium, such as glass or air, there are no preferred directions but the surface is uniquely identified by the vector $\hat{k}$ that is perpendicular to the surface. The interaction energy between LC and the contact medium depends only on the angle θ_s and must be independent of the angle φ_s, [50]. There can be three possible cases:

- energy is minimized if $\theta_s = \varphi_f = 0$. In this case, the director orients himself perpendicular to the surface. The configuration is called homeotropic [50].

- energy is minimized by $\theta_s = \varphi_f$ with $0 < \theta_f < 90$ °. The director is oriented along any direction that can define the easy angle θ_f with the normal to the surface. The director will then orient himself preferentially along any direction that lies on a cone that has an opening of $2\theta_f$. This configuration is defined as conical [50].

- the minimum energy for $\theta_s = \theta_f = 90$ °. The director is oriented along any direction in the plane of the surface and we have a defined planar orientation [50].

If there is an anisotropic medium, the energy of interaction depends on the two angles θ_s and φ_f and it is minimized at well-defined values. In fact, the LC move along a determined $\hat{x}$ axis and the director will orientate itself preferentially along this direction forming a null angle with the surface, homogeneous planar orientation, or a non-zero angle θ_p called "pre-tilt". In practical applications using LC, slides re-coated with a thin layer of high chemical stability polymeric materials, with thicknesses between 10 and 100 nm or slightly more, and a few drops of LC are deposited on these layers. Subsequently, the slide is rotated on a spinner and the drops spread uniformly [54-56]. The solvent evaporates and leaves a thin layer deposited on the surface on which a velvet cloth is rubbed. With this technique it is possible to provide a homogeneous orientation of the LC with pretilt angles that can vary between 5° and 20° degree, depending on the application. The drawback lies in the fact that, due to the friction, electric charges are left on the surface of the polymer and they can interact with a possible electromagnetic field facilitating the deterioration of the sample. Also small particles of dust can be incorporated during the process on the surface leading to a perturbation of the director. To overcome these problems

today, the lithographic technique is used through the use of a photosensitive polymer. This layer is irradiated with polarized UV rays which induce molecular transitions that lead to a reorganization of the polymer chains along the axis perpendicular to the electric field of the incident wave [50].

2.3.2 Elastic Energy

The energy of molecules is mutually influenced [50]. If they are in the sphere of interaction of the molecule itself of radius $L_{int} = 5 - 10$ nm, we can define an expression of the free elastic energy per unit of volume in the form of Taylor development in the director's space derivatives $\frac{dn_i}{dx_i}$, calculated up to the terms of the second order from which:

$$F_{el} = F_0 + a_{i,j} \cdot \frac{\partial n_i}{\partial x_j} + b_{i,j,l,m} \cdot \frac{\partial n_j}{\partial x_j} \cdot \frac{\partial n_l}{\partial x_m} \tag{2.1}$$

Where $a_{i,j}$, $b_{i,j,l,m}$ represent the tensors of the system taken into consideration i, j, l, and m are values that vary between 1 and 3. However, the eq (2.1) must satisfy the properties of symmetry of the LC, in particular, the elastic force F_{el} must remain the same if the system rotates around the director when it is inverted. According to the Oseen-Frank formalism, eq. (2.2), the energy associated with an elastic deformation can be formalized through the sum of three contributions related to as many macroscopic distortions that the crystals can undergo, such as splay (k_{11}), twist (k_{22}), or bend (k_{33}). As shown in the fig. 2.4:

$$F_{el} = \frac{1}{2} \cdot k_{11} \cdot (\nabla \cdot \vec{n})^2 + \frac{1}{2} \cdot k_{22} \cdot (\vec{n} \cdot \nabla \times \vec{n})^2 + \frac{1}{2} \cdot k_{33} \cdot (\vec{n} \times \nabla \times \vec{n})^2 \qquad (2.2)$$
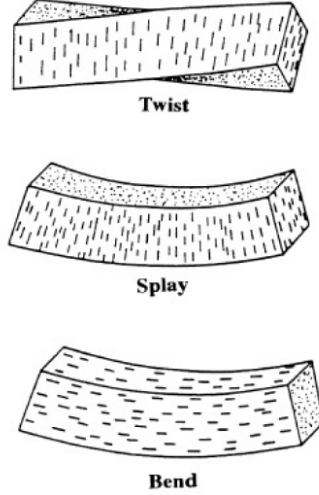
Fig. 2.4. In the figure we have represented the three possible distortions that can occur in a nematic LC [50].

Since the elastic free energy of a LC must be minimal when the director is oriented uniformly throughout the space, the eq. (2.2) must be defined positive and the constants k_{11}, k_{22}, k_{33} must be positive [50].

2.3.3 Anchoring Energy

In the case in which LC enter in contact with surfaces, the latter would exert moments of strength that would tend to orient it along one of the two easy axes. The intensity of these orientating pairs is defined by a physical parameter called anchoring energy. This corresponds to the work per unit on the surface that must be applied so the director of the LC can rotate starting from the orientation of the easy axis identified by the two angles θ_f, φ_f up to a different orientation identified by the angles of surface θ_s and φ_s. The expression of the anchor energy is defined as:

$$W_a = W_a \cdot (\theta_s, \varphi_s) \qquad\qquad (2.3)$$

In most cases, it is interesting to know how anchoring energy of LC varies when one of the two angles is kept fixed and equal to the value of the easy axis and the other is made to vary. In these cases, W_a becomes a single function and we talk about zenith anchoring energy $W(\theta_s) = W_a(\theta_s, \varphi_f)$ or azimuthal anchoring energy $W(\theta_s) = W_a(\theta_f, \varphi_s)$. The functions $W(\varphi_s)$ and $W(\theta_s)$ depend on the type of surfaces and must be defined every time. There is a function proposed a few decades ago by Rapini and Papoular [57]:

$$W(x) = \frac{1}{2} \cdot W_0 \cdot \sin^2(x - x_f) \qquad\qquad (2.4)$$

in which $x = \theta_s$ or $x = \varphi_s$, $x_f = \theta_f$ or $x_f = \varphi_f$ represent the terms in the case of zenith or azimuthal anchorage. W_0 $(\frac{J}{m^2})$ defines the anchoring coefficient that has the dimensions of an energy per unit of surface. $\frac{1}{2} W_0$ defines the work that must be performed to rotate the director $90°$ with respect to the easy axis on a surface per unit area. However, in many cases the surface interactions are very strong and even if an intense electric or magnetic field is applied, it is not possible in any way to move the director from the axis. In this case we can write the 2.2 through a parabolic expression:

$$W(x) = \frac{1}{2} \cdot W_0 \cdot (x - x_f)^2 \qquad\qquad (2.5)$$

If we want to calculate the moment of force per unit of surface that is exerted by the same on the director, it is sufficient to derive the anchor energy with respect to the angle x. By deriving the 2.3 we get:

$$\Gamma_a = -\frac{dW}{dx} = -\frac{1}{2}W_0 \cdot \sin[2(x - x_f)] \qquad (2.6)$$

In the case of strong anchorage we have:

$$\Gamma_a = -\frac{dW}{dx} = -W_0 \cdot \sin[(x - x_f)] \qquad (2.7)$$

Therefore W_0 expresses a direct measure of the elastic recall pairs' intensity that tends to orient the director along the easy axis. The pairs will be linearly linked to W_0. The higher the value of the latter, the more the return pairs must be applied to ensure that the director can be moved effortlessly from the easy axis. The measured value of W_0 is about 10^{-4} $(\frac{J}{m^2})$ and in this case we speak of strong anchorage. If we have 10^{-5} $(\frac{J}{m^2})$ then we have weak anchorage [50].

2.3.4 Dielectric properties of LC

If LC are under the effect of an electric field $\bar{E}$,[50], they polarize, acquiring a dipole moment per unit of volume $\bar{P}$. Assuming the condition of anisotropy, the polarization vector will be:

$$P_\alpha = \varepsilon_0 \cdot \chi_{\alpha,\beta} \cdot \bar{E}_\beta \qquad (2.8)$$

ε_0 is the dielectric constant of the vacuum, $\chi_{\alpha,\beta}$ dimensionless tensor of the dielectric susceptibility not parallel to the electric field. The induction vector $\overline{D}$ will be equal to:

$$\overline{D} = \varepsilon_0 \cdot \varepsilon_{\alpha,\beta} \cdot \overline{E}_\beta \qquad (2.9)$$

with $\varepsilon_{\alpha,\beta}$ being the dielectric tensor. With a nematic or skeptical LC A, the system has a rotation symmetry around the director $\hat{n}$. This implies that the electrical tensor will be diagonal if it is orthogonal respect to the $\hat{z}$ axis. The elements of the tensor matrix are ε_{11} and ε_{22} and they are equal to each other. When the electric field $\varepsilon_\perp$ is precisely perpendicular to the director, we can define the $\varepsilon_\perp$ as the first and second element of matrix tensor's diagonal for the perpendicular component of the field. When it is parallel we have $\varepsilon_{33} = \varepsilon_\parallel$. The dielectric tensor will be defined as:

$$\overline{\overline{\varepsilon}} = \begin{bmatrix} \varepsilon_\perp & 0 & 0 \\ 0 & \varepsilon_\perp & 0 \\ 0 & 0 & \varepsilon_\parallel \end{bmatrix} = \varepsilon_m \begin{bmatrix} 1 & 0 & 0 \\ 0 & 1 & 0 \\ 0 & 0 & 1 \end{bmatrix} + \frac{\Delta\varepsilon}{3} \begin{bmatrix} -1 & 0 & 0 \\ 0 & -1 & 0 \\ 0 & 0 & \frac{1}{2} \end{bmatrix} \qquad (2.10)$$

All LC are composed of atoms and molecules that self-assemble in different crystalline symmetries. For this reason they are called anisotropies. If a polarized light affects the LC, it will be reflected according to the polarization state of the crystal at that precise moment. $\hat{n}_1, \hat{n}_2, and\ \hat{n}_3$ define the components of the director $\hat{n}$ of the LC respectively for the axes $\hat{x}, \hat{y}, \hat{z}$, and the result of the propagation will be linked to the three indices. The axis z is the axis along which the wave propagates. If $n_1 \neq n_2$ then the

crystal is called biaxial. In the case where $\hat{n}_1 = \hat{n}_2$ the crystal will be uniaxial. If $\hat{n}_3 > \hat{n}_1, \hat{n}_2$ the crystal will be called positive or biaxial positive, otherwise with $\hat{n}_3 < \hat{n}_1, \hat{n}_2$ it will be negative or negative biaxial. In the case of a uniaxial LC, like nematic LC, if $\hat{n}_1 = \hat{n}_2$ these indices are defined as ordinary index n_o and extraordinary n_e. The ellipsoid of the indices, fig. 2.5, is a graphical method that allows to easily identify the orientation of the two polarizations and their velocities. This surface derives from the following equation:

$$\frac{x^2}{\hat{n}_1^2} + \frac{y^2}{\hat{n}_2^2} + \frac{z^2}{\hat{n}_3^2} = 1 \tag{2.11}$$
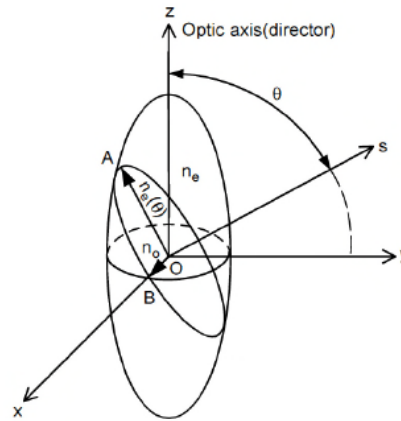
Fig. 2.5. Ellipsoid of indices for a planar wave polarized along the s axis in a uniaxial crystal in which we also visualized the refractive indices of the crystal n_e and n_o [50].

We can therefore express the indices of refraction according to the diagonal components of the dielectric tensor given by simple relationships:

$$\hat{n}_1 = \sqrt{\varepsilon_{11}}, \quad \hat{n}_2 = \sqrt{\varepsilon_{22}}, \quad \hat{n}_3 = \sqrt{\varepsilon_{33}}, \tag{2.12}$$

If we consider the propagation axis along the direction $\hat{k}$ as shown in fig. 2.5, we observe that two polarization vectors are generated: one along the plane $\widehat{xz}$, the other along the plane $\widehat{yz}$. Therefore, we have two waves, one independent of the propagation angle:

$$n_o(\theta) = n_o \qquad (2.13)$$

And the other dependent:

$$n_e(\theta) = \frac{n_e \cdot n_o}{[n_e^2 \cdot \cos^2(\theta) + n_o^2 \cdot \sin^2(\theta)]^2} \qquad (2.14)$$

2.3.5 Electro-Optic effect in LC

Generally speaking, [50], the distortion of the molecules of LC can occur thanks also to an electromagnetic wave coming from a light source such as a laser or through a voltage applied to electrodes made on the device [15]. In the first case there is no appreciable change in the index of refraction, as it could be obtained by applying the electromagnetic field alone [52-53]. The latter process alters the optical properties of the medium. In the presence of an applied field, the ellipsoid of the indices seen previously become:

$$x^2 \cdot \left(\frac{1}{n^2}\right)_1 + y^2 \cdot \left(\frac{1}{n^2}\right)_2 + z^2 \cdot \left(\frac{1}{n^2}\right)_3 + 2 \cdot y \cdot z \cdot \left(\frac{1}{n^2}\right)_4 + 2 \cdot x \cdot z \cdot \left(\frac{1}{n^2}\right)_5 + 2 \cdot x \cdot y \cdot \left(\frac{1}{n^2}\right)_6 = 1$$

$$(2.15)$$

46

where the coefficient $\left(\frac{1}{n^2}\right)_i$ depends on the electric field $\bar{E}$. If it is null, the consequence is that the first three indices are different from zero and the others are null. The response of the nematic LC director to external stresses generated by an electric field depends on dielectric anisotropy. For the positive one-sided LC, the director will tend to align in parallel with the field propagation vector. In the case of a negative one, it will follow another direction forming a tilt angle with the field propagation vector, as shown in the fig. 2.6.
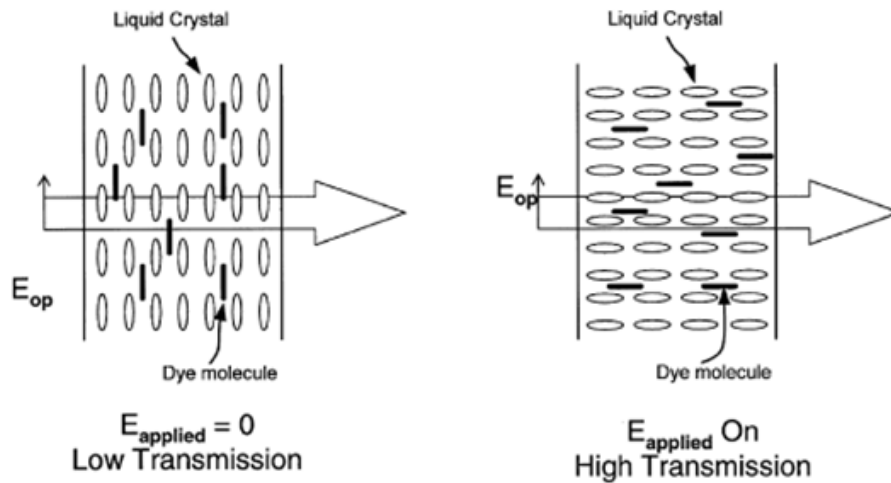

Fig 2.6. Example of alignment of a nematic LC subject without and with an external electric field, respectively on the left and on the right [1].

If we want to produce an orientation of the director we could use positive uniaxial nematic LC with a planar alignment or, as simulated in this thesis, a negative one with a homotopic alignment. In this last case, only some molecules have a direction assigned through a pre-tilt angle. All the others are free to move in all directions. In any case, when using LC, it is necessary to keep in mind that they are treated according to the uses which vary their mechanical properties. One example is when the elastic constant or the

dielectric anisotropy $\Delta\varepsilon$ seen previously is modified to have a better response in the orientational variation of the molecules [50].

2.3.6 Free energy and torque by electric and magnetic fields

For a generally applied electric field [50], such as $\bar{E}$, the displacement $\bar{D}$ can be written in the form:

$$\bar{D} = \varepsilon_\perp \cdot \bar{E} + (\varepsilon_\parallel - \varepsilon_\perp) \cdot (\hat{n} \cdot \bar{E}) \cdot \hat{n} \qquad (2.16)$$

the electric interaction energy density is therefore:

$$\mu_E = -\int_0^E \bar{D} \cdot d\bar{E} = -\frac{1}{2}\varepsilon_\perp \cdot (\bar{E} \cdot \bar{E}) - \frac{\Delta\varepsilon}{2} \cdot (\hat{n} \cdot \bar{E})^2 \qquad (2.17)$$

the first term on the right-hand side of eq. (2.17) is indipendent of the orientation of the director axis. It can therefore be neglected in the director axis deformation energy. Accordingly, the free-energy density term associated with the application of an electric field is given by:

$$F_E = -\frac{\Delta\varepsilon}{2} \cdot (\hat{n} \cdot \bar{E})^2 \qquad (2.18)$$

the molecular torque produced by the electric field is given by:

$$\Gamma_E = \bar{D} \times \bar{E} = \Delta\varepsilon \cdot (\hat{n} \cdot \bar{E}) \cdot (\hat{n} \times \bar{E}) \qquad (2.19)$$

similar consideration for the magnetic field yield a magnetic energy density term U_m given by:

$$U_m = -\int_0^M \overline{B} \cdot dM = \frac{1}{2 \cdot \mu_0} \cdot \chi_\perp^m \cdot B^2 - \frac{1}{2 \cdot \mu_0} \cdot \Delta\chi^m \cdot (\hat{n} \cdot \overline{B})^2 \qquad (2.20)$$

a magnetic free-energy density, associated with the director axis reorientation, F_m given by

$$F_m = \frac{1}{2 \cdot \mu_0} \cdot \Delta\chi^m \cdot (\hat{n} \cdot \overline{B})^2 \qquad (2.21)$$

and a magnetic torque density:

$$\Gamma_E = \overline{M} \times \overline{H} = \Delta\chi^m \cdot (\hat{n} \cdot \overline{H}) \cdot (\hat{n} \cdot \overline{H}) \qquad (2.22)$$

these electric and magnetic torque play a central role in various field induced effects in LC [50].

2.3.7 Freedericksz transition revisited

Consider the three tipical aligned nematic LC cells depicted in figure, corresponding to planar, homeotropic, and twisted of nematic LC of positive anisotropy. With the applied electric field shown, they correspond to the splay, bend and twist deformation. In the first and second cases, substantial director axis reorientation involves some combination of splay and bend deformations. Pure splay and bend deformations are

characterized by elastic constants k_{11} and k_{33} respectevely, occur only for small reorientation. The twist deformation is the "pure" deformation in contrast to the other two deformations, and depend from the k_{22}, constant [50].
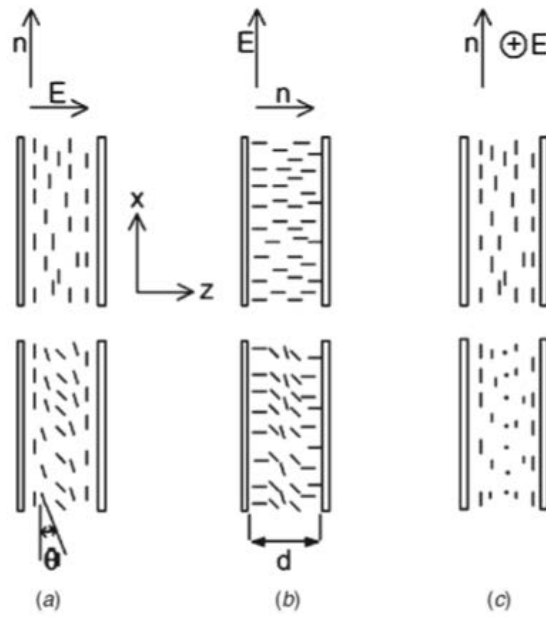

Fig. 2.7. Geometry for observing a) Splay deformation, b) Bend deformation c) twist deformation. The upper row shows the initial orientation, and the bottom row shows the deformation when the field exceeds the threshold values [50].

2.3.7.1 Case 1: One elastic constant approximation.

For the simplest case under one-elastic -constant approximation and strong boundary anchoring condition, the free energy of the nematic LC layer can be obtained by integrating over the sample thickness d:

$$G = \frac{1}{2} \cdot \int_0^d \left[k \cdot (\frac{d\theta}{dz})^2 - \frac{\Delta\varepsilon}{4 \cdot \pi} \cdot \overline{E}^2 \cdot \sin^2 \theta \right] \qquad (2.23)$$

where θ is the reorientation angle, k the elastic constant, $\bar{E}$ the applied field, and $\Delta\varepsilon = \varepsilon_{\parallel} - \varepsilon_{\perp}$. The solution of eq. (2.23), can be obtained using a standard variation method:

$$k \cdot \frac{\partial^2 \theta}{\partial z^2} + \frac{\Delta\varepsilon}{4 \cdot \pi} \cdot \bar{E}^2 \cdot \sin(\theta) \cdot \cos(\theta) = 0 \qquad (2.24)$$

The relation between the reorientation handle and the external field can be derived by integrating the equation above:

$$d = \int_0^{\theta_m} \left[c + \frac{\Delta\varepsilon}{8 \cdot \pi \cdot k} \bar{E}^2 \cdot \cos(2\theta) \right]^2 \cdot d\theta \qquad (2.25)$$

θ_m is the maximum reorientation angle. Constant c can be determined by minimizing the energy G, then can be derived the final expression relating θ and E:

$$\frac{\bar{E} \cdot d}{2} \cdot \left(\frac{\Delta\varepsilon}{4 \cdot \pi \cdot k} \right)^2 = \int_0^{\theta_m} \frac{d\theta}{[\sin^2(\theta_m) - \sin^2(\theta)]^{1/2}} \cdot = F(k) \qquad (2.26)$$

The right-hand side of eq. (2.25) is an elliptic integral of the first kind, which is tabulated for values of $k = sin\theta_m < 1$. For small reorientation angles the elliptic integral can be expanded as a series. eq. (2.25), can be approximated to the second-order:

$$\bar{E} = (\frac{4 \cdot \pi \cdot k}{\Delta\varepsilon})^{1/2} \cdot \frac{\pi}{d} (1 + \frac{1}{4} \cdot \sin^2(\theta_m) + ...) \qquad (2.27)$$

Eq. (2.27) shows that a deformation with $\theta_m \neq 0$ occurs only if the external fields exceed the threshold $E > E_f$, where:

$$\overline{E}_f = (\frac{4 \cdot \pi \cdot k}{\Delta \varepsilon})^{1/2} \cdot \frac{\pi}{d} \tag{2.28}$$

From the eq. (2.28) the Freedericksz threshold voltage $V_f = E_f \cdot d = (\frac{4\pi k}{\Delta \varepsilon})^{1/2} \cdot \pi$ is indipendent of sample thickness. For small director orientation, the maximum reorientation angle θ_m may be obtained from eq. (2.27) [50]:

$$\frac{V}{V_F} = 1 + \frac{1}{4} \cdot \sin^2(\theta_m) \tag{2.29}$$

2.3.7.2 Case 2: Freedericksz transition voltage including elastic anisotropies.

Taking into account the anisotropic properties of the elastic constant (i.e. different k_{11}, k_{22}, k_{33}) eq. (2.24) becomes:

$$\frac{d}{dz}\left\{\left[k_{11} \cdot \cos^2(\theta) + k_{33} \cdot \sin^2(\theta) \cdot \frac{d\theta}{dz}\right]\right\} - (k_{33} - k_{11}) \cdot \sin(\theta) \cdot \cos(\theta) \cdot (\frac{d\theta}{dz})^2 = -\frac{\Delta \varepsilon}{4\pi} \cdot \overline{E} \cdot^2 \sin(\theta) \cdot \cos(\theta) \tag{2.30}$$

we can obtain:

$$\frac{V}{V_F} = 1 + \frac{1}{4}(1 + \kappa + \frac{\Delta \varepsilon}{\varepsilon_\perp}) \cdot \theta_m + \dots \tag{2.31}$$

where:

$$\kappa = \frac{k_{33} - k_{11}}{k_{11}} \tag{2.32}$$

and the Freedericksz transition voltage $V_f = (\frac{4\pi k}{\Delta \varepsilon})^{1/2} \pi$ [50].

2.3.7.3 Case 3: Freedericksz transition voltage including elastic conductivity.

If nematic LC layer is conductive as a result of dopants or presence of impurities, eq. (2.30) changes slightly under the influence of electrical conductivity. The maximum reorientation angle θ_m is described by:

$$\frac{V}{V_F} = 1 + \frac{1}{4} \cdot (1 + \kappa + a) \cdot \theta_m^2 + \dots \tag{2.33}$$

where $V_f = (\frac{4 \cdot \pi \cdot k}{\Delta \varepsilon})^{1/2} \pi$, $\kappa = \frac{k_{33} - k_{11}}{k_{11}}$ accounts for elastic anisotropy, and

$$a = \left[\frac{\sigma_\parallel - \sigma_\perp}{\sigma_\perp} + (\frac{\omega}{\omega_c})^2 \cdot \frac{\varepsilon_\parallel - \varepsilon_\perp}{\varepsilon_\perp} \right] \cdot \left[1 + (\frac{\omega}{\omega_c})^2 \right]^{-1} \tag{2.34}$$

with $\omega_c = 4 \cdot \pi \cdot \frac{\sigma_\perp}{\varepsilon_\perp}$. The Freedericksz transition voltage is identical to the case of nonconducting nematic LC. However, the presence of electrical conductivity does affect the director orientation for external voltage above threshold. For voltage above threshold V_F, the LC deformation depends on the ratio of elastic constants $\frac{k_{33}}{k_{11}}$, on the electric conductivity, and on the

applied frequency. For very high frequency $\omega \to \infty$ the coefficient a$\to \frac{\Delta\varepsilon}{\varepsilon_\perp}$ the nematic LC becomes nonconductive. But for very low frequency $\omega \to 0$ the coefficient a$\to \frac{\Delta\sigma}{\sigma_\perp}$, the electric conductivity becomes dominant [50].

2.4 LC in photonic applications

LC are promising materials suitable for the fabrication of optical switches both in free-space and waveguided structures. Their transparency in the near infrared spectrum, high birefringence, refractive index ranging between 1.4 and 1.6, are just a few characteristics that make LC ideal as active material for silica optical fibers, lasers, and low loss optical waveguides (e.g. glass, silica on silicon, polymers). As Maune et al. have demonstrated [54], nematic LC (E63 $n_e = 1.744$, $n_o = 1.517$ at 589 nm) crystals allow to electrically control the cladding refractive index of the ring resonator. For instance, the authors achieved a maximum resonance shift of about 0.22 μm (at 1.55 μm by applying 20 V) on SOI wafers with top silicon thickness of 205 nm, oxide thickness of 1 μm, ring radius of 5 μm, and ring and waveguide widths of 500 nm, whose picture is reported in fig. 2.8
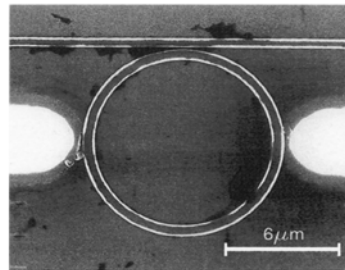

Fig. 2.8. SEM top view of ring resonator with modulation electrodes at the edges of the pictures [54].

Besides, M. Humar et al. [55] have introduced whispering-gallery-mode (WGM) resonators based on nematic LC (E 12 with a refractive index of $n_e = 1.74$ and $n_o = 1.52$) droplets infiltrated into PDMS microcavities, fig. 2.9. They have been able to achieve a resonant frequency tunability two orders of magnitude higher than classical solid state microresonators. Such a large resonance frequency shift has been attained through electric field-induced structural distortions of the birefringent LC resonator medium. Indeed, nematic LC microresonators have shown a resonance shift of about of 20 nm (at 600 nm by applying 2.6 V) Q-factors as high as 12,000 for 33-mm diameter droplets.
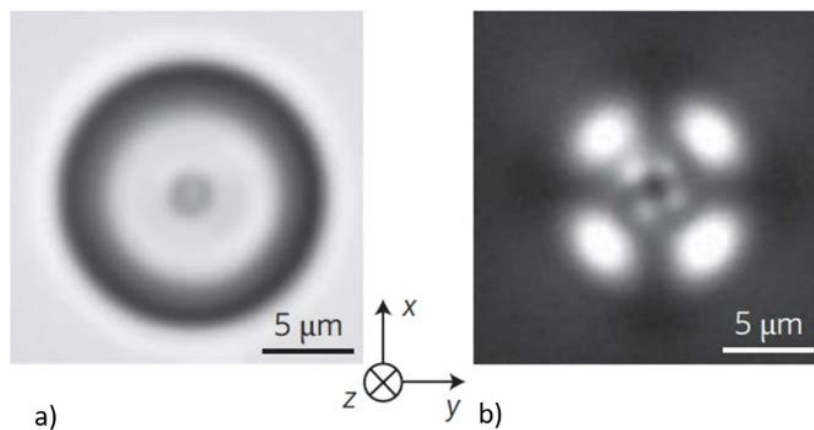
Fig. 2.9. a) E12 droplet inside the PDMS microcavity, b) photo taken with crossed polarizer [55].

LCs have been also employed as top cladding material in others type of ring resonators. In fact, De Cort et al. [56] devised ring resonators operating in the C-band, fig. 2.10. Their TM ring resonator has showed variable Q-factors according to the electric potential difference.). Such a voltage dependence can be explained by taking into account the re-orientation of LC molecules located into the cladding part of the device. In

details, the Q-factor associated to the TM and TE has showed show a slope change (from negative to positive) at about 100 V. Minimum values detected for the TM and TE Q-factors are 4000 and 8500, respectively. On the other hand, the maximum values are 10000 (TM) and 17000 (TE). Also, the tunability range and the direction of the resonant frequency shift have proved to depend on the polarization state of the impinging radiation. Specifically, for the TM-polarized light a red-shift of 31 nm has been found, whereas a blue shift of 4.5 nm has been observed for the TE-polarized.
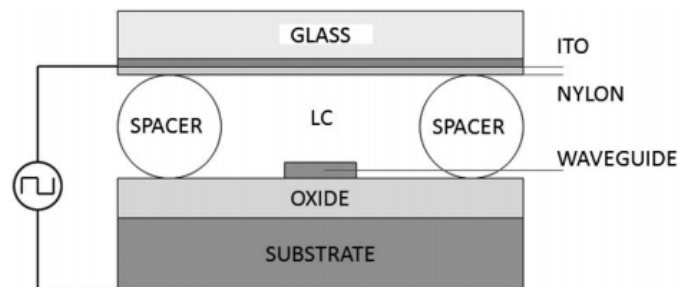
Fig. 2.10 depicts a cross section of the SOI ring resonator with LC used as cladding [56].

SOI-based waveguides can be combined with LCs to shift the phase of the input electromagnetic radiation instead of the frequency. For instance, Pfeifle et al. [57] has demonstrated that a 1-(trans-4Hexylcyclohexyl)-4-isothoicyanatebenzene-coated SOI waveguide is able to produce a phase shift of 35 π with a drive voltage of 5 V at 1500 nm. The device, fig. 2.11 was characterized by a high level of miniaturization. Indeed, the overall waveguide length hasn't exceeded the 100 µm.
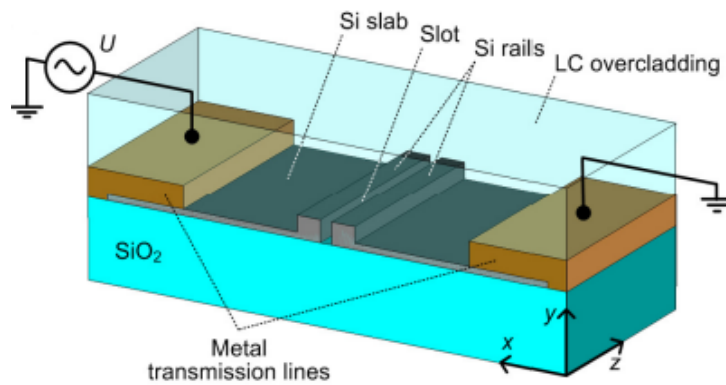
Fig. 2.11. Sketch of a slot waveguide in which the LC covers all the structure [57].

C. Levallois et al. [58] have fabricated and characterized a VCSEL laser made out of nanosized LC (BL 24) spacers (nano-PDLC) inserted between the dielectric Bragg mirror and the active region, fig. 2.12. The use of LC has allowed to achieve a laser emission around 1.55 µm while applying a 170 V electric potential difference. This approach led to a tuning range of 9.8 nm. Moreover, as the applied voltage has been raised from 0 to 170 V the output power has increased by 3dB. The active and tuning layer thicknesses have been tailored (0.7 and 6 µm respectively) in order to achieve high laser gains.

Fig. 2.12. Cross section of the VCSEL using nano-droplets of PDLC [58].

Another class of devices that have been already implemented by exploiting the LC technology are the POLICRYPS [59] (Polymer Liquid CRYstal Polymer Slices) Bragg diffraction gratings, fig. 2.13. The device has been comprised of a composite material constituted by polymer sliced interposed between LC (E-7) films. The LC director orientation has been arranged to be perpendicular to the polymer stripes when no external electric field is applied. The device has been dimensioned as follows: grating pitch 2.5 μm, thickness 4.5 μm, length 11 mm. The output signal after attenuation by the POLICRYPS filter has been found to be 20 dB at the wavelength of 1552 nm. A squared voltage waveform oscillating at 1kHz and possessing an amplitude of 40V has been used to detect the optical reflection response of the filter tuned for 4nm.
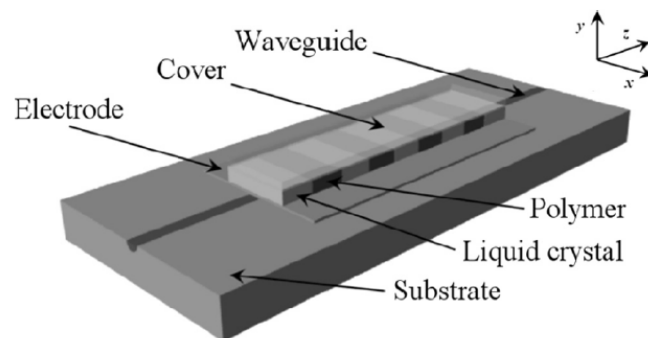
Fig. 2.13. Sketch of integrated optical filter with POLICRYPS [59].

Besides their electric tunable orientation, LC possess non-linear optical properties that can be exploited for second harmonic generation. Thereby, non-linearity can be employed for butt-coupled optical fibers and variable optical attenuators. For instance, V-grooved [60] LC waveguides arranged as reported in fig. 2.14. The device has been fabricated as follows. A thermally oxidized n-type Si wafer has been preferentially etched to create

a groove for the LC insertion. The LC has been "encapsulated" by a spin-coated thin (50 nm) layer of Nylon. Finally, the waveguide has been topped with an-ITO coated borosilicate glass (refractive index 1.5116 at 1550 nm). The orientation of the NLC director, in function of tilt (θ) and twist angle (φ) is depicted in figure. The device has been able to operate at voltages of about 5 V generating an on-off extinction ratio over 40 dB. The overall insertion loss was 14 dB. Such an overall loss can be de-convoluted into propagation and coupling losses. The largest contribution to the 14dB has been found to stem from the E7 LC coupling losses.
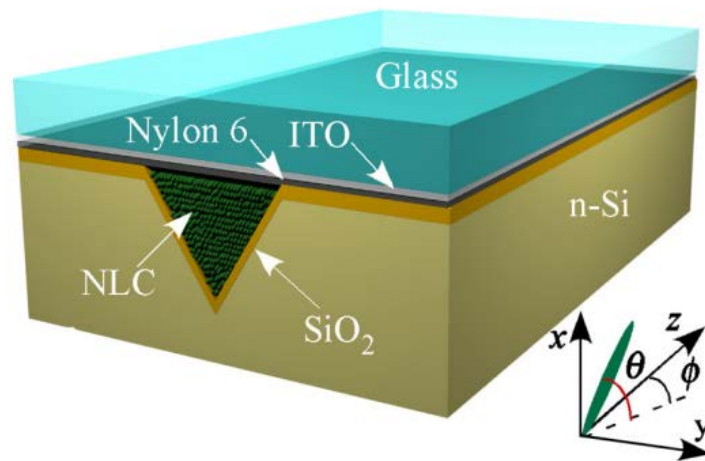
Fig. 2.14. Schematics of a V-grooved channel waveguide [60].

Conclusions

LC are materials which show a certain degree of ordering (positional and/or orientational) intermediate between liquid and solid. The majority of LC that are used in photonic applications are of the thermotropic type. Thermotropic means that the LC phase exists within a certain temperature interval. The excellent electro-optic properties of LC have been widely applied to design tunable photonic components starting from waveguide-based devices, ring resonators, optical filters and switches and lasers also employing their strong optical nonlinearity [15], [60].

Chapter 3: Fabrication and characterization of LC:PDMS waveguides

3.1 Fabrication of LC:PDMS waveguides

The fabrication of devices based on LC infiltrated in PDMS channels called LC:PDMS waveguides [15], [25], [61], is based on soft lithography techniques common to Microelectronics. In order to study the optical properties of LC:PDMS waveguides and test the NLC E7 alignment, three waveguide groups of 8, 10 and 15 µm widths were designed respectively. Each set consists of 5 micro-channels, with a length of 1 cm and a height of 5 µm. The guide sets are equally spaced by 80 µm to avoid optical coupling. MicroChem's negative photoresist SU-8 2005 Microchem® was used to create microchannels, as shown in fig. 3.1.
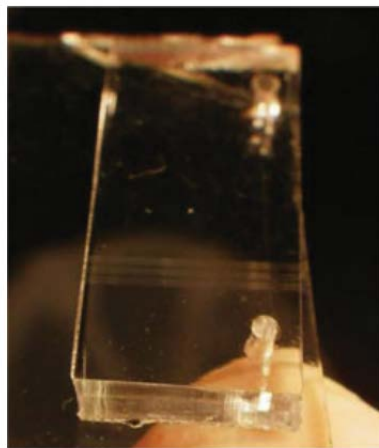

Fig 3.1. A prototype with sets of E7 nematic LC straight waveguides in PDMS [15].

To obtain the required 5 µm thick structures, a silicon wafer was used, on which the native oxide layer was removed by wet etching in HF. On this 2

cm silicon square the photoresist SU-8 was poured and was spinned by the spin coating machine, with three different ramps at different speeds: 500 rpm for 5 seconds with acceleration of 500 rpm / s, a second ramp at 3000 rpm for 30 seconds again with 500 rpm / s acceleration. The substrate covered with the SU-8 was heated on a heating plate for 1 minute at 65 ℃ and 2 minutes at 95 ℃. In the photolithography process, a UV illumination with a wavelength of 360 nm was used and the best results were obtained with an energy value of 250 mJ/cm2. A further post-exposure step was performed using the heating plates again for 1 minute at 65 ℃ and for 1 minute at 95 ℃. After cooling the sample was immersed in the SU-8 developer for 1 minute for unexposed photoresist to be removed. Initially, the PDMS is a non-cross-linked liquid form, with the trade name SYLGARD 184 of Dow Corning®. The PDMS consists of two elements: resin and crosslinker. These two components are mixed at room temperature in a 10: 1 by weight ratio. In the first step, the waveguides were made by pouring the liquid mixture of PDMS on the previously produced silicon sample. The silicon on which the liquid PDMS was poured was then placed in a [5 cm × 5 cm] sided box, to accommodate 3 mm thick PDMS. Then the whole box was placed in a vacuum bell. The forced vacuum eliminated the bubbles created by mixing between the resin and the crosslinker. In the third and last step, a uniform PDMS film was obtained by spin coating on a carefully cleaned glass surface. In order to avoid air entrapment in the PDMS channels, all the prepared parts were placed under vacuum for 30 minutes. The samples were baked at 100 ℃ for 15 minutes. The PDMS with the glass substrate was kept empty for 8 minutes, since the thickness of the latter component requires a shorter cooking time. The integral cooking time of the parts was calibrated to

obtain a reproducible PDMS to allow removal from the silicon supports and to be subsequently assembled without deformation. The PDMS with micro-channels was then removed from the mold the excess parts were cut. The complete assembly of the assembled sample in fig. 3.1 was finally baked at 80 ℃ for 60 minutes. The manufacturing process was completed by drilling a hole to connect the channel to the tank and to the micro-channels through a channel perpendicular to the guide sets as shown in fig. 3.2.
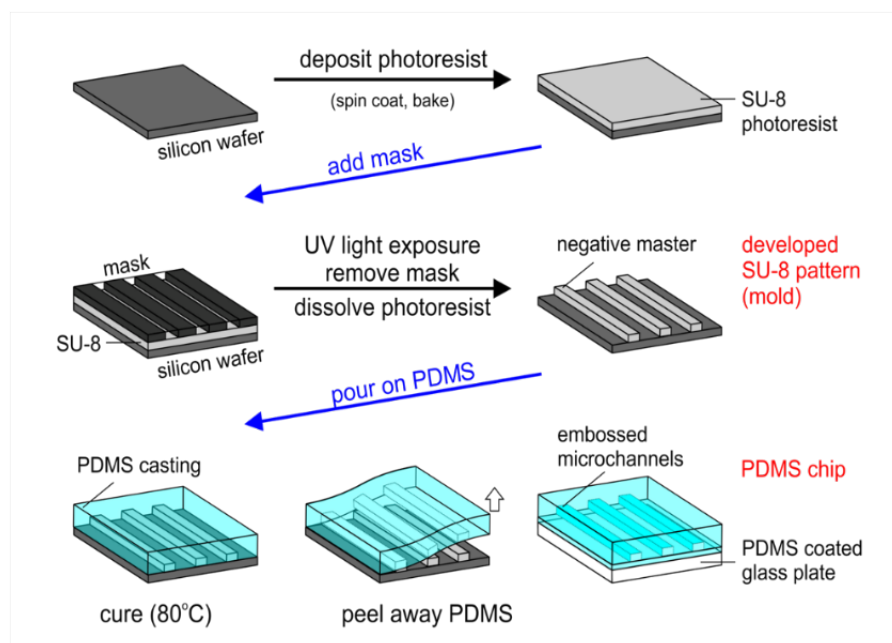

Fig 3.2. A fabrication process based on casting and molding techniques can be employed to obtain LC:PDMS.

The device was then placed in a vacuum oven and baked at 80 ℃. The micro-channels were filled with capillarity and then cooled to room temperature as shown in the fig. 3.3. The NLC E7 was introduced into the isotropic mesophase through the vertical channels.
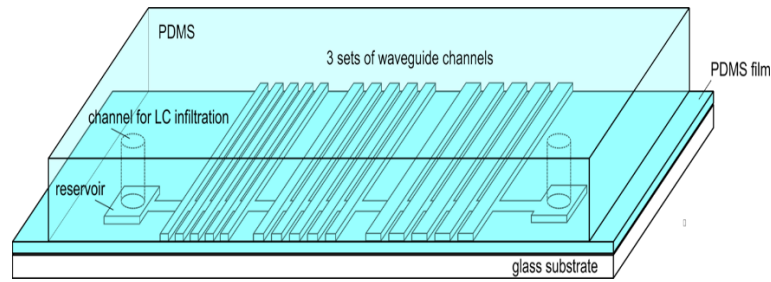
Fig 3.3. The LC is infiltrated by capillarity in the isotropic phase in the channels through the reservoir in a vacuum oven at 80℃.

NLC filled channels show light transmission through the edges and appear black in the center. This is due to the homeotropic alignment of the NLC molecules, producing an optical delay between the polarizers only along the edges and not in the medium where the molecules are aligned perpendicular to the horizontal plane. This is due to the low-energy surface of PDMS, which provides a minimal contact interface between rod-like NLC molecules and PDMS surface. Because of the unnatural orientation of the NLC molecule, it was not necessary to use an alignment layer as in most LC optical devices. This intrinsic characteristic of the PDMS means that production steps are minimized in the production of optofluidic devices and therefore increases the probability of operation of the device. In our samples the NLC alignment was the same for the three waveguide assemblies, showing the independence with respect to the waveguide width [15].

3.2 Characterization of LC:PDMS guides

For the optical characterization of prototypes in LC: PDMS [15], [25], [61], we must first perform an examination through a polarized microscope to verify that all the channels, or most of them, are completely filled with the LC. The second test that is carried out is that of light propagation within

the individual guides. The characterization of polarized microscope observation revealed an interesting feature of the arrangement of NLC molecules within the PDMS channels. The PDMS surface is hydrophobic respect to the NLC, LC molecules are homeotropically oriented on the borders of the channel, i.e. are perpendicular to the PDMS channel walls. The channels appear black in the center and bright along the edges. In fact, this image determines the arrangement of the E7 LC molecules inside the microfluidic channels of the PDMS. This molecular arrangement occurs spontaneously without using any alignment layer placed on the PDMS, which results in a minimal contact interface between the NLC molecules and the surface of the PDMS itself. The LC molecules close to the PDMS edges create an optical delay that can be appreciated by using a polarizing microscope. On the other hand, the LC molecules located in the middle of the waveguide are homeotropically aligned and, therefore, they block the light path when the two polarizer are crossed.
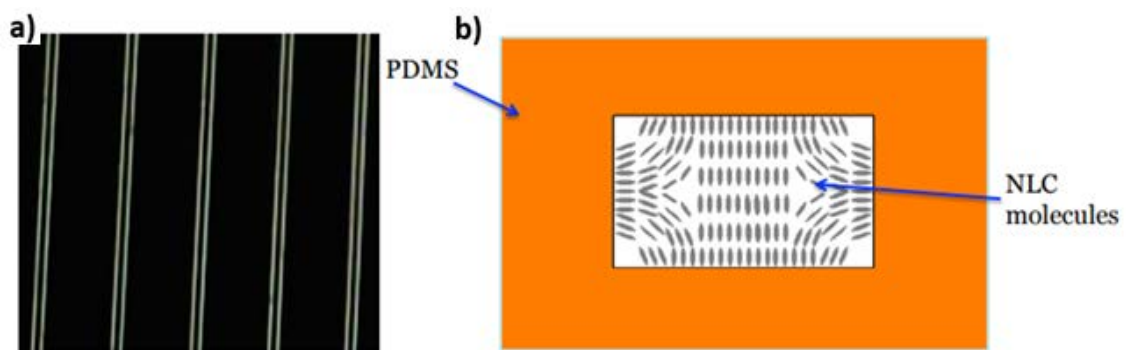

Fig.3.4. a) A polarizing microscope image of LC homeotropic alignment in PDMS channels. b) schematics of a LC:PDMS waveguide in which is represented the LC homeotropical molecular orientation [25].

The characterization of the light transmission occurs through the use of lasers at different optical wavelengths. Both light sources in the visible and in the near infrared were used. All optical channels are able to transmit light in multimode propagation regime considering that the refractive index of the PDMS, equal to 1,406 and that the wavelength of the input laser is 1550 nm. The refractive index is much lower than the refractive indices of E7 since the optical confinement of the light wave must be achieved. The coupling between the light source and the sample can take place through the use of two fibers: one single-mode and one multimode. In fig. 3.5 there is a waveguide illuminated by a green light beam at the wavelength of 532 nm emitted by lasers atNd^{+3}:YVO$_4$.
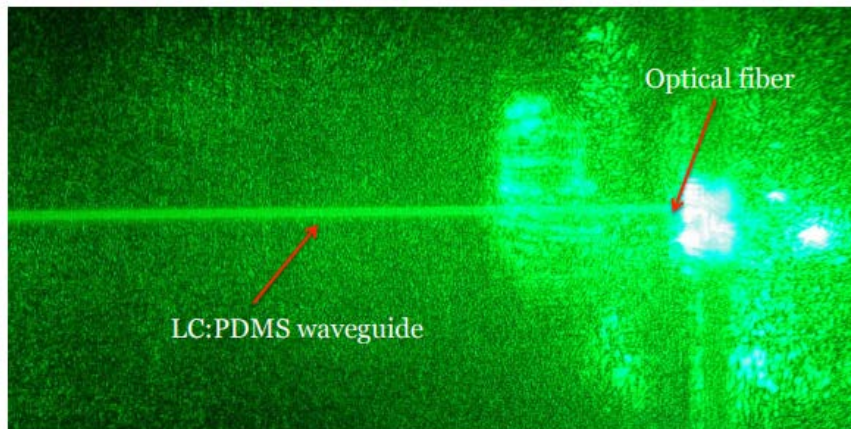

Fig. 3.5. A LC: PDMS waveguide coupled through a fiber in which a green beam propagates itself [25].

A similar behavior was observed considering a red light beam emitted by a He-Ne laser source. A DFB laser was also used to study the propagation in the C band of the near infrared spectrum. To study the polarization of the incoming electromagnetic wave it was necessary to use three retarder

waveplates. It was observed that light transmission is almost polarization independent. This phenomenon is quite unusual for an anisotropic medium such as LC. The output signal strength was monitored using an optical power meter, as shown in fig. 3.5. Through a sequence of three retarder plates, $\frac{\lambda}{4}$, $\frac{\lambda}{2}$, $\frac{\lambda}{4}$, used to calibrate and to control light polarization, from TE mode to TM mode, at the waveguide input, which led to a variation of luminance intensity of only 0.3 dB as shown in fig. 3.7. Furthermore, it was established through the polarizer that the light beam, after traveling through the waveguide, showed that the bias is preserved during propagation in the channel. The non-variation of the incoming bias is related to the distribution of the non-uniform refraction index of the LC within the PDMS channels. In fig. 3.6 the experimental setup used for optical characterization of the LC:PDMS waveguides is reported [61].
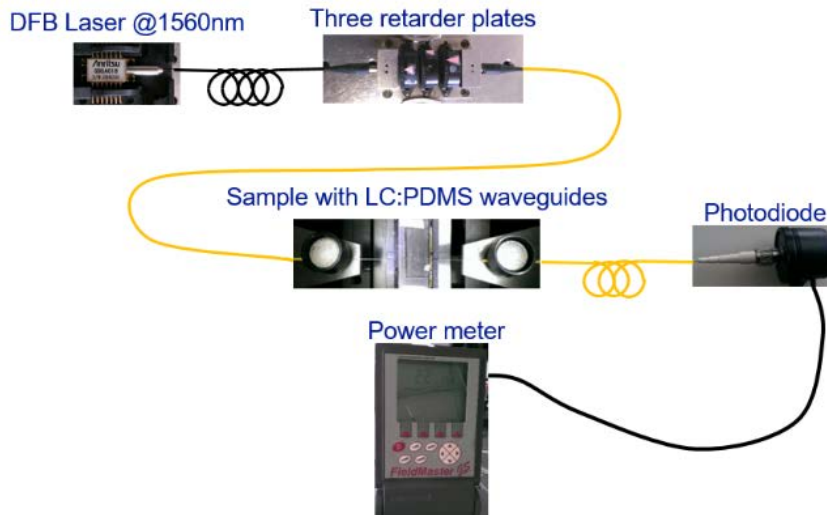
Fig. 3.6 show that a polarization independent light transmission was achieved, despite the typical LC optical anisotropy. Measured light transmission at 1550 nm versus polarization in a LC:PDMS prototype [61].
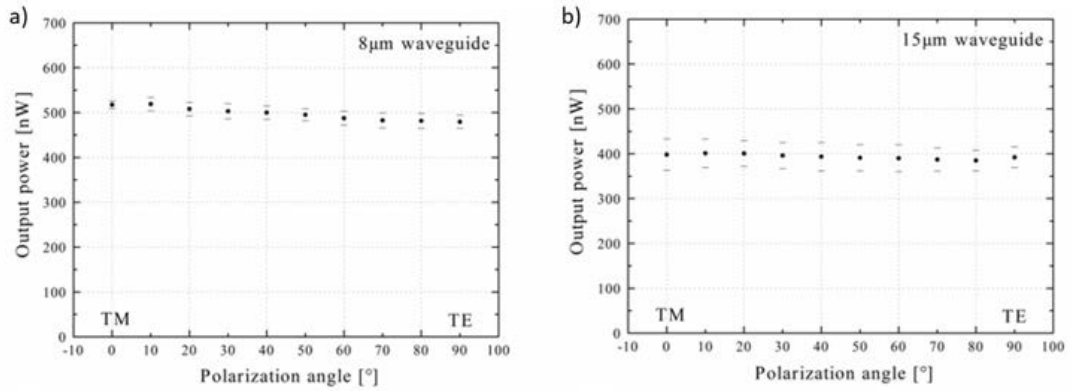
Fig 3.7. Light-weighted pathway with the width of 8 μm on the left and 15 μm on the right at the wavelength of 1550 nm. The transmission variation of only 0.35 dB has been observed to be the orientation of the LC [61].

3.3 Fabrication of co-planar electrodes for electro-optic LC:PDMS waveguides

In the fabrication of the electrodes, various materials were used, such as Indium tin oxide (ITO), chromium (Cr), titanium-tungsten (TiW), and aluminium (Al). In this section each single process will have an introductory paragraph in which the fundamental principles of its technology will be explained. There will be a description of the results obtained through that technology to create the coplanar-electrodes.

3.3.1 Fabrication of samples by evaporation process

The evaporation processes [62-72] involved only a few samples because the temperatures reached in the vacuum chamber were at least 150-200 °C on the substrate. This involved a dilation and subsequent contraction due to the thermal coefficient of the PDMS which resulted in an imperfect

surface uniformity of the deposited material. The metals involved in the evaporation process were Cr and Al. The non-uniformity of the deposited thin films contributed to a rippled surface with the formation of metallic islands, visible in the fig. 3.8 a) and b) that did not allow to obtain good-quality metal films. In the evaporation process, it was necessary to superimpose layers of Cr to Al to avoid linking of the Al atoms with the oxygen present in the deposition chamber, obtaining Al_2O_3, an insulating film instead of a conductive metal film. The Cr / Al / Cr samples were produced with two different thicknesses: 50/150/50 Å, but the thinness of the deposited layers did not allow to detect the resistivity of the latter, so I decided to fabricate thicker layers with 200/600/200 Å. Subsequently, the fragility of the samples can be guessed by the observation of the samples, with the deposited metal films showing a very poor adhesion to the PDMS substrate. For these reasons, I have judged it useless to deepen the analysis through the SEM. Therefore, no further characterizations have been made on them.
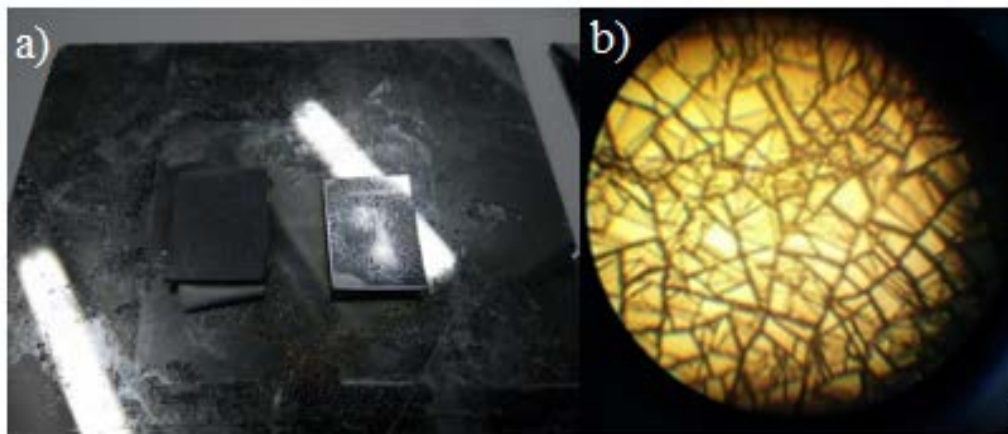

Fig. 3.8. Picture showing a deposition by evaporation method of Cr/Al/Cr (200/600/200). In a) there is roughness on the surface of the metal deposition. In b) the same devices examined at the microscope with a lens of 10x.

3.3.2 Sample fabrication by sputtering process

The sputtering processes [74-80] through which I made co-planar electrodes involved targets of ITO, Cr, and Ti-W. The depositions that involved the ITO were carried out at different temperatures for different exposure times. ITO is a widely used material in optoelectronics and photonics because it is a transparent conductive oxide that guarantees good resistivity values. In the case of electrode production through the evaporation process, in the sputtering process the formation of the superficial islands of the deposited ITO occurred. These films were made at various temperatures of 25 ℃, 100 ℃, 150 ℃ for different times but Cr's depositions were only carried out at a temperature of 25 ℃. The metal target available was the only one not to have created islands since it is an extremely ductile metal. Having characterized the samples produced at 25 ℃ through I-V measurements and having obtained a resistive behavior, I did not proceed to manufacture other samples for temperatures of 100 ℃, 150 ℃. Ti-W films behaved like samples produced by the evaporation method, for temperatures of 25 ℃ and 100 ℃, there were a ripple formation on the surface of the samples. For this reason, no other characterizations have been made on them.

3.3.3 Indium Tin Oxide (ITO)

The fabrication of samples in ITO required a refinement of the process. We started from making thin conductive oxide films at temperatures ranging between 150 ℃ and 100 ℃ with various time values of 7 minutes until decreasing to reach 30 sec. In this case, as for the other devices made in

temperature, the difference between the coefficients of thermal expansion has led to the surface roughness equivalent to those obtained with the process of evaporation of Cr / Al / Cr as illustrated in the pictures 3.9 a) b) c) d).
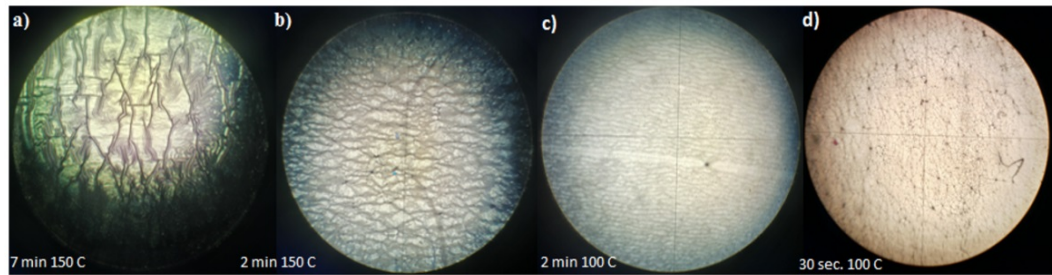
Fig. 3.9. In the images we have the samples made with different temperature values for different exposure times. As can be seen by decreasing the exposure times of the samples in combination with a reduction in temperature, there is less surface rippling which leads to a better surface yield.

By examining ITO samples under an optical microscope, fig. 3.9, a higher surface uniformity was obtained for different decreasing temperatures. Aware of the fact that at room temperature better uniformity could be obtained due to the lower thermal stress, I made several samples at 25 ℃ but I increased the time of exposure to the sputtering process compared to the samples produced in the fig. 3.9 d). The samples in fig. 3.10 have a temporal range that varied from 30 secs up to 1.30 min in 30 sec steps. Subsequently, these samples were examined by SEM to determine with extreme precision, what the thickness of ITO made was. From the measurements, it was possible to establish that in just 30 seconds of exposure, a film of only 30 nm was obtained, with a ratio of about 1:1 between the deposition and the exposure time, as shown in fig. 3.9:
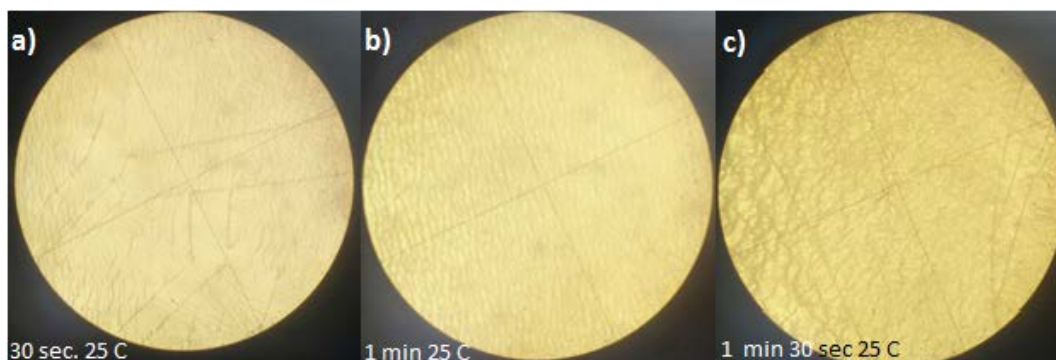
Fig. 3.10. From left to right the samples produced at 25 ℃ starting from a) 30 sec. B) 1 min. and c) 1 min and 30 sec.
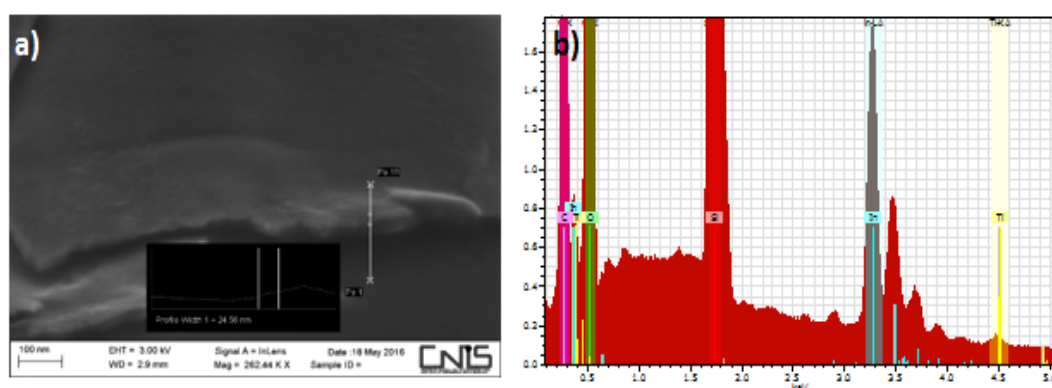
Fig. 3.11. a) On the right side we have a SEM photo of the samples that have been produced specifically the sample c) of the fig. 3.10. b) For each sample measured at SEM the surface was analyzed through the spectroscopy process, to understand the atomic percentages of the materials that made up the samples.

In fig. 3.11 b) we also have an analysis through atomic spectroscopy for the determination of the elemental composition of the sample, that is, of the structure and quantity of the atoms that compose it, regardless of the information on how the atoms are linked by forming molecules or on the crystalline structure of the material. I-V characterizations were made and shown in fig. 3.12. On these samples, we had a behavior not properly resistive. Furthermore, we do not have a solid substrate, but a polymeric substrate on which silver strips have been used for measurements to prevent probe tips from piercing the thin substrate and thus nullifying the

measurement. The measurements were made considering a voltage range between -10 V and +10 V with a 0.5 V step and a compliance of 10 mA. For each voltage value 3 measurement values were acquired. The minimum and maximum resistance values were 1315.78 Ω and 2857.14 Ω while for the resistivity we had the minimum and maximum of 27865 Ω / sq and 50057 Ω / sq, as shown in fig. 3.12.
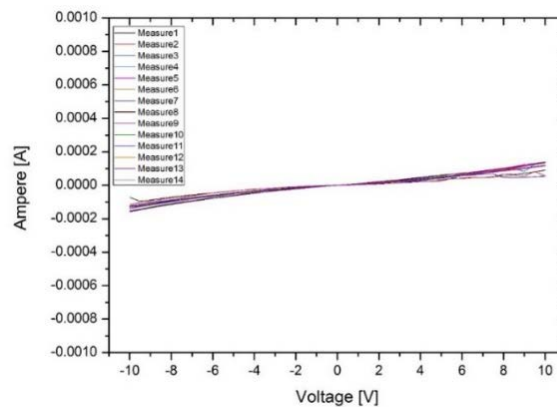
Fig. 3.12. I-V characteristic of a sample with a thin ITO film, sputtered at 25 ℃ for 30 sec.

3.3.4 Chromium (Cr)

The Cr samples were manufactured only at a temperature of 25 ℃. As in the previous case of the ITO, we tried not to expose the samples to temperatures above 25 ℃ in order to avoid thermal expansion of the PDMS. As you can see from the fig. 3.13 a) there is a uniformity from the surface of the Cr on the PDMS then confirmed by the SEM analysis. Four samples were produced at a temperature of 25 ℃ with different exposure times of 2 min. and 4 min. for couples. From image of fig. 3.12, of one of the various samples deposited at 25 ℃ for 4 minutes, the deposition rate is

about 25 nm every minute because, after examining this SEM sample, a thickness of 100 nm was obtained.
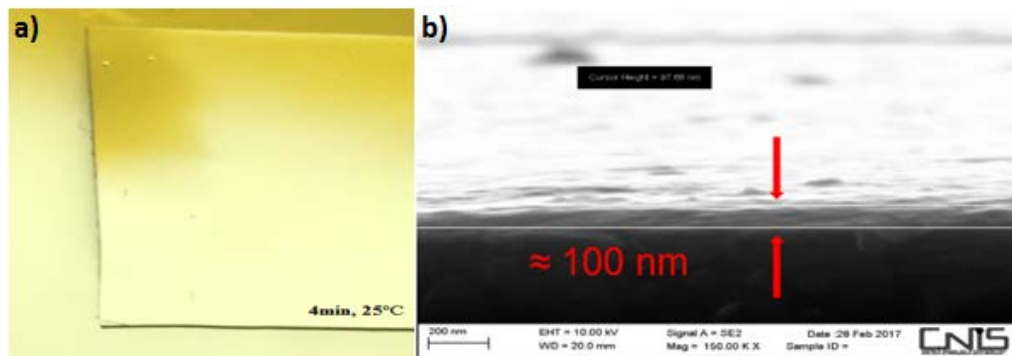
Fig. 3.13 a) The sample was produced with a deposition time of 4 min at room temperature of 25 °C. b) Photo taken at SEM of a deposition of 100 nm of Cr on a PDMS substrate.

The uniformity of the Cr surface on the PDMS resulted in having a purely resistive behavior on all the fabricated samples and on which I-V measurements were made, as shown in fig. 3.14. The voltage range ranged from 0 V to 15 V with a step of 0.1 V and a compliance of 50 mA. The number of acquisitions per sample was 3 from which resistance and resistivity values were obtained equal to 4945.63 Ω and 0.5 Ω / sq.
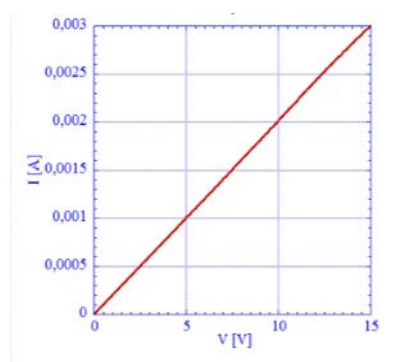
Fig. 3.14. I-V measurement of the Cr sputtering deposition at 4 min of CR at 25 °C of 100 nm.

3.3.5 Electroplating

When a metal M is immersed in an aqueous solution containing ions of that metal, M^{z+}, an exchange of metal ions will take place between the metal M and the ions of the solution, or M^{z+}, ions from the crystalline lattice enter the solution and some ions from the solution enter the crystal lattice [3], [63], [81-85]. One of these reactions can occur faster than the other one. In this case if there is an excess of electrons on the metal, the metal acquires a negative charge. In response to the charge of the metal side, there is a rearrangement of the charges on the side of the solution. The negative charge on the metal M attracts positively charged ions from the solution and rejects negatively charged ions A^{z-}, resulting in an excess of positive ions M^{z+} in the solution. Thus, in this case, on the side of the solution, it acquires opposite and equal charge q_s^+, defined as the charge per unit of surface on the solution side of the interphase. Positive charge on the solution side slows down the velocity of M^{z+} ions leaving the crystal lattice due to repulsion and accelerates the rate of ions entering the crystal lattice. After a certain period of time a dynamic equilibrium will be established between the metal M and its ions in the solution:

$$M^{z+} + ze \rightleftarrows M \qquad\qquad (3.1)$$

where z is the number of electrons involved in the reaction. An example of a galvanic process is shown in fig. 3.15. The same number is inserted at the dynamic equilibrium, and the same number of ions leaves the crystal lattice:

$$\vec{n} = \overleftarrow{n} \tag{3.2}$$
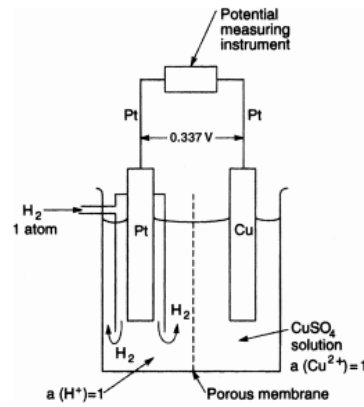
Fig. 3.15 Relative standard electrode potential E0 of a Cu/Cu2+ electrodes [40].

The interphase region is neutral to equilibrium:

$$q_M = -q_S \tag{3.3}$$

The result of the recharge of the interphase is the difference in potential: $\Delta\Phi$ (M,S) between the potentials of the metal Φ_M, and the solution Φ_S:

$$\Delta\phi(M,S) = \phi_M - \phi_s \tag{3.4}$$

When an electrode is part of an electrochemical cell in which current flows, its potential will be different from the equilibrium potential. If the electrode's potential equilibrium (potential in the absence of current) is the potential of the electrode itself, the current flow is therefore the difference between the electrode and electrode's potential:

$$\eta = \overline{E}(l) - \overline{E} \tag{3.5}$$

It is called "overpotential". For very high negative values of ($\eta > 100$ mV) the current density $I = \frac{l}{S}$, where S is the area of the electrode surface increases exponentially:

$$I = -I_0 e^{-a \cdot z \cdot f \cdot \eta} \qquad (3.6)$$

and for the great positive values of η (anodic processes) we obtain:

$$I = -I_0 e^{(1-a) z \cdot f \cdot \eta} \qquad (3.7)$$

where I_0 is the exchange current density, $I_0 = I$ when $\eta = 0$, the current density is linked to a transfer coefficient F called the Faraday constant, R the gas constant, T the absolute temperature from which:

$$f = \frac{F}{RT} \qquad (3.8)$$

When an electrode is in equilibrium, there is a constant exchange of charge carriers, electrons or ions, between the solution and the metal. At 25 ° C we have:

$$f = \frac{96487 \ [C \cdot mol^{-1}]}{8.3144 \ [J \cdot K^{-1}] \times 298 \ [K]} = 38.94 \ [V] \qquad (3.9)$$

The eq. (3.9) is called Faraday law which defines the amount of electrochemical reaction that occurs at an electrode and is proportional to

the amount of electrical charge Q passing through the electrochemical cell. If the weight of an electrolysis product is:

$$w = Z \cdot Q \tag{3.10}$$

Since Q is the product of the current in ampere and the elapsed time t in seconds we have:

$$Q = I \cdot t \tag{3.11}$$

$$w = Z \cdot I \cdot t \tag{3.12}$$

According to Faraday's law the production of an equivalent gram of a product to the electrode, immersed in an electrolytic cell, requires a charge of 96.487 C. It represents a mass of electrons and its value can be calculated from:

$$F = N_A \cdot e \tag{3.13}$$

where N_A is the Avogadro number. An equivalent, defined as w_{eq}, is that fraction of a reaction (atomic) molar unit that corresponds to the transfer of an electron. In general we have:

$$w_{eq} = \frac{A_{wt}}{n} \tag{3.14}$$

A_{wt} is the atomic weight of the metal deposited on the cathode and n the number of electrons involved in the deposition reaction. From the eq. (3.9) and eq. (3.11) it follows that when Q=1C or Q=1 A·s. The combination of eq. (3.12) and eq. (3.14) defines:

$$w = w_{Q=1} \cdot Q \tag{3.15}$$

The value of Z that can be evaluated as follows. Since 96.487 C are required for the deposition of an equivalent of a metal, w_{eq}, from eq. (3.14) follows that $w_{eq} = 96,487\ Z$ from which:

$$Z = w_{Q=1} = \frac{w_{eq}}{96,487} = \frac{w_{eq}}{F} \tag{3.16}$$

from eq. (3.16) $Z = \frac{A_{wt}}{nF}$ and therefore:

$$w = ZQ = \frac{A_{wt}}{nF}Q \tag{3.17}$$

Current efficiency CE is defined as the number of coulombs required for that reaction, Q_j divided by the total number of Coulombs passed:

$$CE = \frac{Q_j}{Q_{total}} \tag{3.18}$$

The thickness of the deposit can be assessed by considering the volume of the deposit. Since the volume V of the deposit is the product of the area of plated surface and the thickness h, it follows that:

$$h = \frac{V}{a} = \frac{w}{ad} \qquad (3.19)$$

In the case in which it is necessary to calculate the time t necessary to obtain the desired deposit thickness h at a given current density, the Faraday law was introduced in eq. (3.17), and in eq. (3.19) to obtain the thickness as a function of time:

$$h = \frac{V}{a} = \frac{ZQ}{ad} = \frac{ZIt}{ad} \qquad (3.20)$$

$$t = \frac{had}{ZI} \qquad (3.21)$$

Modern integrated circuits consist of thin-film layered structures subject to interdiffusion during the thermal processing step in manufacturing. The diffusion, not only in the case of thin films, is a thermodynamically irreversible process, and is defined as the tendency of two different gases to mix when they are separated by a porous partition. At equilibrium in a solid, impurities or vacant positions are evenly distributed. In solids, for example, the chemical potential is identified with the Fermi energy level. When two solids or thin films are put into contact, as in the case of a p-n junction, the charged particles will be interdiffused in such a way that the chemical potentials or Fermi levels are balanced. The same movement of

charges takes place in the galvanic processes thanks to the difference in concentration between the aqueous solution and the cathode. Gold easily forms alloys with other metals during the deposition process or by diffusion with the gold substrate on which it has been plated. For this reason, I used a thin layer of nickel of about 100 nm before the deposition of gold on copper, as depicted in fig. 3.16. It was produced with a current of 300 mA for 30 seconds. This step is a further step in the production of co-planar gold electrodes without the characteristics of this material being able to degrade with a less noble metal such as copper (Cu).

Fig. 3.16. The photo shows a 100 nm layer of nickel so that the gold produced can not be contaminated, in the galvanic process, with a copper substrate.

The gold deposits can be, using chemical terms, hard or soft, opaque or luminous, depending on the impurities and deposition conditions. Excessively high concentrations of gold in the baths are to be avoided due to the cost of the gold lost during the drag-out of the salt. During the galvanic processes two parameters are very important: brightness and adhesion. The brightness of a surface is defined as the optical reflective power of the surface. It is measured by the amount of specularly reflected light. Adhesion can be considered as the degree to which a bond has been

developed from one point to another to the coating-substrate interface. The strength of this bond should be equal to or greater than the cohesive strength of the weaker of the two materials involved. There are several accepted methods to evaluate the adhesion of electroplated coatings that is higher between metals than between metals and plastics. In general, the coating is removed mechanically and, where possible, the tests must be carried out with the production elements rather than with the test samples, such as the Ollard gluing test. It consists in applying a load to separate the deposit from the substrate and is indicative of the adhesion force [40].

3.3.6 Gold Plating

Gold exists mainly in the oxidation states +1 and +3. In term IUPAC Au (I) and Au (III) the most important ion for electrodeposition is [Au(CN)2]-. The stability of the cyanide complex present in Au (I) is reflected in the shift of the reduction potential for the Au (I) from 1.71 V to 0.611 V. In this case we have that the stability constant is $K = 10^{39}$. Two other solutions of gold that are interesting for electro-deposition are gold sulfite $K = 10^{10}$ and gold thiosulfate $K = 10^{28}$:

$$Au^+ + 2CN^- \rightarrow [Au(CN)_2]^- \qquad K=10^{39} \qquad\qquad (3.22)$$

$$Au^+ + 2S_2O_3^{2-} \rightarrow [Au(S_2O_3)_2]^{3-} \qquad K=10^{28} \qquad\qquad (3.23)$$

$$Au^+ + 2SO_3^{2-} \rightarrow [Au(SO_3)_2]^{3-} \qquad K=10^{10} \qquad\qquad (3.24)$$
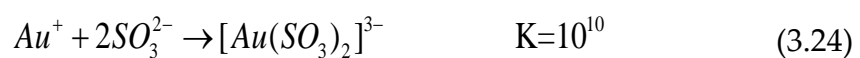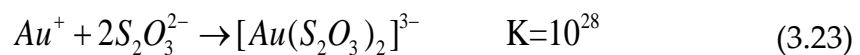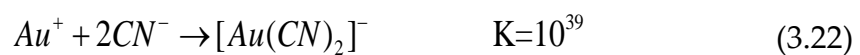
There are numerous baths and gold-plated additives used in industry. The cyanide baths were the most used baths and were divided into three classifications: the alkaline-gold-cyanide bath (pH> 8.5), the buffered acid baths (pH between 1.8 and 6) and the neutral, i.e. the cyanide bath buffered gold (pH between 6 and 8.5). Currently they are no longer used because of the present cyanide for which a fourth group of plating baths can be defined with the presence of thiosulphates and sulfites instead of cyanide. The pH range between 8 and 10 is a critical region because the pK_a hydrogen cyanide is 9.46 which determines the stability of the solution, the equilibrium constant for HCN (aqueous) which goes to HCN gr. is 101.4, making the pK_a for HCN gr. is 8.06:

$$HCN(g) \rightarrow H^+ + CN^- \qquad \text{pK}_a = 8.06 \qquad (3.25)$$
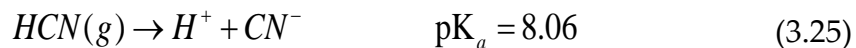
At pH <8, the predominant form of cyanide is HCN (g), which evolves as a gaseous product. HCN gas is highly toxic and its evolution from galvanic baths is a health problem. The presence of significant concentrations of free cyanide in the bath like in the case of alkaline baths, is also a health risk because of the risk of ingestion. For this reason, in my electrodepositions, I used a thiosulfites solution instead of the cyanide solution. The operational parameters of commercial baths based on gold sulfite have been presented with particular attention to the effect of the plating temperature and of the current density on the residual stresses in the deposited metal. Although, the sulfite Au (I) has been used in commercial baths but the complex is susceptible to disproportion, forming Au (III) and metallic gold. This spontaneous decomposition of the bath led the commercial baths to use patented stabilizing additives. Gold sulfite Au (I)

is particularly unstable for pH < 7 where sulfite is transformed to form bisulfite. The thiosulphate of gold Au (I) has a stability constant pK_a 10^{28} which is included in Au (I) sulfite and Au (I) cyanide. The thiosulphate complex is stable in weak acidic solutions due to the pK_a with low thiosulphate. The thiosulphate-only complex is dominant with a low pH.

$$H_2S_2O_3 \rightarrow H^+ + HS_2O_3^- \quad \mathrm{pK}_a = 0.3 \tag{3.26}$$

$$HS_2O_3 \rightarrow H^+ + S_2O_3^{2-} \quad \mathrm{pK}_a = 1.7 \tag{3.27}$$

It has been shown that the reduction of Au (I) thiosulfate has a global reaction that produces thiosulfate and gold:

$$[Au(S_2O_3)_2]^{3-} + e^- \rightarrow Au + S_2O_3^{2-} \tag{3.28}$$
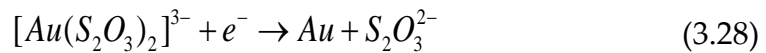
The effect of mixed thiosulphate-sulfite electrolytes has been studied to produce gold deposits suitable for forming gold tracks on integrated circuits and in electronic interconnections. The composition of the baths is as follows 3.17 [77]:

$NaAuCl_4 \cdot 2H_2O$	0.06 M	Gold as metal	10 g L^{-1}
Na_2SO_3	0.42 M	Sulfide	70 g L^{-1}
$Na_2S_2O_3 \cdot 5H_2O$	0.42 M	Thiosulfate	70 g L^{-1}
Na_2HPO_4	0.03 M	Additives	10 g L^{-1}
Tl^+ (added as Tl_2SO_4)	0.03 M		
pH	6	pH	5
Temperature	60°C	Temperature	50°C
Current density	5 mA cm^{-2}		

Fig. 3.17. Typical baths are represented with which the galvanic processes of gold deposition are carried out [81].

3.3.7 Sample fabrication by galvanic process

For the production and characterization of the samples with gold electrodes, I used a 24 carat gold solution produced by Coswell. The characteristic of this solution was that it did not contain the cyanides for the stabilization of the solution's pH, but thiosulphates and sulfites. For the production of electrodes, the process defined in fig. 3.18 as followed: I started with 2cm copper squares per side on which a sanding process was carried out to make the surface as smooth as possible. Subsequently, a micrometric layer was deposited on the copper surface through a transition to the spin coating, depending on the design requirements, a photoresist layer which in my case was the AZ 9260 representing the channels to be filled with the LC. The sample was made to pass a soft bake at 100 ℃ for one minute after which the desired pattern was transferred through a photolithographic passage. The maximum value that I was able to obtain for the width of the channels was 10 µm fig. 3.19.
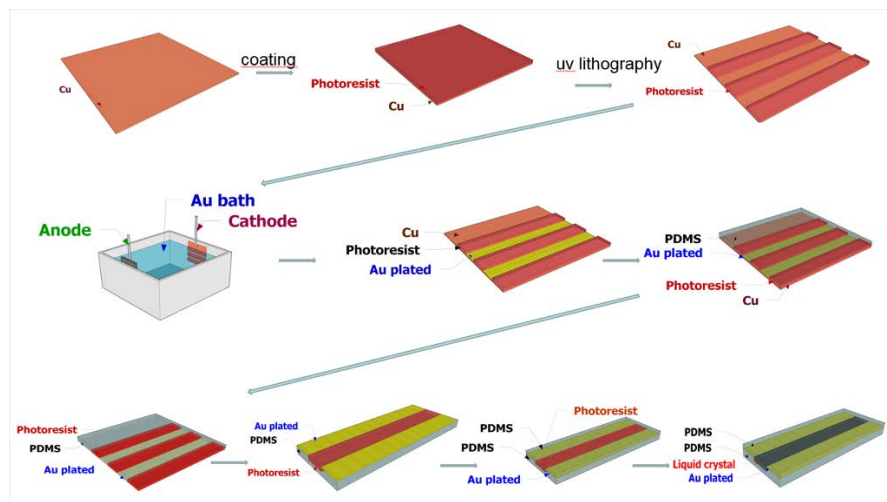
Fig. 3.18. The electrodes are produced by using a squared substrate of copper of 2x2 cm, merged in a gold plating bath with different currents from 4 mA to 16 mA applied for two different times 30 min and then for 1 hour [3].
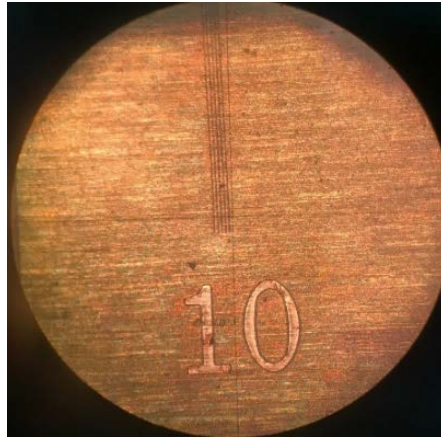
Fig. 3.19. The photo shows a set of 5 guides with a width of 10 μm with a separation of

10 μm.

From this step, the photoresist was removed through the specific remover, the AZ B351, and the sample ready for the bath was obtained in the solution with the gold salts. In the solution, a current variable between 4 mA and 16 mA was made to run for two different timings between 30 minutes and 1 hour. This resulted in a deposition of the gold layer that varied between 500 nm and 2 mm having calculated the thicknesses through eq. (3.20) and eq. (3.21). In an empirical way, I discovered that with a magnetic stirrer, the process was improved because there were no hydrogen bubbles at the photoresist strip that defined the channels and compromised the uniformity as shown in the fig 3.20 a) and b). This was due to the composition of the gold solution which corrodes the photoresist, which together with the current value used during the process moves an enormous volume of charges from the solution towards the cathode. The greater the current value, the more bubbles will be formed around the photoresist, the greater the value of the rpm to rotate the magnetic stirrer so that they do not have time to develop around the photoresist and jeopardize the creation of the channel or the channels as shown in fig. 3.21.
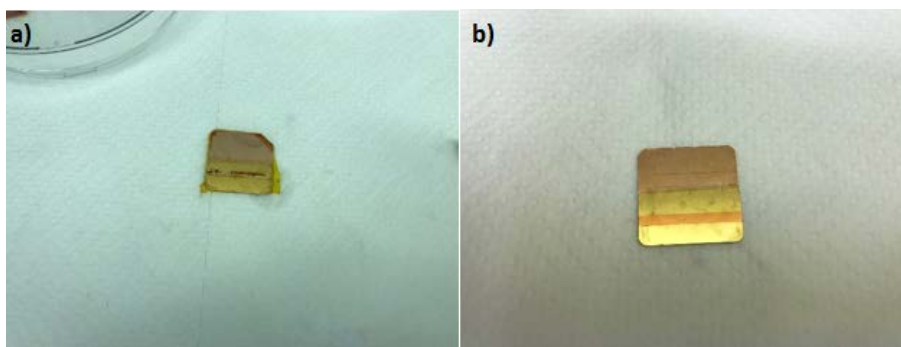
Fig. 3.20. a) A sample made without the use of a magnetic stirrer, while in b) another sample using the magnetic stirrer.

The samples thus produced were coated with cured PDMS and then fired at a temperature of 100 ℃ for 1 hr. To eliminate the copper substrate, I used ferrous chloride in fig. 3.21 a) or copper chloride in fig. 3.21 b). For my samples, I initially used ferrous chloride at a temperature of 50 ℃ with and without magnetic stirring, but in both cases there was an exfoliation of the newly created layer of gold as depicted in fig. 3.21 a). The photoresist, as mentioned, will define the guide to be filled and once removed, there will be depressions in the structure of the PDMS.
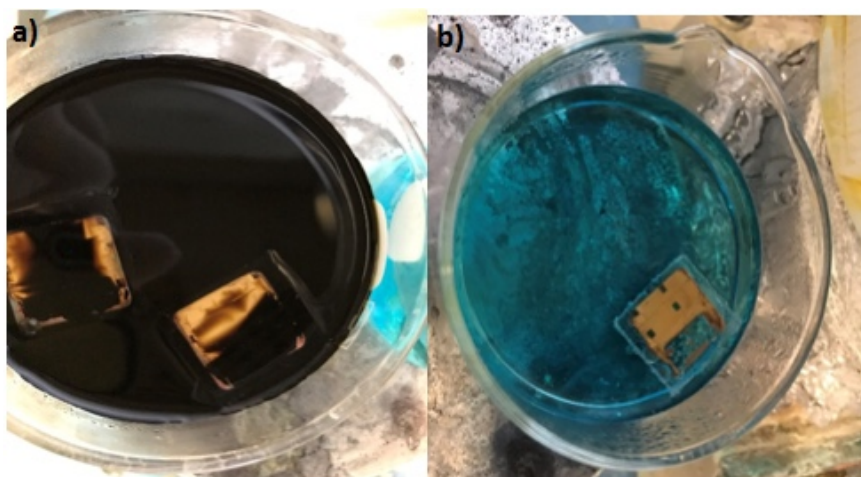
Fig. 3.21. a) Prototypes immersed in a) ferric chloride and b) ammonium perchlorate.

All the solutions I have used lead to the formation of hydrogen bubbles. As a consequence, the possible superficial detachment of the gold from the PDMS can occur due to the detonations of these bubbles. To avoid this, I used ammonium persulphate, which in addition to being less aggressive than ferric chloride and copper chloride, has a natural indicator of the level of incision changed through the transparency of the solution in transparent blue, which reflects the fact that the incision has occurred completely. This also means less mechanical stress on the structure when I have to take the sample to examine whether the incision process is complete or not. Subsequently the photoresist was removed with acetone bath and I closed my structure through another PDMS stick made from a silicon substrate on which four strips of graphite were placed through which I went to make some tests of continuity electric, as can be seen from the fig. 3.22 a) and b).
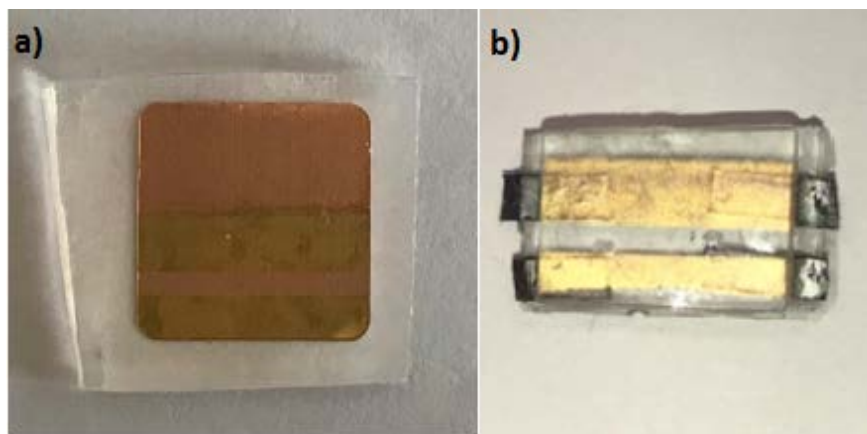
Fig. 3.22. a) Sample covered with the PDMS. In b) first sample produced to verify the continuity of the deposited gold layer.

I fabricated prototypes to be filled with the LC. As shown in fig. 3.23) the LC used for the tests carried out and for the switching was the 5CB, since that was available at the moment in the laboratory. In this case the

electrodes were contacted by tin soldering and two PDMS loops were placed over the structure to maximize the likelihood of filling and operating the device. As shown in fig. 3.24 a) and b), there is switching of the LC for voltage values of just 2 V. The maximum voltage value at which the LC were subjected was 10 V.
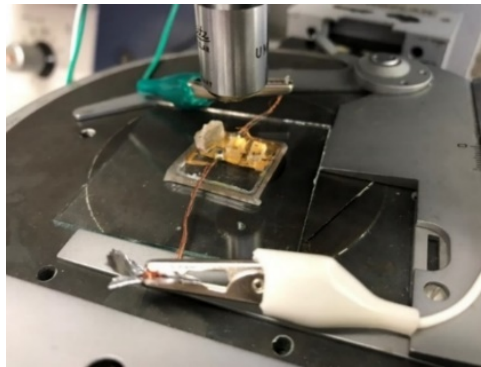
Fig. 3.23 Measurement set up for the reorientation of 5CB LC molecules diffused by capillarity in the device.

The sample observed under an optical microscope does not seem to have homeotropicity. This is probably caused by the contact with the gold layers which do not give perpendicular positioning when they come into contact with only walls of the PDMS.
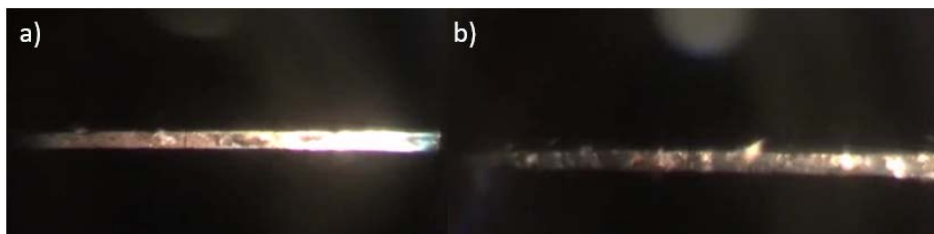
Fig. 3.24. Photo taken with a polarizing microscope showing a guide with a width of 38.1 μm in which LC was infiltrated by capillarity. a) In this case there is no voltage applied to the device. b) When the voltage is applied at the device there is re-orientation of the LC molecules.

Conclusions

It is possible to realize polymer guides (PDMS) filled with LC (LC), hence the name LC: PDMS technology. The manufacturing process of prototypes of optical waveguides in LC: PDMS technology is a process that starts from the creation of appropriately designed masks, through specific programs such as Autodesk Autocad® and through lithographic processes, common to microelectronics. The characterization of the samples produced in the laboratory resulted in an independence of the polarization of the incoming wave. A variation of the transmission of 0.35 due to the orientation of the LC and an estimated loss in transmission of $8 \frac{dB}{cm}$ [15], probably due to a series of issues including a not perfect matching of the LC:PDMS waveguides with the input and the output of the optical fibers, a not perfect arrangement of the LC molecules as medium and scattering of the silicon atoms present on the surfaces of the walls of the PDMS channels.

Chapter 4: Simulations of LC:PDMS waveguides

4.1 Overview

The simulations reported in this thesis were performed on the complementary use of two software: COMSOL Multiphysics® and BeamPROP®. Using the first software, I simulated the orientation of LC (LC) using the energy minimization equation of Oseen-Frank. The values extracted from these simulations were then processed through the use of Matlab® so they could be read correctly by the BeamPROP® simulator in order to design optical devices. The COMSOL Multiphysics®' version used was 5.3a because it includes new modules specifically designed for wave optics. I simulated the re-orientation of the LC molecules with and without the presence of an electric field applied to co-planar electrodes in an optofluidic channel.

4.2 Introduction to Finite Element Method

The finite element method (F. E. M.) [86-89] on which COMSOL Multiphysics® is based is a numerical technique for finding approximate solutions to problems described by differential equations on partial derivatives, reducing them to a system of algebraic equations. In general, the F.E.M. is suitable very well to solve partial differential equations when the domain has a complex form, it is variable, the accuracy required for the solution is not homogeneous on the domain, and when the searched solution lacks regularity. F.E.M. is applied to physical bodies that can be

subdivided into a number of parts, even very large. In the continuous, every single finite element is considered through a numerical integration of homogeneous characteristics. The main feature of F. E. M. is the discretization through the creation of a grid (mesh) composed of primitives (finite elements) of encoded form (triangles and quadrilaterals for 2D domains, tetrahedra and hexahedrons for 3D domains). On each element characterized by this elementary form, the solution of the problem is assumed to be expressed by the linear combination of certain functions called "shape functions". In some cases, the function can be approximated and the values will not be necessarily calculated in the points of interest, but the values provide the least amount of errors on the whole solution. The typical example refers to polynomial functions and the number of coefficients that identifies the solution on each element is therefore linked to the degree of the chosen polynomial which, in turn, governs the accuracy of the found numerical solution. In its original form, and still more widespread, the finite element method is used to solve linear problems, such as stress problems, deformations in the elastic field, or the diffusion of heat inside a material or body. Some more refined solutions allow to explore the behavior of materials even in the non-linear field, assuming plastic or visco-plastic behaviors.

4.3 Introduction on Beam Propagation Method

Regarding the simulation of light propagation in optoelectronic devices, I used the Synopsys BeamPROP®. It is based on the method of approximation of the propagation of the electromagnetic wave [91-94] in

optical devices in which the refractive index has a slow variation. The mathematical method is based on the parabolic equation (PE) also used in underwater acoustics. When a wave propagates along a waveguide for a long distance, longer than the wavelength, performing a strict numerical simulation is very difficult. The Beam Propagation Method (BPM) is based on approximate differential equations involving only a first order derivative in the variable. The derivative is performed with respect to the propagation axes representing the axis in which the waveguide propagates and can be resolved through "initial" value problems. The "initial" value is a function of time but not in the spatial variable. If we consider the propagation of high-frequency beams through an inhomogeneous medium such as LC molecules, we can consider scalar wave equation derived for the TE or TM modes separately:

$$n^2(r) \nabla^2 \phi + k^2 \cdot n^2(r) = 0, \qquad (4.1)$$

In which Φ represents the scalar field and $n^2(r)$ is used to indicate the refractive index and k is the wave number of the vacuum. If the refractive index n^2 can be split in two parts: unperturbed n_0^2 and perturbed Δn^2 we can have:

$$\nabla^2 \phi + k^2 \cdot n_0^2(r) \cdot \phi = -k^2 \cdot \Delta n^2(r) = p(r) \qquad (4.2)$$

In which p is considered as a source function. The combination of the radiation conditions at infinity and the wave equation defines a specific refractive index where through the Helmholtz equation can be solved.

$$\nabla^2 \psi + k^2 \cdot n_0^2(r) \cdot \psi = 0 \qquad (4.3)$$

If there is a solution of ψ for $z = z_0$, the derivative of $\frac{d\psi}{dz}$ can be calculated for all values of z, that is the axes among which the waves propagate, and also:

$$\frac{d\psi}{dz} = \bar{a}(x, y, z_0) \qquad (4.4)$$

The operator $\bar{a}$ is perpendicular to the transverse coordinate (x, y). If the n_0 is constant the $\bar{a}$ operator can be calculated in the angular-spectrum domain such as:

$$\Psi(k_x, k_y, z) = \int\limits_{-\infty}^{+\infty} \int \psi(x, y, z) e^{\left[-j(k_x \cdot x + k_y \cdot y)\right] dxdy} \qquad (4.5)$$

The relationship between the ψ and $\frac{d\psi}{dz}$ is given by:

$$\frac{d\psi}{dz}(k_x, k_y, z) = -j \cdot (k^2 \cdot n_0^2 - k_x^2 - k_y^2)^{-1/2} \cdot \Psi(k_x, k_y, z) \qquad (4.6)$$

From this equation, the operator $\hat{a}$ can be obtained. If we consider the beam propagation along the $\hat{z}$ axis, we can split the field Φ in two parts: ϕ_1 generates in the region where $z' < z$, and ϕ_2 where $z' > z$, so these conditions define that:

$$\phi = \phi_1 + \phi_2 \qquad (4.7)$$

The explicit expression to describe ϕ_1 and ϕ_2 is:

$$e_1(r \mid r') = \begin{cases} 0 & \text{for } z < z' \\ 1/2 & \text{for } z = z' \\ 1 & \text{for } z > z' \end{cases} \tag{4.8}$$

If G is the Green's Function of eq. (4.3) ϕ_1 can be expressed as follows:

$$\phi_1(r) = \int\limits_{-\infty}^{+\infty}\int\int G(r \mid r') \cdot e_1(r \mid r') \cdot p(r') dV' \tag{4.9}$$

The derivative is:

$$\frac{d\phi_1}{dz} = \int\limits_{-\infty}^{+\infty}\int\int \frac{dG}{dz}(r \mid r') \cdot e_1(r \mid r') \cdot p(r') dV' + \int\limits_{-\infty}^{+\infty}\int\int G(r \mid r') \cdot \delta(z - z') \cdot p(r') dV' \tag{4.10}$$

The first integral represents the propagation of the wave in an unperturbed medium, and can be rewritten in function of the operator $\bar{a}$ such as $\bar{a} \cdot \phi_1$ and the second integral can be rewritten as follows:

$$\int\limits_{-\infty}^{+\infty}\int G(x,y,z \mid x',y',z') \cdot (-k^2)^{i\theta} \cdot \Delta n^2(x',y',z) \cdot \phi(x',y',z) dx' dy' \tag{4.11}$$

This expression can be seen as an operator $\bar{b}$ who operates on φ with respect to the transverse coordinate $\bar{b} \cdot \phi$. We obtain that:

$$\frac{d\phi_1}{dz} = \bar{a} \cdot \phi_1 + \bar{b} \cdot \phi \tag{4.12}$$

If we neglected the influence of the reflected field ϕ_2 on ϕ_1 the eq. (4.12) can be written as:

$$\frac{d\phi_1}{dz} = \overline{a} \cdot \phi_1 + \overline{b} \cdot \phi_1 \qquad (4.13)$$

The eq. (4.13) defines an important approximation and defines the operational condition of using the beam propagator method. This excludes the use of BPM in cases in which, for example, the refractive index changes abruptly. Compared to the first version of this simulation, a series of new algorithms have been introduced to improve the calculation of the electromagnetic wave propagation, which are based on the "paraxial one way model". It is necessary to discretize along the variable through the diagonal approximations of Padé before obtaining results through the paraxial one way model. When evanescent waves outside of the guide are evaluated, these approximations have defects. In the theory of electromagnetism, the evanescent waves should tend to zero at the time they propagate outside the waveguide. For this reason, there are now functions called "rational approximations" that can suppress evanescent modes. We decided to use BeamPROP® as it guarantees design and simulate both passive and active photonic devices and it uses extremely precise algorithms to enable rapid virtual prototyping, reducing the need to fabricate many physical devices [90-93].

4.3.1 Monte Carlo Simulations

In collaboration with Prof. C. Zannoni and Dr. Paolo Pasini we studied the molecular orientation of the LC in LC:PDMS devices [94-95]. As

anticipated in the previous chapter, LC are materials that have the crystalline properties of solids and the fluidity of liquids. These materials can show transitions between several phases. The most studied phases of the LC are the isotropic and nematic phases. The isotropic phase does not show any translational or orientational order, while the nematic phase exhibits a short-range orientational order. This last transition is the most relevant in many technological applications. LC systems show interesting dynamic properties. The Monte Carlo model is one of the founding pillars of computational science, in fact it can be applied in chemistry, physics, and biology and it also finds application in their related fields. The Monte Carlo method is mainly used in three classes of problems: optimization of specific calculations, numerical integration, and generation of drawings from a probability distribution. In statistical chemistry, through the Monte Carlo method, it is possible to study molecular dynamics and calculate the theories on the statistical field of simple systems of particles and polymers. The concept behind the Monte Carlo model is to use randomness to solve problems that could be deterministic in principle. These problems are often very difficult or impossible to solve by traditional approaches. In problems related to the fields of physics or chemistry, Monte Carlo methods are useful for simulating systems with many degrees of freedom, such as fluids, disordered materials, strongly coupled solids and cellular structures or kinetic gas models. In principle, Monte Carlo methods can be used to solve any problem with a probabilistic interpretation. According to the law of large numbers, the integrals described by the expected value of some random variables can be approximated by taking the empirical average or sample mean of independent samples of the variable [94]. Phase transitions can be studied through the Lebwohl-Lasher (LL) model,

a minimal lattice LC model whose simplicity has attracted significant research. The molecules of LC, or clusters of strictly ordered molecules, are represented by vectors of three-dimensional units ("spin"). The spins have a fixed position in the lattice sites and have freedom of rotation, but are subject to an intermolecular potential, so that this restriction does not affect their radius guidance system. The main advantage in using reticular models is having a great number of particles that can be treated compared to other systems. The microchannel boundary conditions are represented considering an outer particle layer with a fixed orientation. This orientation will be homeotropic on all the walls of the simulated microchannel. The conditions along the canal will be defined through periodic conditions. These spins interact through a Hamiltonian given by:

$$H = -\varepsilon P_2 \cdot (u_i \cdot u_j) \tag{4.14}$$

Where P_2 is the second Legendre polynomial, u_i u_j are unit vectors along the axis of the two particles, and ε is an energy parameter that measures the interaction strength between neighboring molecules. The Lebowohl-Lasher model possesses a phase transition at a dimensionless temperature: $T^* = \frac{kT}{\varepsilon} = 1.1232$ [95].
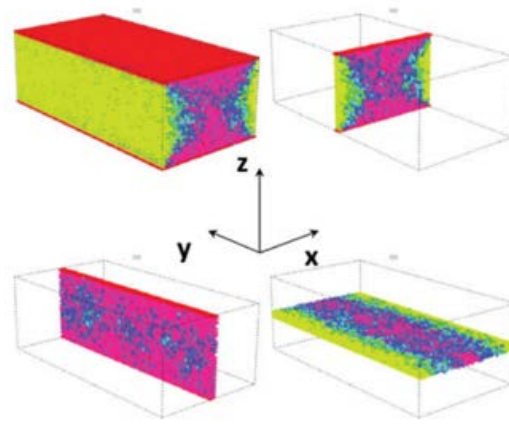
Fig. 4.1. A 80×80×26 cell. The color code indicates the spin orientations with the red one denoting the alignment along z. In the top left image shows the overall molecular organization whereas the other three images are cross sections taken at the middle layer of each plane ($\widehat{xz}$, $\widehat{xy}$, $\widehat{yz}$) respectively (clockwise) [95].

We have performed a set of independent complete simulations for cell mimicking a microchannel of a straight waveguide of size $L_x \times L_y \times L_z$. Keeping fixed $L_z = 26$ μm and $L_y = 80$ μm, we have considered $L_x = 40, 60, 80, 120$ μm, where the cross sections of the microchannel are rectangular [95].

Fig. 4.2. The simulated polarized optical images as obtained by Monte Carlo simulations for microchannel of various width (L_x), for light transmission along $\hat{y}$ (front view on the left) and along $\hat{z}$ direction (top view on the right) [95].

The molecular organization of the structure obtained is in good agreement with experimental results in absence of external field, and also can provide predictions for the optical polarized images between crossed polarizers which should be obtained by real experiments as shown in fig. 4.3.
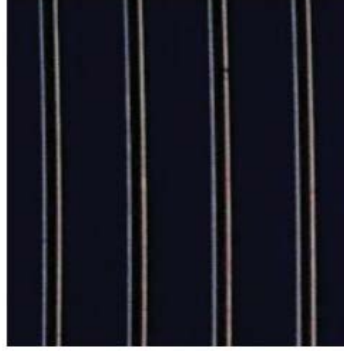
Fig. 4.3. A polarizing microscope image of LC:PDMS waveguides with a homeotropic alignment channels obtained for a fabricated device [10].

We have also investigated the effect of the application of a uniform electric field F on the microchannel. The field, coupled dielectrically to the particles, is modelled as sum over mesogenic spins of individual terms:

$$U_i = -\xi_i P_2(u_i \cdot F) \tag{4.15}$$

The strength of the coupling to the field, denoted by the term ξ_i, is proportional to the dielectric constant anisotropy and to the field intensity. Here we consider microscopic cells and we assume the field to be uniform throughout the sample, so that $\xi_i = \xi$. We also assume the LC to have positive dielectric anisotropy, like the common mesogens 5CB or E7, so that $\xi > 0$. We shall also consider a field applied transversally with respect to the channel direction: $F \| x$. We have simulated in this case two lateral size of the cell, $L_x = 40$ μm and $L_x = 80$ μm, keeping fixed the other

dimensions L_y = 80 μm and L_z = 26 μm and various values of the field strengths, i.e. ξ = 0, 0.01, 0.02, 0.03, 0.04 and 0.05, shown in fig. 4.4.
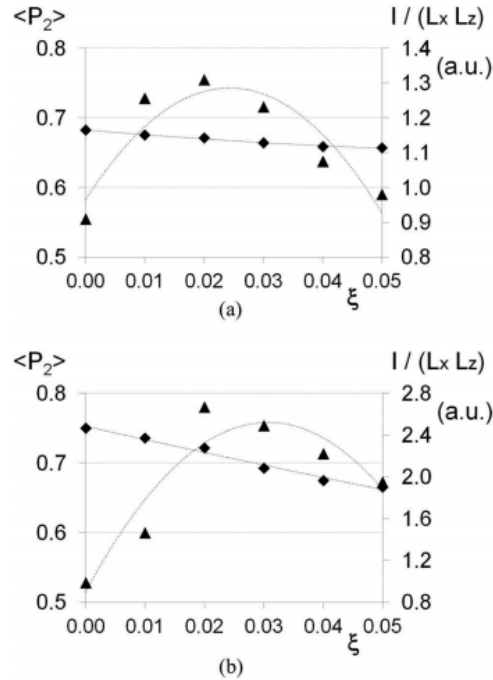
Fig. 4.4. Transmitted light intensity (triangles) vs field strength ξ. The results are depicted for a) 40 × 80 × 26 μm and b) 80 × 80 × 26 μm. $< P_2 >$ (diamonds) is the nematic order parameter [95].

During the second year of my Ph.D. course, I participated in the international COST ICT-2018 program as a visiting student at the Physics department of the Polytechnic University of Warsaw in the research group of Prof. Wolinsky. During my stay at the physics department, in collaboration with Prof. Rutkowska, I had the opportunity to explore possible solutions for the creation of optofluidic devices controlled through co-planar electrodes. I tested optofluidic prototypes and subsequently filled my samples with different LC: 6CHBT and 5CB. Unfortunately, they did not have a vacuum oven as in my department and therefore many of the ones that I created did not have the guides

completely filled. This partially cancelled the characterization of these LC. The samples in fig. 4.5 were filled with the 5CB crystals and were examined using a VHX 5000 electron microscope [96].
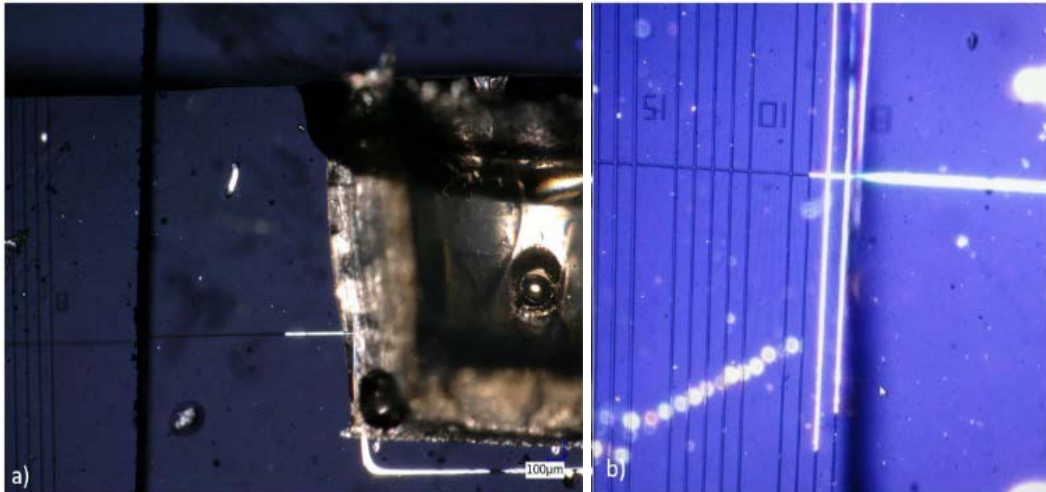
Fig. 4.5 a) and b) PDMS prototype filled with 5CB. The picture was taken with an digital microscope [96].

Differently from my simulation in COMSOL Multiphysics®, based on the quadratic Euler method, the group led by Prof. Wolinsky used proprietary scripts realized in Matlab™ and based on the Euler-Lagrange method. In the model, the relaxation pattern of the finite difference was applied considering the homoeotropic behavior of the LC molecules on the PDMS walls, to minimize the free energy described by the Oseen-Frank equation in which the contribution of the electric field was also introduced.

4.3.2 Alternative-Direction Successive Over-Relaxation (ADSOR)

The ADSOR [97] method is a useful algorithm in fluidic simulations for all fluid problems. This method is based on the Successive Over Relaxation method. This algorithm is used to discretize the partial differential equations (PDE) often leads to a large sparse system of equations such as:

$$A\phi = b \qquad (4.16)$$

In matrix term, the successive over-relaxion iteration can be expressed as:

$$\phi^{(k+1)} = (D - \omega \cdot L)^{-1}(\omega \cdot U + (1-\omega) \cdot D) \cdot \phi^{(k)} + (D - \omega \cdot L)^{-1}b \quad (4.17)$$

where D, L, U represent the diagonal. Lower triangular, and upper triangular parts of the coefficient matrix A, k is the iteration count, and ω is the relaxation factor. This matrix expression is not usually used to program the method but an element-based expression is used:

$$\phi^{(k+1)} = (1-\omega) \cdot \phi_i^{(k)} + \frac{\omega}{a_{ii}} \cdot \left(b_i - \sum_{j<i} a_{ij} \cdot \phi_i^{(k+1)} - \sum_{j>i} a_{ij} \cdot \phi_i^{(k)} \right) \quad \text{i=1,2,....,n (4.18)}$$

Note that if ω=1 the eq. reduces to the Gauss-Seidel iteration. The choice of ω is not necessarily easy because depends from the coefficient matrix property. For a symmetric, and positive matrices it can be proven that 0< ω < 2 lead to converge [97].

4.3.3 Euler-Lagrange method

The Euler-Lagrange equations describe the motion of an object that obeys the second principle of dynamics, relating the position and speed of the mechanical system. Given the integral of a function of the form [97]:

$$I(\in) = \int_{t_1}^{t_2} F(U,\dot{U},t)dt \tag{4.19}$$

where t_1 and t_2 are arbitrary, U and $\dot{U}$ are given by:

$$U(t) = u(t) + \in \eta(t) \tag{4.20}$$

$$\dot{U}(t) = \dot{u}(t) + \varepsilon \cdot \dot{\eta}(t) \tag{4.21}$$

and ε is a real and independent variable. The U and u functions can describe the possible positions of a dynamic variable system in two temporal instants, t_1 and t_2. Where u(t) represents the position when the integral described in the eq. (4.20) is stationary and indicates one extreme and U(t) is u(t) plus one of its variations $\varepsilon \cdot \eta$(t). Assuming that η(t) is independent of u(t), then there is a function that makes the eq. (4.19) unique in the extremes t_1 and t_2. The functions u(t) and η(t) are class C². That is, they possess the second continuous derivatives with respect to t. The term η(t) must disappear for t $= t_1$, and t $= t_2$. that is, u(t) and U(t) coincide at the end points of the interval $[t_1, t_2]$, where t_1 and t_2 are arbitrary. The function is stationary if $U(t) = u(t)$, or $\varepsilon = 0$. If t_1 and t_2 are not in function of ε, the derivative of the function eq. (4.6) is:

$$\frac{dI(\varepsilon)}{d\varepsilon}\Big|_{\varepsilon=0}=\int_{t_1}^{t_2}\frac{dF}{d\varepsilon}(U,\dot{U},t)dt=0 \tag{4.22}$$

however:

$$\frac{dF}{d\varepsilon}(U,\dot{U},t)dt=\frac{dF}{dU}\cdot\frac{dU}{d\varepsilon}+\frac{dF}{d\dot{U}}\cdot\frac{d\dot{U}}{d\varepsilon} \tag{4.23}$$

If we substitute the eq. (4.19) in eq. (4.20) and impose $\varepsilon = 0$ we have:

$$\frac{dI(\varepsilon)}{d\varepsilon}\Big|_{\varepsilon=0}=\int_{t_2}^{t_1}(\frac{dF}{du}\eta+\frac{dF}{d\dot{u}}\dot{\eta})dt \tag{4.24}$$

Integrating by parts the eq. (4.24) we obtain:

$$\frac{dI(\varepsilon)}{d\varepsilon}\Big|_{\varepsilon=0}=\int_{t_1}^{t_2}\eta(t)\cdot(\frac{dF}{du}+\frac{d}{dt}\frac{dF}{d\dot{u}})dt+\frac{dF}{d\dot{u}}\cdot n(t)\Big|_{t_1}^{t_2} \tag{4.25}$$

The second term of eq. (4.25) vanishes because $\eta(t_1) = \eta(t_2)=0$ which defines:

$$\frac{dI(\varepsilon)}{d\varepsilon}\Big|_{\varepsilon=0}=\int_{t_1}^{t_2}\eta(t)\cdot(\frac{dF}{du}+\frac{d}{dt}\cdot\frac{dF}{d\dot{u}})dt=0 \tag{4.26}$$

and

$$\frac{dI(\varepsilon)}{d\varepsilon}\Big|_{\varepsilon=0}=\frac{dF}{du}-\frac{d}{dt}\cdot\frac{dF}{d\dot{u}} \tag{4.27}$$

If a differentiable functional is stationary at its local maxima and minima, the Euler-Lagrange equation is useful for solving optimization problems in which the function is sought by minimizing or maximizing it. Moreover, in order to speed up the calculation of the Euler-Lagrange integral through Matlab's script, it became necessary to implement the ADSOR scheme (Alternative-Direction Successive Over-Relaxation), a useful algorithm in fluidic simulations for all fluid problems. The electric field is generated by two types of electrodes: co-planar electrodes and in plane switch [96]. Instead, in my simulations, the electrodes are placed on the sides of the guide filled with LC for higher values of voltage applied, as depicted in fig. 4.6.
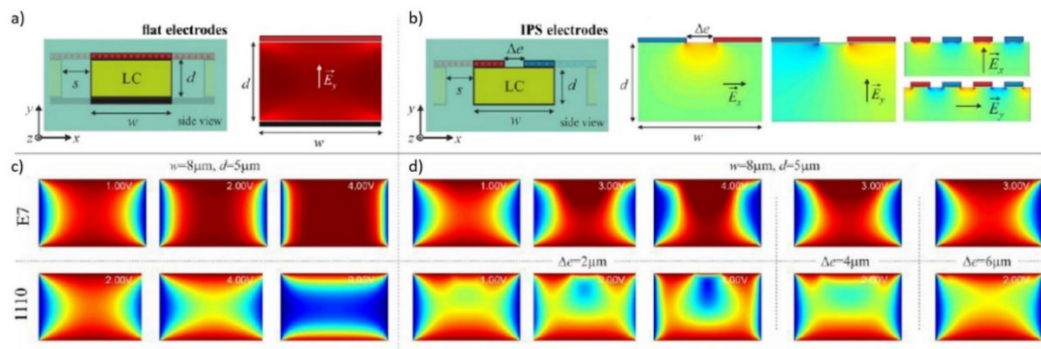
Fig. 4.6. a) and b) two different types of electrodes are represented with which to re-enter the LC molecules. c) and d) Reorientation of the molecules of LC E7 and 1110, infiltrated into PDMS channels, according to the potential applied to the electrodes. In the case of IPS, different gaps between the electrodes were simulated [96].

The simulations involved two types of LC: the E7 and 1110 both synthesized at the Military University of Technology in Warsaw. The NLC 1110 mixture is characterized by a low birefringence, $\Delta n = 0.046$ at the wavelength of $\lambda = 589$ nm and 20 °C and has a negative electrical anisotropy of $\Delta\varepsilon = 1.2$ at kHz frequencies. With regard to the LC E7, the values are $\Delta n = 0.264$ and $\Delta\varepsilon = 14.5$, respectively. The elastic constant used

in the calculations with an elastic constant approximation is equal to 20 pN. The previously defined ADSOR numeric scheme was combined with the multigrid (MM) method to calculate molecular re-orientation under the influence of an electric field. From the numerical simulations, calculated as a function of the angle θ, it is possible to find the spatial distribution of the effective refractive index within the NLC nuclei relative to the TE and TM polarization according to the following equation:

$$n_{TM,TE}(\theta) = n_e n_o [(n_{e,o}^2 - n_{o,e}^2)\cos^2\theta + n_{o,e}^2]^{-\frac{1}{2}} \qquad (4.28)$$

where n_e and n_o are the ordinary and extraordinary refractive indices, respectively. In order for the structure to be correctly simulated, the following steps are necessary [96]:

- calculation of the electrical potential for a given molecular orientation within the waveguide channels and for the geometry of the specific electrodes (ADSOR + MM);
- calculation of the distribution of the electric field in the region inside the electrodes. The values of the electric field along the x and y axes are calculated as the first derivatives of the potential applied to the electrodes.
- calculation of the molecular orientation under the influence of the applied electric field (ADSOR + MM) to solve the Euler-Lagrange equation.

4.4 Results of COMSOL simulations

4.4.1 Partial Differential Equations

Partial Differential Equations (PDE) [86] is an identity that relates the independent variables, the dependent variable u and the partial derivative of u. It can be written as:

$$F(x, y, u(x, y), u_x(x, y), \mu_y(x, y)) = F(x, y, u, u_x, \mu_y) = 0 \qquad (4.29)$$

This is the most general PDE in two independent variables of first order. The order of an equation is the highest derivative that appears. The most general second order PDE in two independent variables is:

$$F(x, y, u, u_x, \mu_y, u_{xx}, \mu_{yy}) = 0 \qquad (4.30)$$

An solution of a PDE is a function $u = (x, y, ...)$ that satisfies the equation identically, at least in some region of the x, y,… variables. When solving an ordinary differential equation (ODE), one sometimes reverses the roles of the independent and the dependent variables, for the separable ODE $\frac{du}{dx} = u^3$. For the PDE the distinction between the independent variables and the dependent variables ("the unknow"), is always maintained. If we have this equation in the form $\mathcal{L}u=0$, where $\mathcal{L}$ is an operator. If v is any function, $\mathcal{L} \cdot v$. For instance, $\mathcal{L} = \frac{d}{dx}$ is the operator that define the partial derivative v_x. It is possible to write, for the linearity:

$$\mathcal{L}(u + v) = \mathcal{L} \cdot u + \mathcal{L} \cdot v \tag{4.31}$$

$$\mathcal{L}(cu) = c \cdot \mathcal{L}(u) \tag{4.32}$$

For any functions of u, v and any constant c. Whenever (4.31) holds, for all choices of u, v and c, $\mathcal{L}$ is called linear operator. The equation:

$$\mathcal{L}u = 0 \tag{4.33}$$

Is called linear if $\mathcal{L}$ is a linear operator. eq. (4.33) is called homogeneous linear equation. The equation

$$\mathcal{L}u = g \tag{4.34}$$

where $g \neq 0$ is a given function of the independent variables, is called an inhomogeneous linear equation. The advantages of linearity for the eq. (4.29) is that if u and v are both solutions, so is (u+ v). If $u_1, \ldots u_n$, are all solutions, so is any linear combination:

$$c_1 u_1(x) + \ldots + c_n u_n(x) = \sum_{i=1}^{n} c_j u_j(x) \tag{4.35}$$

where c_j is constants. PDE tipically have so many solutions, but you can have a single solution imposing auxiliary conditions. These conditions are: initial conditions and boundary conditions. An initial conditions specifies the physical state at a particular time t_0. In each physical problem there is a Domain D in which PDE is valid. For eg. the vibrating string, D is the

interval $0 < x < l$, so the boundary of D consist only of the two points $x = 0$, and $x = l$. So it is necessary to specify some boundary condition if the solution is to be determined. The three most important kinds of boundary conditions are:

- (D) u is specified ("Dirichlet condition")
- (N) the normal derivative $\frac{du}{dn}$ is specified ("Neumann condition")
- (R) $\frac{du}{dn} + au$ is specified ("Robin condition")

where a is a given function of x, y, z and t, and $\hat{n}$ is the unit normal vector perpendicular to the domain D.

4.5 COMSOL Simulations

The spatial distribution of the refractive index of the LC can be determined by the electric field associated with the voltage applied to the electrodes [53] [16]. The spatial distribution of the director's index profile is obtained by calculating the value of the minimum energy of the LC. A correct description of the orientation of the LC's director is based on the energy minimization of Oseen-Frank equation, which describes the contribution of the possible distortions and the interaction with an external electric field by considering the tensor of the dielectric anisotropy of the LC:

$$F = F_e + F_{el} \tag{4.36}$$

$$F = \frac{1}{2} \cdot \iiint \left\{ k_{11} \cdot (\nabla \cdot \vec{n})^2 + k_{22} \cdot [\vec{n} \cdot (\nabla \times \vec{n}) + \frac{2 \cdot \pi}{\varepsilon}]^2 + k_{33} \cdot [\vec{n} \times (\nabla \times \vec{n})]^2 - \varepsilon_0 \cdot [\Delta\varepsilon \cdot (\vec{n} \cdot \vec{E})^2 + \varepsilon_\perp \cdot \vec{E} \cdot \vec{E}] \right\} \tag{4.37}$$

where $\Delta\varepsilon = \varepsilon_{\parallel} - \varepsilon_{\perp} = 5.42\cdot10^{-12}\left(\dfrac{F}{m}\right)$ and:

$$\vec{D} = \varepsilon_0 \cdot \left\{ \varepsilon_{\perp} \cdot (\vec{E}\cdot\vec{n})\cdot\vec{n} + \varepsilon_{\perp} \cdot [\vec{E} - (\vec{E}\cdot\vec{n})\cdot\vec{n}] \right\} = \varepsilon_0 \cdot [\varepsilon_{\perp}\cdot\vec{E} + \Delta\varepsilon\cdot(\vec{E}\cdot\vec{n})\cdot\vec{n}]\,(4.38)$$

In eq. (4.36) we have indicated with F_e elastic energy, while F_{el} defines the electric counterpart, both are used in the calculation of the volumetric integral for the nematic LC, $\Delta\varepsilon$ represents the dielectric anisotropy and $\varepsilon_{\perp}$ is the dielectric constant perpendicular to the director at the low frequencies. The spatial distribution of the director's index profile is obtained through the calculation of the minimum value of energy of Oseen-Frank by the resolution to the partial derivatives of Euler-Lagrange. These equations are implemented in a weak form through the COMSOL Multiphysics® simulator. The boundary conditions, to have a numerical stability, were considered as the lateral conditions of the angles of tilt (θ) and of twist (φ), as shown in fig. 4.7.
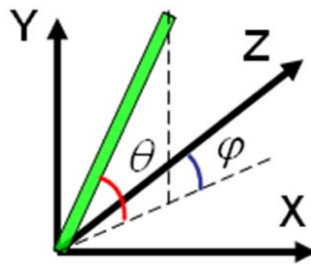
Fig. 4.7 The orientation of the LC director in function of the tilt (θ) and of twist (φ) angles.

The simulations performed in COMSOL Multiphysics® included coplanar gold electrodes placed along the channel with the LC. The model is shown

in fig. 4.8. The impulse sent into the simulations with the BeamPROP® is a Gaussian pulse, at a wavelength of 1550 nm.
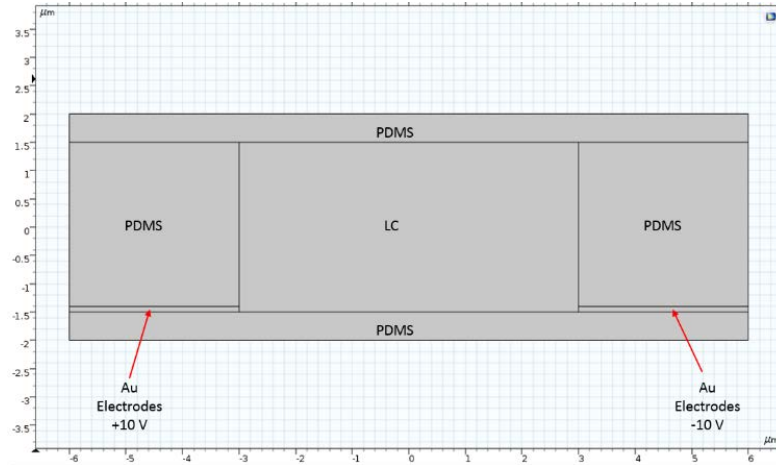
Fig. 4.8. Representation of a rectangular waveguide (6x3 µm) where the simulation of the LC E7 was performed.

In order to confine light in the waveguide it is necessary that the value of the effective index is higher than the index of refraction of the cladding but lower than that of the LC according to the following formulas:

$$n_{eff} > n_{cl} \tag{4.39}$$

$$n_{cl} < n_{eff} < n_{cr} \tag{4.40}$$

where n_{eff} is the effective index of LC, n_{cl} the refractive index of the cladding (PDMS) and n_{cr} the refractive index of the core (LC). The analysis of the fundamental mode was carried out by taking into account only the light waves propagating along the z axis direction:

$$\overline{E} = (x, y, z, t) = \overline{E}(x, y) \cdot e^{j \cdot (\omega t - \beta z)} \tag{4.41}$$

where with ω I have indicated the frequencies and with β the propagation constant. The eigenvalues associated with the electric field are derived through the Helmholtz equation:

$$\nabla \times (\nabla \times \overline{E}) - k_0^2 \cdot n^2 \cdot \overline{E} = 0 \qquad (4.42)$$

resolved by $\lambda = -j \cdot \beta$. The boundary conditions along the guide have been set with the value of zero, having assumed that the field is externally evanescent [96] [97]. It is important to note that when you study the characteristics of light in a guide, the actual mode you have is related to this simple relationship:

$$n_{eff} = \frac{\beta}{k_0} \qquad (4.43)$$

To evaluate the refractive index, I introduced in COMSOL Multiphysics® the PDE module, for each individual component, these three axes:

$$indicex = \frac{n_o n_e}{\sqrt{(n_o \cdot n_o \cdot n_1 \cdot n_1 + n_e \cdot n_e \cdot (1 - n_1 \cdot n_1)}} \qquad (4.44)$$

$$indicey = \frac{n_o n_e}{\sqrt{(n_o \cdot n_o \cdot n_2 \cdot n_2 + n_e \cdot n_e \cdot (1 - n_2 \cdot n_2)}} \qquad (4.45)$$

$$indicez = \frac{n_o n_e}{\sqrt{(n_o \cdot n_o \cdot n_3 \cdot n_3 + n_e \cdot n_e \cdot (1 - n_3 \cdot n_3)}} \qquad (4.46)$$

For the characterization of the LC, it was necessary to put the equations related to the tensor components of the dielectric constants according to the $\hat{x}, \hat{y}, \hat{z}$ axes reported according to Khoo [1]. The tensor matrix of the dielectric ε is formed by these elements:

$$epsxx = n_o \cdot n_o + (n_e \cdot n_e - n_o \cdot n_o) \cdot \cos(\theta) \cdot \cos(\theta) \cdot \sin(\phi) \cdot \sin(\phi) \tag{4.47}$$

$$epsyy = n_o \cdot n_o + (n_e \cdot n_e - n_o \cdot n_o) \cdot \sin(\theta) \cdot \sin(\theta) \tag{4.48}$$

$$epszz = n_o \cdot n_o + (n_e \cdot n_e - n_o \cdot n_o) \cdot \cos(\theta) \cdot \cos(\theta) \cdot \cos(\phi) \cdot \cos(\phi) \tag{4.49}$$

$$epsxy = epsyx = (n_e \cdot n_e - n_o \cdot n_o) \cdot \sin(\theta) \cdot \cos(\theta) \cdot \sin(\phi) \tag{4.50}$$

$$epsxz = epsyz = (n_e \cdot n_e - n_o \cdot n_o) \cdot \sin(\theta) \cdot \cos(\theta) \cdot \cos(\phi) \tag{4.51}$$

$$\begin{bmatrix} eps_{xx} & eps_{xy} & eps_{xz} \\ eps_{yx} & eps_{yy} & eps_{yz} \\ 0 & 0 & eps_{zz} \end{bmatrix} \tag{4.52}$$

with n_o= 1.5024 and n_e= 1.697 of E7 calculated at the wavelength of 1550 nm, $n_1 = \cos(\theta) \cdot \sin(\phi)$, $n_2 = \sin(\theta)$, $n_2 = \cos(\theta) \cdot \sin(\theta)$ representing the values of the director as a function of the angles of tilt and twist that describe how the LC molecules should be arranged within the waveguide.
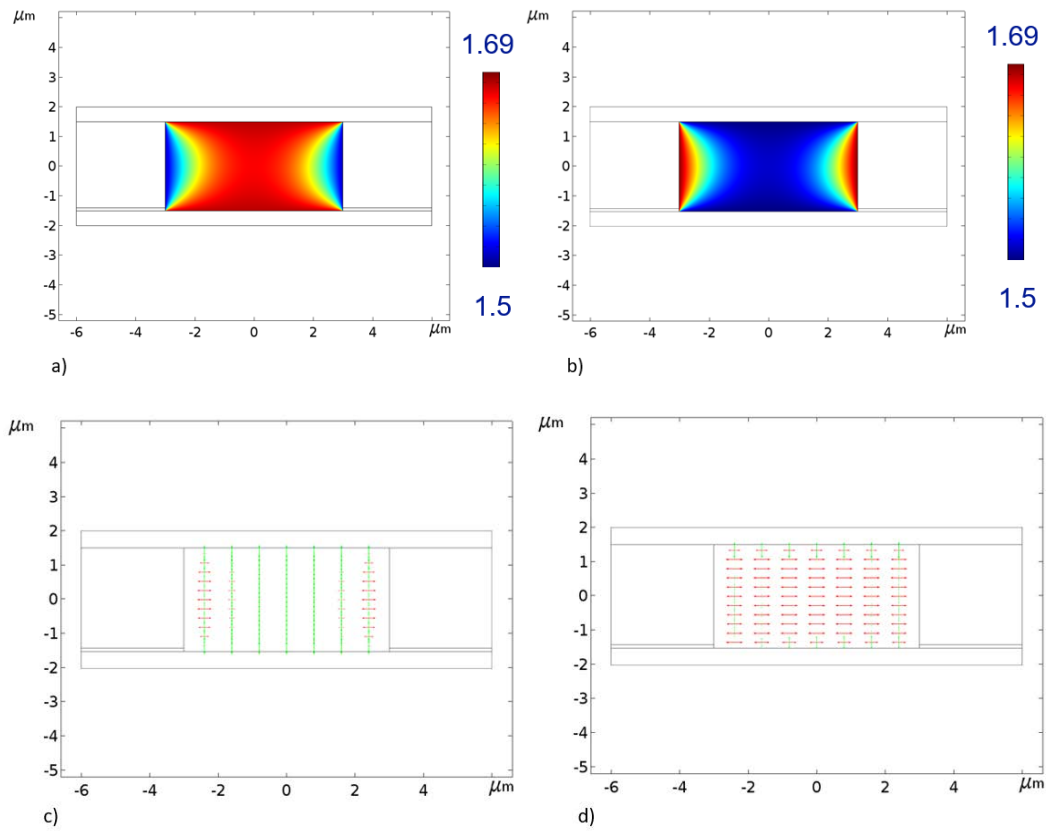
Fig. 4.9. a) Refractive index of LC E7 for a TE polarization, in a 6x3 μm channel waveguide, and b) for a TM polarization. c) Refractive index of LC E7 for a TE polarization for 0 V applied and d) for a TE polarization when it's applied +10 V on the left-hand electrode and -10 V on the right-hand electrode. In the legend is shown the range of the refractive index of the E7 @ for a wavelength of 1550 nm.

a)

b)

c)

d)

e)

f)

g)

h)

i)

l)

m)
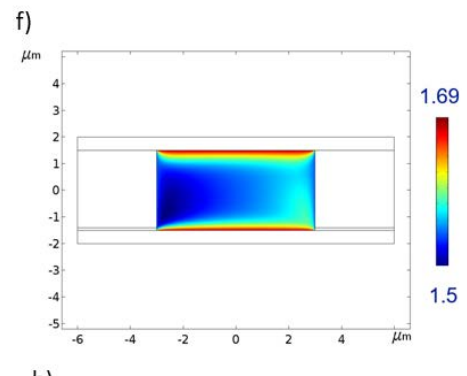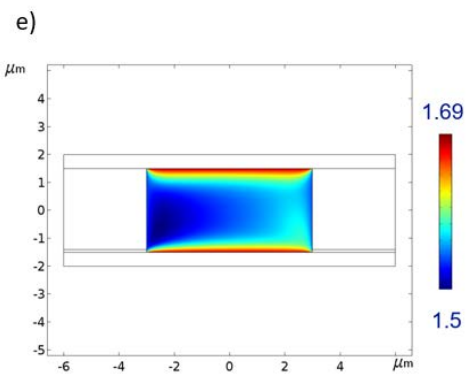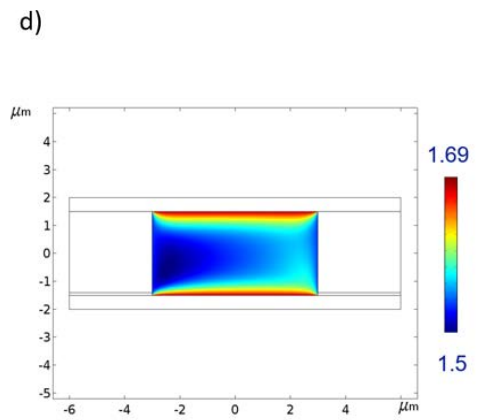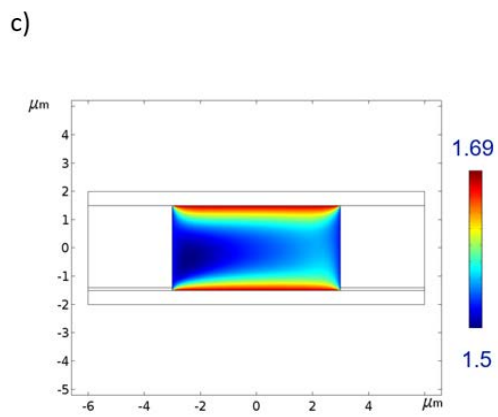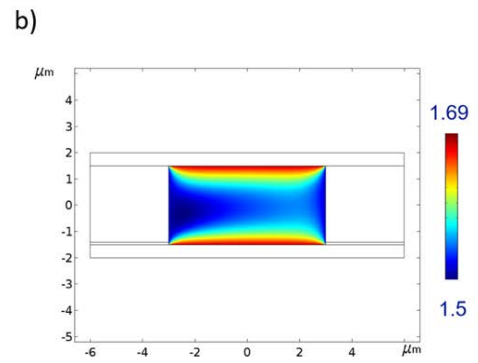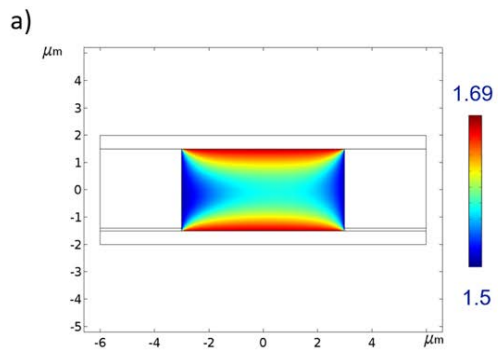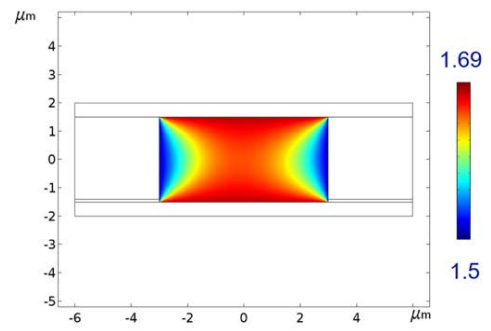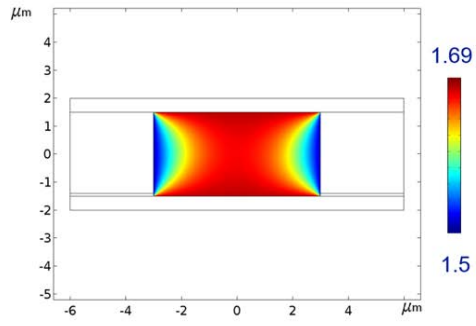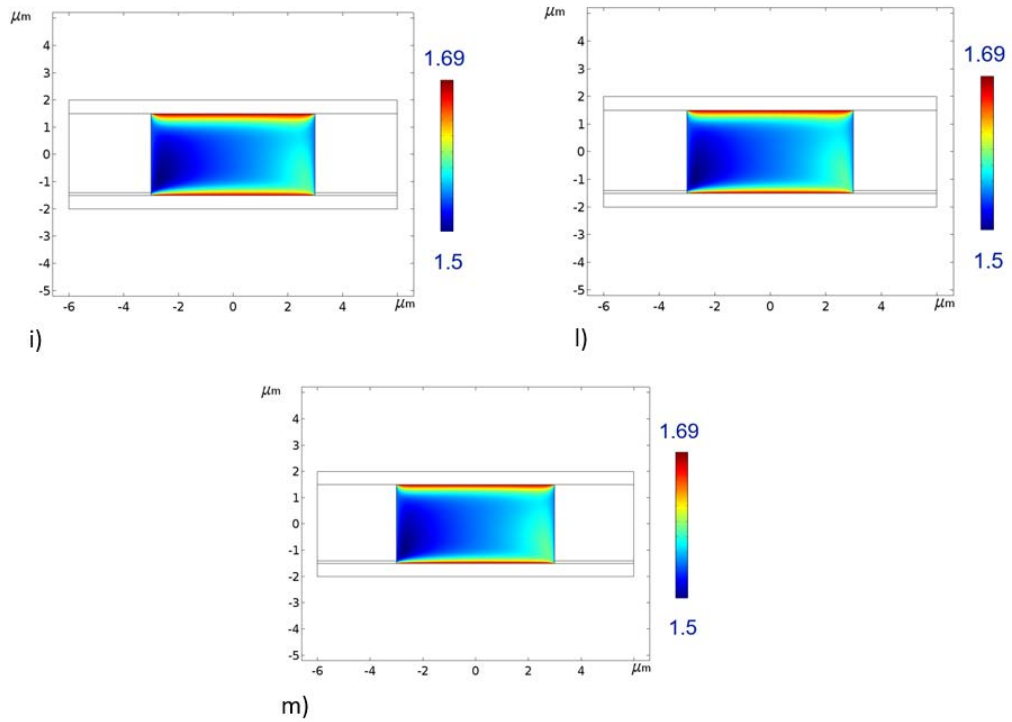
Fig. 4.10. In figure is represented the behavior of the LC molecules, for a 6x3 μm LC:PDMS channel. The applied voltage is: a) 0 V, b) 1 V, c) 2 V, d) 3 V, e) 4 V, f) 5 V, g) 6 V, h) 7 V, i) 8 V, l) 9 V, m) 10 V, respectively.
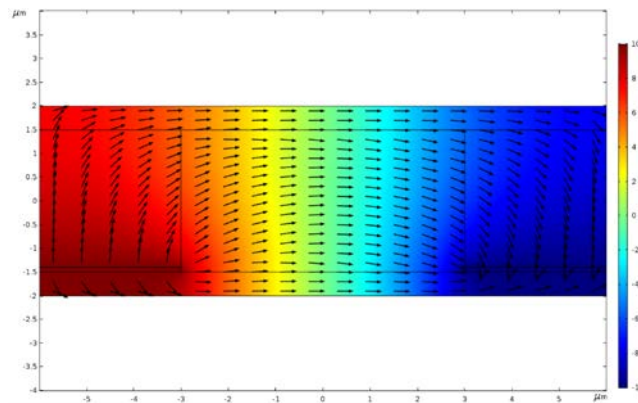
Fig. 4.11. Electric field applied to the electrodes of a 6x3 μm channel. Voltage starting from +10 V on the left-hand electrode to -10 V to the right hand electrode.

When I simulated the orientation of the LC molecules, I found the threshold voltage to tilt the LC molecules in the PDMS channel. To obtain numerical values I used some probes inside the simulation program. These probes

have been placed at different points of the canal filled with LC, as depicted in fig. 4.12. The variation of the tilt angle of the crystal liquid molecules has been studied for two different geometries of optofluidic waveguides with a cross section of 6x3 um and 3x3 um respectively. These two geometries are the basis of two distinct optofluidic devices simulated and described in detail in the fifth and sixth chapters of this thesis, namely the zero-gap directional coupler and the multi modal interferometer (MMI). The tilt angle is represented in function of the voltage applied to the electrodes, and the tilt angle is measured in radians. In both models the only variation concerns the cross section of the channel, not the thickness of the electrodes or the material with which they are made. In fig.4.12 the trend of the tilt angle is shown as a function of the voltage to be applied to the electrodes in order to have a re-orientation of the molecules of the LC. For a geometry of 3x3 um the minimum voltage to be applied tilt the LC molecules is about 2 V while for a 6x3 geometry the minimum voltage to be applied is about 4 V [99]. In both simulations the position of the test probes is the same.
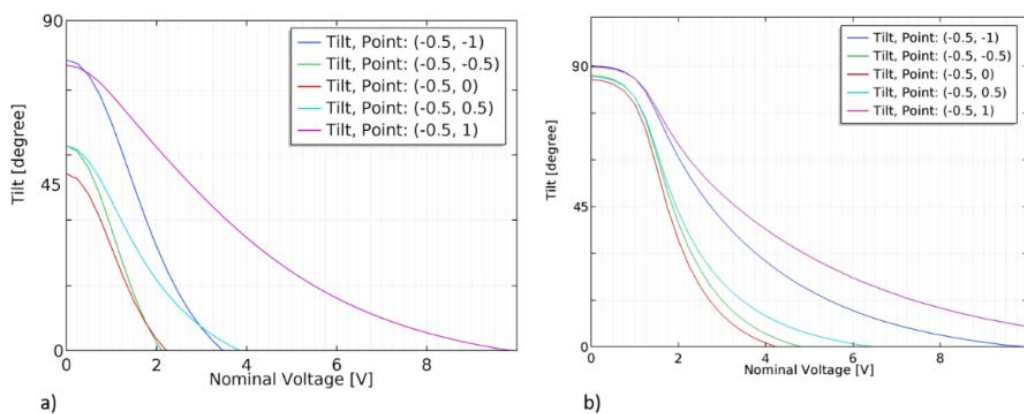
Fig. 4.12. The tilt angle expressed in radiant is plotted versus the applied voltage for several points inside a 3x3 μm (a) and 6x3 μm (b) channel. The coordinate x is fixed at -0.5 μm and y varies from -1 μm to 1 μm. The voltage to tilt the molecules by $\pi/2$ is about 2 V for a 3x3 μm geometry and 4.25 V [99] for a 6x3 cross section, y=0.

The arrangement of the E7 LC in the simulated guides with rectangular and square geometry is homotropic with respect to the walls of the PDMS, as previously mentioned.

The simulations took place following this criterion: through COMSOL Multiphysics®, rectangular and square guides have been simulated, for both almost TE and near TM modes. The refractive indices were extracted using a text file produced by COMSOL Multiphysics® and were subsequently reprocessed through Matlab® where they were imported into the BeamProp ® to study the propagation along z.
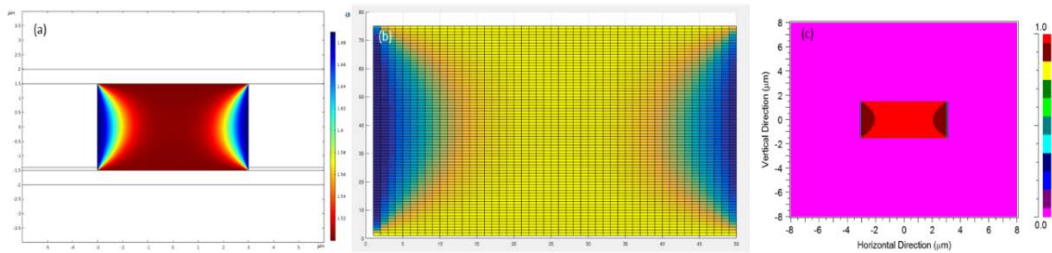
Fig. 4.13. a), b), c) The refractive index of LC E7 is shown with respect to the quasi-TM polarization a) simulated in COMSOL Multiphysics®, b) imported into Matlab® an 80 x 50 of elements matrix, c) imported into BeamProp®.

The 2D model represents the cross section of a rectangular waveguide with dimensions of 6 x 3 µm. Then, a 3-D model (6 x 10 x 3 µm) predicated on the previous 2-D one was created for the LC:PDMS technology waveguide, see fig. 4.14 a) and b). In order to implement the 3D model two further parameters were added to the original configuration: tilt angle (θ), and twist angle (φ). In addition, a supplementary condition had to be sat. Indeed, all the terms in eq. (4.51) can not be null. Therefore, the model

resulted into an enclosed structure along the three space dimensions. The homeotropic alignment conditions for the LC stood also for the 3-D case. Since the 2-D model included gold electrodes (100 nm for the thickness) also, electrical contacts (i.e. Au thin plates) were introduced even in 3-D one, as reported in the fig. 4.14 a) and b). The former corresponds to the LC state at 0 V. On the other hand, the latter describes the system when the +10 V on the left-side electrode and -10 V on the right-side electrode.
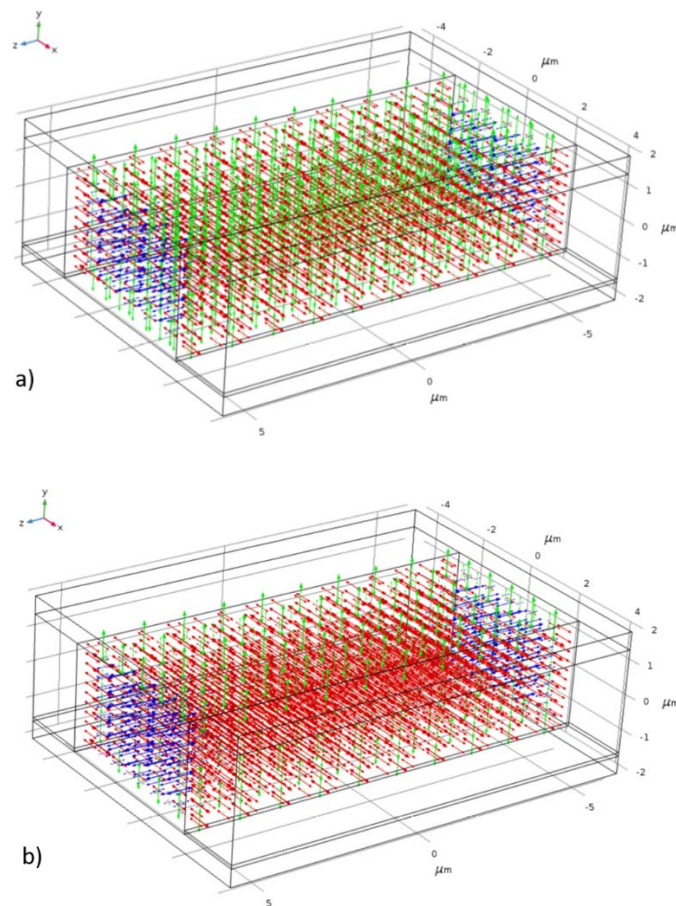
Fig. 4.14. In a) the refractive index of LC E7 for a TE polarization at 0 V applied is represented and b) when +10 V on the left-hand electrode and -10 V on the right-hand electrode is applied.
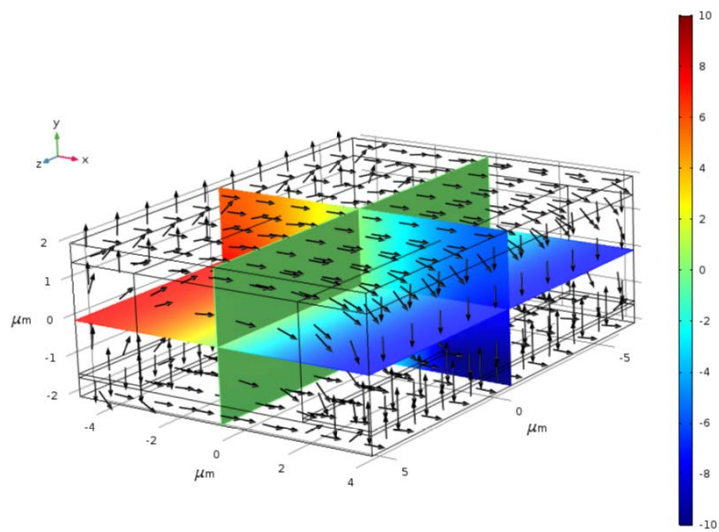
Fig. 4.15. Electric field in 3D view of the voltage starting from +10V on the left-hand electrode to -10V to the right hand electrode. The black arrows represent the electric field.

Conclusions

In COMSOL Multiphysics® the Oseen-Frank model was introduced for the description of the elastic energy of the LC to which the contribution of the electric field has been added. Thanks to this model it has been possible to simulate both guides with rectangular 6x3 μm and square 3x3 μm cross sections, supposing very small variations of the tilt and twist angles. The orientation of the LC molecules has been studied with and without the use of a potential applied to the structure that generated an electric field and finally exposed the data and imported into BeamProp® thanks to which devices such as the zero gap couplers and the multimodal interferometer will be simulated.

Chapter 5: Directional coupler

5.1 Theory of the coupling modes

Starting from the equations of Maxwell, [100-116], in complex form for an unperturbed waveguide can be rewritten as:

$$\nabla \times \overline{E}_I = -j\omega \cdot \mu \cdot \overline{H}_I \qquad (5.1)$$

$$\nabla \times \overline{H}_I = -j\omega \cdot \varepsilon \cdot \overline{E}_I \qquad (5.2)$$

The propagation modes define that complete set of orthogonal solutions by which it is possible to describe, for each field distribution given in the waveguide, as the sum between a finite set of guided modes and a spectrum of radiant modes. Considering a perturbation of the guide due to a variation of $\Delta\varepsilon$ of the permittivity and introducing the subscript, P represents the perturbation. The Maxwell equations take the form:

$$\nabla \times \overline{E}_P = -j\omega \cdot \mu \cdot \overline{H}_P \qquad (5.3)$$

$$\nabla \times \overline{H}_P = -j\omega \cdot (\varepsilon + \Delta\varepsilon) \cdot \overline{E}_P \qquad (5.4)$$

therefore rewritten as eq. (5.4):

$$\nabla \times \overline{H}_P = -j\omega \cdot \varepsilon \cdot \overline{E}_P - j\omega \cdot \Delta\varepsilon \cdot \overline{E}_P \qquad (5.5)$$

The fact that the variation $\Delta\varepsilon$ corresponds to the perturbation defined by a source term is highlighted. Rewriting the Maxwell equations through the polarization vector:

$$\nabla \times \overline{E}_p = -j\omega \cdot \mu \cdot \overline{H}_p \tag{5.6}$$

$$\nabla \times \overline{H}_p = -j\omega \cdot \varepsilon \cdot \overline{E}_p - j\omega \cdot \overline{P} \tag{5.7}$$

applying the Lorentz reciprocity theorem obtaining:

$$\nabla \cdot (\overline{E}_p \times \overline{H}_l^* + \overline{E}_l^* \times \overline{H}_p) = -j\omega \cdot (\overline{P} \cdot \overline{E}_l^*) \tag{5.8}$$

And introducing the operator ∇ transversely and integrated on a transverse surface we have that:

$$\int\limits_{-\infty}^{+\infty}\int \overline{\nabla}_t \cdot (\overline{E}_p \times \overline{H}_l^* + \overline{E}_l^* \times \overline{H}_p) dxdy + \int\limits_{-\infty}^{+\infty}\int \frac{d}{dx} \cdot (\overline{E}_p \times \overline{H}_l^* + \overline{E}_l^* \times \overline{H}_p \cdot \hat{z} dxdy = -j\omega \cdot \int\limits_{-\infty}^{+\infty}\int \overline{P} \cdot \overline{E}_l^* dxdy$$

$$\tag{5.9}$$

Applying the divergence theorem to the first integral of eq. (5.9) the equation becomes:

$$\int\limits_{-\infty}^{+\infty}\int \overline{\nabla}_t \cdot (\overline{E}_p \times \overline{H}_l^* + \overline{E}_l^* \times \overline{H}_p) dxdy = \oint_C (\overline{E}_p \times \overline{H}_l^* + \overline{E}_l^* \times \overline{H}_p) \cdot \hat{l} dl \tag{5.10}$$

A second member is introduced in the equality. The circuitry integral theorem is evaluated on a circumference C where the two-dimensional

integral is calculated by the Sommerfield condition. The sources of the fields have ended at a distance $r \to \infty$ having:

$$\lim_{r \to \infty} r \cdot \overline{E} = 0 \tag{5.11}$$

$$\lim_{r \to \infty} r \cdot \overline{H} = 0 \tag{5.12}$$

the two limits impose that the integral written previously is equal to:

$$\oint_C (\overline{E}_p \times \overline{H}_l^* + \overline{E}_l^* \times \overline{H}_p) \cdot \hat{l} dl = 0 \tag{5.13}$$

therefore the eq. (5.9) can be rewritten as:

$$\int_{-\infty}^{+\infty} \int \frac{d}{dx} \cdot (\overline{E}_p \times \overline{H}_l^* + \overline{E}_l^* \times \overline{H}_p) \cdot \hat{z} \, dxdy = -j\omega \cdot \int_{-\infty}^{+\infty} \int \overline{P} \cdot \overline{E}_l^* dxdy \tag{5.14}$$

The transverse, $\overline{E}_t, \overline{H}_t$, and longitudinal, $\overline{E}_l, \overline{H}_l$, components of the electric and magnetic fields introduced are:

$$\overline{E} = \overline{E}_t + \overline{E}_l \tag{5.15}$$

$$\overline{H} = \overline{H}_t + \overline{H}_l \tag{5.16}$$

if these terms are replaced in eq. (5.14) it can be rewritten as:

$$\frac{d}{dx} \int\limits_{-\infty}^{+\infty} \int (\overline{E}_{p,t} \times \overline{H}_{l,t}^* + \overline{E}_{l,t}^* \times \overline{H}_{p,t}) \cdot \hat{z} dxdy = -j\omega \cdot \int\limits_{-\infty}^{+\infty} \int \overline{P} \cdot \overline{E}_l^* dxdy \quad (5.17)$$

This last equation indicates a general relationship between the solutions of an unperturbed structure and the solutions that are generated by the addition of a perturbation of the system. Moreover, it is strictly connected to the orthogonality properties of the guided modes. Considering the case in which there is $\overline{P} = 0$ eq. (5.17) it will become:

$$\int\limits_{-\infty}^{+\infty} \int (\overline{E}_{p,t} \times \overline{H}_{l,t}^* + \overline{E}_{l,t}^* \times \overline{H}_{p,t}) dxdy \qquad (5.18)$$

It represents the orthogonality between the different counter-propagating modes. Writing then both the electric field and the perturbed magnetic field we obtain:

$$\overline{E}_{p,t}(x,y,z) = \sum_v \overline{E}_{t,v}(x,y) \cdot \left[A_v(z) \cdot e^{-j\beta_v z} + B_v(z) \cdot e^{-j\beta_v z} \right] + \int \overline{E}_{rad,v} dv \quad (5.19)$$

$$\overline{H}_{p,t}(x,y,z) = \sum_v \overline{H}_{t,v}(x,y) \cdot \left[A_v(z) \cdot e^{-j\beta_v z} + B_v(z) \cdot e^{-j\beta_v z} \right] + \int \overline{H}_{rad,v} dv \quad (5.20)$$

Considering only the couplings between the guided modes we will have:

$$\overline{E}_{p,t}(x,y,z) = \sum_v \left[A_v(z) \cdot e^{-j\beta_v z} + B_v(z) \cdot e^{-j\beta_v z} \right] \cdot \overline{E}_{t,v}(x,y) \quad (5.21)$$

$$\overline{H}_{p,t}(x,y,z) = \sum_v \left[A_v(z) \cdot e^{-j\beta_v z} + B_v \cdot (z) e^{-j\beta_v z} \right] \cdot \overline{H}_{t,v}(x,y) \quad (5.22)$$

The coefficients $A_\nu(z)$ refer to direct modes that propagate along the positive direction of the $\hat{z}$ and $B_\nu(z)$ represents those which are reflected. The coefficients are in function of $\hat{z}$ otherwise $\bar{E}_{pt}(x, y, z)$ and $\bar{H}_{pt}(x, y, z)$ would be solutions of an unperturbed waveguide.

5.1.1 Couplings between co-propagating modes

The electric and magnetic fields are defined as:

$$\overline{E}_l = \overline{E}_\mu \cdot e^{-j\beta_\mu z} \tag{5.23}$$

$$\overline{H}_l = \overline{H}_\mu \cdot e^{-j\beta_\mu z} \tag{5.24}$$

Through eq. (5.19) and eq. (5.20) the eq. (5.17) becomes:

$$\sum_\mu \frac{d}{dz}\left(\int_{-\infty}^{+\infty}\int \left[\begin{array}{l} (A_\nu(z)e^{-j\beta_\nu z} + B_\nu(z)e^{-j\beta_\nu z}) \cdot (\overline{E}_{t,\nu} \times \overline{H}_{t,\mu}^*)e^{-j\beta_\nu z} + \\ +(A_\nu(z)e^{-j\beta_\nu z} - B_\nu(z)e^{-j\beta_\nu z}) \cdot (\overline{H}_{t,\nu} \times \overline{E}_{t,\mu}^*)e^{-j\beta_\nu z} \end{array} \right] \cdot \hat{z} dxdy \right) =$$

$$= \sum_\mu \frac{d}{dz}\left(\begin{array}{l} e^{-j\beta_\nu z}\left[(A_\nu(z)e^{-j\beta_\nu z} \int_{-\infty}^{+\infty}\int (\overline{E}_{t,\nu} \times \overline{H}_{t,\mu}^* + \overline{H}_{t,\nu} \times \overline{E}_{t,\mu}^*) \cdot \hat{z} dxdy \right] + \\ +e^{-j\beta_\nu z}\left[(B_\nu(z)e^{-j\beta_\nu z} \int_{-\infty}^{+\infty}\int (\overline{E}_{t,\nu} \times \overline{H}_{t,\mu}^* - \overline{H}_{t,\nu} \times \overline{E}_{t,\mu}^*) \cdot \hat{z} dxdy \right] \end{array} \right)$$

$$\tag{5.25}$$

Thanks to the property of orthogonality between the modes, the integrals with $\mu \neq \nu$ are null and therefore:

$$\int_{-\infty}^{+\infty}\int \frac{\overline{E}_\mu \times \overline{H}_\mu^*}{2} \cdot \hat{z} dxdy = \int_{-\infty}^{+\infty}\int \frac{\overline{H}_\mu \times \overline{E}_\mu^*}{2} \cdot \hat{z} dxdy = 1 \qquad (5.26)$$

The term A_μ that is associated with positive propagation will be:

$$\frac{dA_\mu}{dx} = -j\frac{\omega}{4} \cdot e^{j\beta_\mu z} \cdot \iint \overline{P} \cdot \overline{E}_\mu^* dxdy \qquad (5.27)$$

5.1.2 Coupling between counter-propagating modes

When it is necessary to describe the $\mu-last$ counter-propagating mode it is necessary to define the electric and magnetic fields as follows [100]:

$$\overline{E}_l = \left(\overline{E}_{t,\mu} - \overline{E}_{z,\mu}\hat{z}\right) \cdot e^{-j\beta_\mu z} \qquad (5.28)$$

$$\overline{H}_l = \left(\overline{-H}_{t,\mu} + \overline{H}_{z,\mu}\hat{z}\right) \cdot e^{-j\beta_\mu z} \qquad (5.29)$$

For the co-propagating structure we have:

$$\frac{dB_\mu}{dx} = -j\frac{\omega}{4} \cdot e^{j\beta_\mu z} \cdot \iint \overline{P} \cdot \overline{E}_\mu^* dxdy \qquad (5.30)$$

the two solutions eq. (5.27) and eq. (5.30) represent the fact that the perturbation is described in the most general way possible through the polarization vector $\overline{P}$. The perturbation can always be seen as a variation

of the dielectric allowance from the nominal value of $\varepsilon(x, y)$ and then rewriting the polarization vector as:

$$\overline{P} = \Delta\varepsilon(x, y, z) \cdot \overline{E}_p \qquad (5.31)$$

the variation in permittivity leads to a change in the refractive index n(x, y, z) being:

$$n^2(x, y, z) = \frac{\varepsilon(x, y) + \Delta\varepsilon(x, y, z)}{\varepsilon_0} \qquad (5.32)$$

The anisotropies are represented by the tensors relative to the electric and magnetic fields. Considering the simplest case in which there is a perturbation along the $\hat{z}$ axis of the waveguide we can assume for simplicity $\Delta\varepsilon = \Delta\varepsilon(z)$ and the polarization vector disappears:

$$\overline{P} = \overline{P}_t + \overline{P}_z \cdot \hat{z} \qquad (5.33)$$

And

$$\overline{P}_t = \Delta\varepsilon \cdot \overline{E}_{p,t} = \Delta\varepsilon \cdot \sum_v (A_v(z) \cdot e^{-j\beta_v z} + B_v(z) \cdot e^{-j\beta_v z}) \cdot \overline{E}_{t,v} \qquad (5.34)$$

substituting in Maxwell's equations:

$$j\omega \cdot (\varepsilon + \Delta\varepsilon) \cdot \overline{P}_{p,z} = \nabla_t \times \overline{H}_{p,t} \qquad (5.38)$$

$$\overline{E}_z \cdot \hat{z} = \overline{\nabla}_t \times \overline{H}_t \qquad (5.36)$$

we have that:

$$\overline{P}_t = \Delta\varepsilon \cdot \overline{E}_{p,z} \cdot \hat{z} = \frac{\Delta\varepsilon}{\varepsilon+\Delta\varepsilon} \cdot \frac{1}{j\omega} \cdot \overline{\nabla}_t \times \overline{H}_{p,t} = \frac{\Delta\varepsilon}{\varepsilon+\Delta\varepsilon} \cdot \frac{1}{j\omega} \cdot \sum_v (A_v(z) \cdot e^{-j\beta_v z} + B_v(z) \cdot e^{-j\beta_v z}) \cdot \overline{\nabla}_t \times \overline{H}_{v,t} =$$

$$= \frac{\varepsilon \cdot \Delta\varepsilon}{\varepsilon+\Delta\varepsilon} \cdot \sum_v (A_v(z) \cdot e^{-j\beta_v z} + B_v(z) \cdot e^{-j\beta_v z}) \cdot \overline{E}_{v,z} \cdot \hat{z}$$

$$(5.37)$$

rewriting the last equation as:

$$-j \cdot \frac{\omega}{4} \cdot e^{-j\beta_\mu z} \iint \left[\Delta\varepsilon \cdot \left(A_v(z) \cdot e^{-j\beta_v z} + B_v(z) \cdot e^{-j\beta_v z} \right) \cdot \overline{E}_{v,t} \cdot \overline{E}^*_{\mu,t} + \frac{\Delta\varepsilon}{\varepsilon+\Delta\varepsilon} \cdot \right.$$

$$\left. \left(A_v(z) \cdot e^{-j\beta_v z} - B_v(z) \cdot e^{-j\beta_v z} \right) \cdot \overline{E}_{v,t} \cdot \overline{E}^*_{\mu,t} \right] \cdot dxdy \qquad (5.38)$$

and

$$-j \cdot \frac{\omega}{4} \cdot e^{-j\beta_\mu z} \iint \left[\Delta\varepsilon \cdot \left(A_v(z) \cdot e^{-j\beta_v z} - B_v(z) \cdot e^{-j\beta_v z} \right) \cdot \overline{E}_{v,t} \cdot \overline{E}^*_{\mu,t} + \frac{\Delta\varepsilon}{\varepsilon+\Delta\varepsilon} \cdot \right.$$

$$\left. \left(A_v(z) \cdot e^{-j\beta_v z} - B_v(z) \cdot e^{-j\beta_v z} \right) \cdot \overline{E}_{v,t} \cdot \overline{E}^*_{\mu,t} \right] \cdot dxdy \qquad (5.39)$$

from which we can derive the equation of coupled modes:

$$\frac{dA_\mu}{dx} = -j \cdot \sum_v (K^+_{\mu,v} \cdot A_v \cdot e^{-j(\beta_v - \beta_\mu)\hat{z}} + K^-_{\mu,v} \cdot B_v \cdot e^{-j(\beta_v - \beta_\mu)\hat{z}}) \qquad (5.40)$$

$$\frac{dB_\mu}{dx} = -j \cdot \sum_v (K^-_{\mu,v} \cdot A_v \cdot e^{-j(\beta_v - \beta_\mu)\hat{z}} + K^+_{\mu,v} \cdot B_v \cdot e^{-j(\beta_v - \beta_\mu)\hat{z}}) \qquad (5.41)$$

the co-propagating and counter-propagating coupling coefficients $K^+_{\mu,v}$

and $K_{\mu,\nu}^-$ have been indicated, while with $K_{\mu,\nu}^t$ and $K_{\mu,\nu}^z$ are the coefficients of transversal and longitudinal coupling:

$$K_{\mu,\nu}^+ = K_{\mu,\nu}^t + K_{\mu,\nu}^z \tag{5.42}$$

$$K_{\mu,\nu}^- = K_{\mu,\nu}^t - K_{\mu,\nu}^z \tag{5.43}$$

$$K_{\mu,\nu}^t = \frac{\omega}{4} \cdot \int\limits_{-\infty}^{+\infty}\int \Delta\varepsilon \cdot \overline{E}_{t,\nu} \cdot \overline{E}_{t,\mu}^* dxdy \tag{5.44}$$

$$K_{\mu,\nu}^z = \frac{\omega}{4} \cdot \int\limits_{-\infty}^{+\infty}\int \frac{\varepsilon\Delta\varepsilon}{\varepsilon + \Delta\varepsilon} \cdot \overline{E}_{z,\nu} \cdot \overline{E}_{z,\mu}^* dxdy \tag{5.45}$$

Assuming that the two guides are monomodal, they allow the propagations of a single mode, and can consider null the longitudinal component of the electric fields. Imposing that the counter-propagating modes are $K_{\mu,\nu}^z = 0$. Under these conditions can be rewritten as:

$$\frac{dA_a}{dz} = -j \cdot K_{a,a}^t \cdot A_a - j \cdot K_{b,a}^t \cdot A_{a,b} \cdot e^{-j(\beta_b - \beta_a)\hat{z}} \tag{5.46}$$

$$\frac{dA_b}{dz} = -j \cdot K_{b,b}^t \cdot A_b - j \cdot K_{a,b}^t \cdot A_{b,a} \cdot e^{-j(\beta_a - \beta_b)\hat{z}} \tag{5.47}$$

The subscripts a and b are the equivalents of ν and μ, the perturbation causes a variation of the phase constants that are represented by $K_{a,a}^t$ and $K_{b,b}^t$ while the coupling is defined by the two coefficients $K_{b,a}^t$ and $K_{a,b}^t$. If we do not have the coupling terms, we would have an equation like:

$$\frac{dA_\mu}{dz} = -j \cdot K^t_{\mu,\mu} \cdot A_\mu \tag{5.48}$$

where μ= a, b describes the only way μ−last propagates in my guide along the $\hat{z}$ axis. The perturbation can be determined by considering the guide b which changes the cladding of the guide to a defined quantity such as $(\varepsilon_b - \varepsilon_{cl})$.

$$K^t_{a,a} = \frac{\omega}{4} \cdot \int\int_{-\infty}^{+\infty} (\varepsilon_b - \varepsilon_{cl}) \cdot \overline{E}_{t,a} \cdot \overline{E}^*_{t,a} dxdy \tag{5.49}$$

$$K^t_{b,a} = \frac{\omega}{4} \cdot \int\int_{-\infty}^{+\infty} (\varepsilon_b - \varepsilon_{cl}) \cdot \overline{E}_{t,b} \cdot \overline{E}^*_{t,a} dxdy \tag{5.50}$$

From eq. (5.49) and eq. (5.50) it can be noted that $K^t_{a,a}$ is negligible compared to $K^t_{b,a}$ because in the first case we have that the integrand function in the perturbed region is given by the product of the tails of the guide field which is the unperturbed one. In the second function, there is solution of the perturbing waveguide, as we can see from the subscripts. It is therefore understandable that only the terms with mixed subscripts should be considered, as they are the ones who give me information about my disrupted structure and neglect the other two. To determine $K^t_{a,b}$ we have to write:

$$K^t_{b,a} = \frac{\omega}{4} \cdot \int\int_{-\infty}^{+\infty} (\varepsilon_a - \varepsilon_{cl}) \cdot \overline{E}_{t,a} \cdot \overline{E}^*_{t,b} dxdy \tag{5.51}$$

The equations governing the directional coupler will then become:

$$\frac{dA_a}{dz} = -j \cdot K_{b,a}^t \cdot A_b \cdot e^{-j(\beta_b - \beta_a)\hat{z}} \tag{5.52}$$

$$\frac{dA_b}{dz} = -j \cdot K_{a,b}^t \cdot A_a \cdot e^{-j(\beta_a - \beta_b)\hat{z}} \tag{IV.80}$$

The relation that binds $K_{b,a}^t$ with $K_{a,b}^t$ drift from the condition of power conservation. If it is necessary to define the power linked to the $\mu-$like mode, the power term can be written as:

$$P_\mu = A_\mu \cdot A_\mu^* \tag{5.53}$$

The equations describing the operation of the directional coupler define only two modes and therefore the perturbation power will be given by:

$$P_t = P_a \cdot P_b = A_a \cdot A_a^* + A_b \cdot A_b^* \tag{5.54}$$

energy conservation requires that:

$$\frac{dP_t}{dz} = 0 \tag{5.55}$$

from which:

$$\frac{dA_a}{dz} \cdot A_a^* + \frac{dA_a^*}{dz} \cdot A_a + \frac{dA_b}{dz} \cdot A_b^* + \frac{dA_b^*}{dz} \cdot A_b = 0 \tag{5.56}$$

substitution will show that:

$$jA_aA_b^* \cdot (K_{b,a}^* - K_{a,b}) \cdot e^{j\partial z} + jA_bA_a^* \cdot (K_{a,b}^* - K_{b,a}) \cdot e^{-j\partial z} = 0 \qquad (5.57)$$

placing $\delta = \beta_a - \beta_b$ since we have an equality it must necessarily be verified and therefore:

$$K_{a,b} = K_{b,a}^* = k \qquad (5.58)$$

The equations of the couplers become:

$$\frac{dA_a}{dz} = -jkA_b \cdot e^{-j\partial z} \qquad (5.59)$$

$$\frac{dA_b}{dz} = -jkA_a \cdot e^{j\partial z} \qquad (5.60)$$

By deriving eq. (5.59) and always replacing it, we obtain a second order equation:

$$\frac{d^2A}{dz^2} + j \cdot \partial \left(\frac{dA_a}{dz} \right) + |k|^2 \cdot A_a = 0 \qquad (5.61)$$
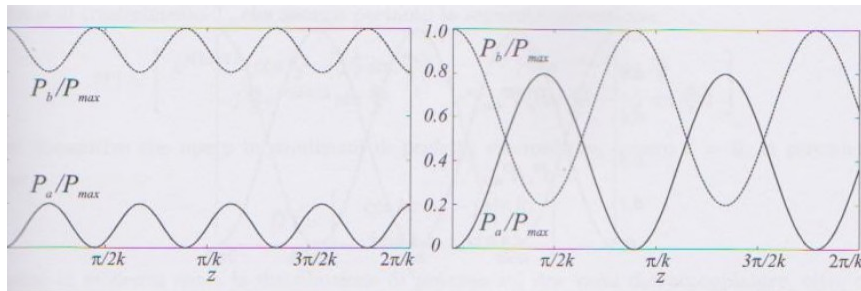
Fig. 5.1. Trend of the normalized powers of the modes a and b to the increase of the synchronism, that is to the decreasing values d, with the same coefficient of coupling [100].

Shown in fig. 5.1 is the trend of the normalized powers of the modes a, b according to the values that it can assume δ with the value of 4K and k. By imposing the boundary conditions in $\hat{z} = 0$ and the presence of the only modes in the second guide we have that $A_a = 0$, $A_b = 0$ obtaining the following solutions:

$$A_a(z) = -j \cdot A_0 \cdot \frac{2k}{S} \cdot e^{-\frac{j\delta z}{2}} \cdot \sin(\frac{Sz}{2}) \tag{5.62}$$

$$A_b(z) = -j \cdot A_0 \cdot e^{-\frac{j\delta z}{2}} \cdot \left[\cos(\frac{Sz}{2}) - \frac{j\delta}{2} \cdot \sin(\frac{Sz}{2}) \right] \tag{5.63}$$

having defined S:

$$S = 2 \cdot \sqrt{|k|^2 + \left|\frac{\delta}{2}\right|^2} \tag{5.64}$$

the total power can be written as:

$$P_t = P_a \cdot P_b = A_a \cdot A_a^* + A_b \cdot A_b^* = |A|^2 \tag{5.65}$$

for the individual powers associated with the guides we can write:

$$P_a = |A_0|^2 \cdot \frac{4 \cdot |k|^2}{S^2} \cdot \sin^2(\frac{Sz}{2}) \tag{5.66}$$

$$P_b = (P_t - P_a) \cdot |A_0|^2 \cdot (1 - \frac{4|k|^2}{S^2} \cdot \sin^2(\frac{Sz}{2})) \tag{5.67}$$

P_a and P_b have a period of $\Delta z = \frac{2\pi}{S}$ and in particular the maximum value is given by:

$$P_{\text{max}} = \left|A_0\right|^2 \cdot \frac{4 \cdot \left|k\right|^2}{S^2} \tag{5.68}$$

The mode A_b transfers part of its power to the mode A_a until the maximum value is reached, and this value is directly proportional to the coupling coefficient and the difference between the phase constants δ, in which the mode-related $\delta_a \neq 0$ and $\delta_b \neq 0$ define the trend displayed in fig. 5.3. If it can have the perfect synchronism between the two waves or when it can achieve the condition $\delta = 0$ and it has the maximum transfer of power between the two sides, then:

$$P_{\text{max}} = \left|A_0\right|^2 \tag{5.69}$$

The maximum power transferred is related to the wavelength λ through the relationship $L_c = \frac{\pi}{2|k|}$ and the previously defined mode functions $E_{t,a}$ and $E_{t,b}$. We can notice that the coupling length is inversely proportional to the coefficient k.

5.2 Design of an LC:PDMS based directional coupler

An LC:PDMS directional coupler is made of two identical waveguides as shown in fig. 5.4. LC molecules are already homeotropically aligned to the PDMS surface, without any alignment layer as usually required in standard LC electro-optic devices.
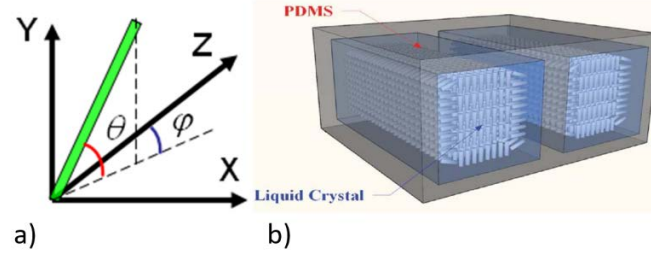
Fig. 5.2. a) Orientation of the director of the LC. b) Schematic 3D view of a LC:PDMS passive directional coupler [8].

As previously mentioned, LC molecules in a nematic phase were aligned along a common direction defined by a unit vector $\hat{n}$, see fig. 5.2 a), that established a privileged average molecular orientation, rendering the nematic LC (NLC) macroscopically anisotropic and uniaxial. The free energy was minimized in order to obtain the molecular director orientation $\hat{n}$ of the NLC inside the PDMS channels. The unit vector $\hat{n}$ represented the normalized director of the molecules. In the present model $\hat{n}$ it was identified by a function of tilted and twisted angles with respect to a reference system in which the z-axis is chosen parallel to the director. The orientation of the individual molecules was defined through the polar angle θ (tilt) of $\hat{n}$ with respect to the z-axis. The azimuthal angle ϕ (twist), is the one that $\hat{n}$ forms with the x-axis. The refractive index is imported from COMSOL Multiphysic® 3.5a, in fig. 5.3, and was implemented in BeamPROP® [8]. The simulated squared cross- sections of the waveguide had the dimensions of 5, 3 and 2 μm. Before calculating the propagation of the Gaussian beam in the directional couplers, the number of modes associated to each waveguide had been investigated. Since a directional coupler relying on a single mode was required the 2 μm geometry was chosen. The distribution of the refractive index was then implemented in BeamPROP® to observe the directional coupler performance at a

wavelength of 1550 nm. BeamPROP® was fed with a PDMS refractive index of 1.3997, whereas the LC refractive index was imported from COMSOL Multiphysic® for LC. A set of simulations of directional couplers was performed at different waveguide gaps starting from 0.3 μm until 1 μm. Moreover, we calculated the Extinction Ratio (ER), defined as the ratio between the output power values of the two waveguides of the coupler.
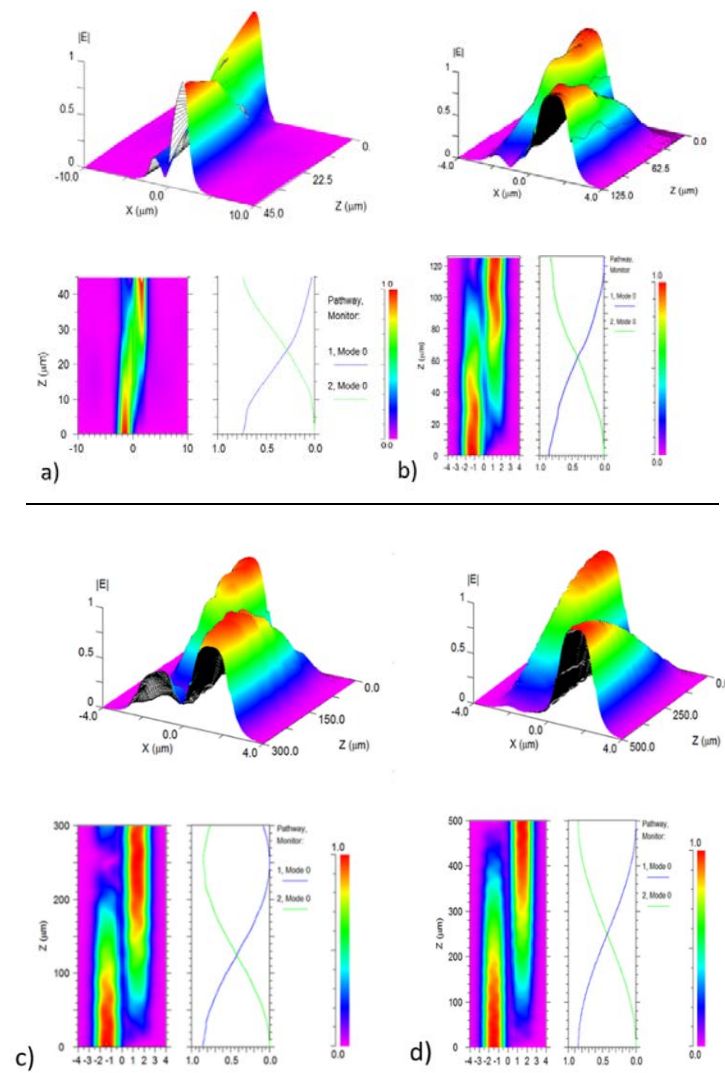
Fig. 5.3. a) Directional coupler with a gap = 0.3 μm and a coupling length of 45 μm, b) directional coupler with a gap = 0.5 μm which guarantees a coupling length of 125 μm. c) Directional coupler with a gap = 0.75 μm for a coupling length of 300 μm, d) a directional coupler with a gap of 1 μm to obtain a coupling length of 500 μm [8].

The simulations show that a complete exchange of optical power occurs at just 45 μm with an ER, defined as the ratio between the power levels at the output of the waveguides, of about 11 dB. A value of ER over 20 dB can be obtained with a coupling length of 500 μm for a gap of 1 μm [8]. The calculus of the power inside the waveguides was performed by Matlab® scripts.
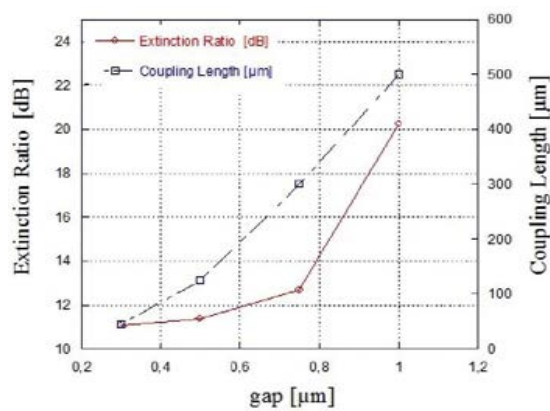
Fig. 5.4. On the left-side hand is showed the extinction ratio and coupling length versus coupler gap [8].

In order to have electro-optical control, I proposed the fabrication of flexible electrodes by sputtering ITO deposition on PDMS, as explained in the third chapter of this thesis, and as illustrated in fig. 5.5 a). The same behavior can be replicated using gold electrodes fabricated through the electroplating process as demonstrated in chapter three. It's clearly that if an electric field is applied to these electrodes, it generates a reorientation of the LC molecules to force it to have a bar state in place of the cross-state behavior of the directional coupler as shown in fig. 5.9 b). For the geometry of the electrode, the rectangular shape is the best choice, because of the electrodes must be parallel to the channels. The simulations regarding the

geometry of the electrodes does not involve variations in the shape of the electric field, as demonstrated in chapter four. Actually, a model of the directional coupler with gold electrodes is under investigation in COMSOL Multiphysic®.
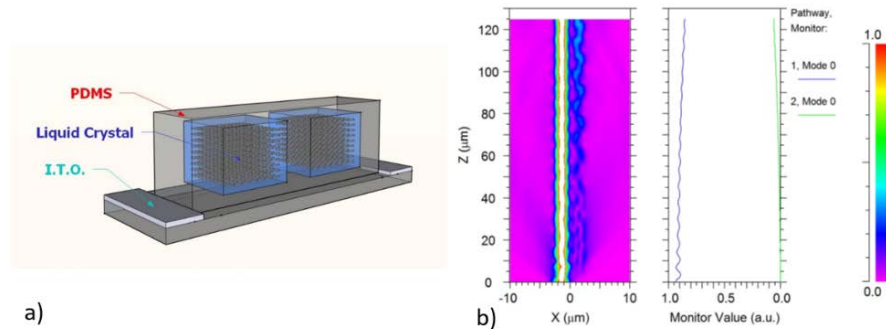
Fig 5.5. a) The figure above shows a directional coupler with electrodes in ITO with an applied voltage. b) The molecules of the LC are reoriented allowing for bar-state of the coupler as shown in the contour map produced by the BeamPROP® simulation [8].

5.3 Simulations of Zero Gap Directional Coupler

As previously seen, the simulated directional couplers had different coupling lengths and different gaps between the waveguides. An ER of 20 dB was obtained only if the gap between the waveguides was of 0.3 μm. It is quite critical to obtain such sub-micrometric gap. For this reason I investigated another optical device, the zero-gap directional coupler which is more feasible in LC:PDMS technology. The zero-gap directional coupler or bimodal coupler [117-130] is a device designed for spatial switching similar to the directional coupler except that there is no gap between the parallel coupled waveguides. The light beam comes from one

of the two input waveguides and propagates along the entire section of the coupler, as depicted in fig. 5.8.
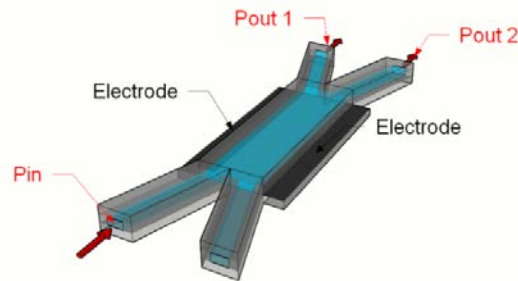
Fig. 5.6. Schematic view of zero-gap directional coupler.

The simulations of the zero-gap directional coupler are related only the central part. This section had the dimension of 3 μm with a length of 1 mm to achieve the bimodality of the waveguide. In the BeamPROP® [3] the power peak at the output can be moved to the left margin and mainly trigger the output 1, or it can be moved to the right margin and mainly trigger the output 2, as shown in fig. 5.8. It should be possible to control from which waveguide to let out the optical beam with the use of co-planar electrodes. In order to excite the two modes inside the zero gap directional coupler, a Gaussian impulse had to be launched at the extremes of the input waveguide, as depicted in fig. 5.7.
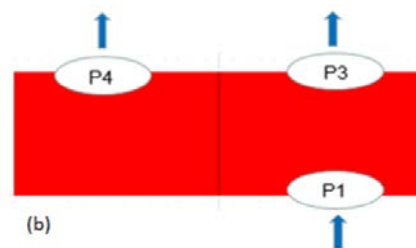
Fig. 5.7. In picture the zero-gap directional coupler simulated with unbalanced input is represented.

The output power value was obtained by considering the slices with which the zero-gap directional coupler was divided. The blue lines in fig. 5.10 are the slices through which I calculated the integral using the Simpson model to obtain the power values of the Gaussian impulse launched at the input. The distance between each line was 10 μm.
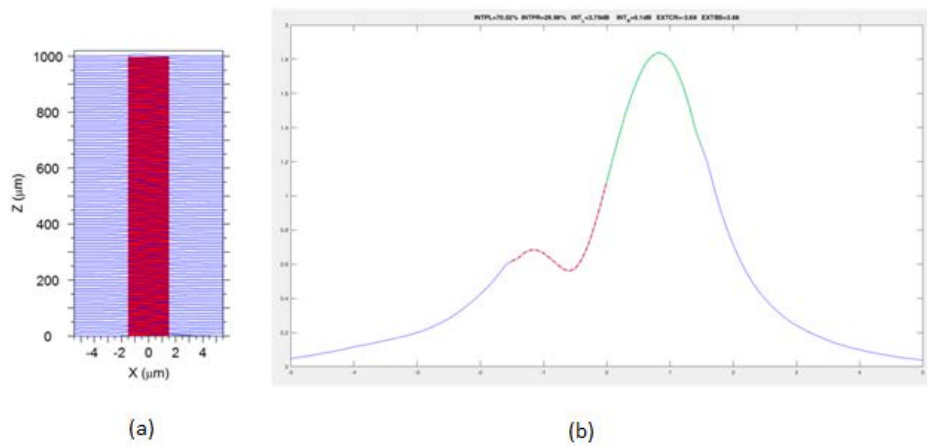
Fig. 5.8. In picture the method for the calculation of the Extinction Ratio is shown. a) The bimodal waveguides subdivided by slices, b) the representation of the calculus of the output powers of the left (P4) in red and right side (P3) in green of the bimodal guide.

The maximum value of the output power was achieved for a length of the zero gap directional coupler of 500 μm. Two extinction reports were obtained. In the case in which the ratio of the power of the right-hand drive to the left-hand one is obtained, we get a value of 16 dB of the refractive index of 1.6 LC, corresponding to apply at the devices a voltage of 1.62 V [3]. On the other hand, if I calculate the extinction ratio in relation to the ratio between the power of the left-hand drive and the right-hand drive, a value of about -18 dB is obtained for a refractive index of LC of 1.628. These results are better than those obtained by Asquini et al in ref [119]. Their values of ER were equal to -9.45 and -10.09 for two squared waveguides with dimensions of 4 μm and 3 μm respectively. This result

was linked to the different materials used in their simulations, such as the combination of BK7 glass with E7.
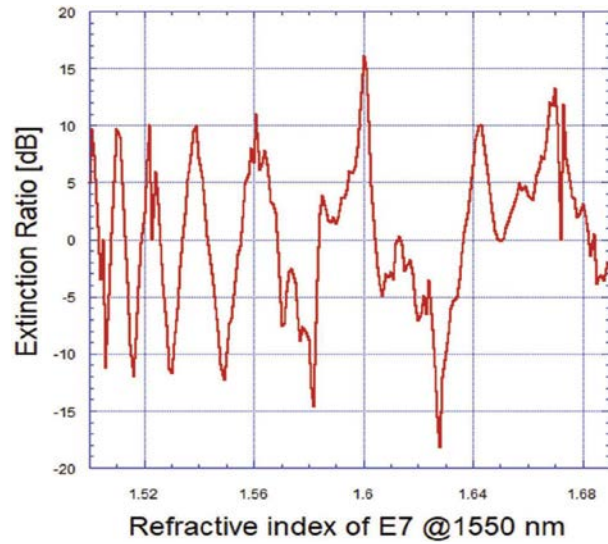
Fig. 5.9. Extinction ratio of the output of a zero-gap directional coupler switch versus LC refractive index [3].

Conclusion

Many devices have been studied in recent years through the most varied combinations of shapes and materials. Through the combined use of different materials such as GaAs, GaAlAs, InP, $LiNbO_3$ and SiO_x, directional couplers have been created with an ER starting from 20 dB up to 30 dB [111], [123-130]. But all have a common feature, they are not made of flexible materials. The combined use of PDMS and LC could be a solution to obtain flexible optoelectronic devices. I obtained two values for the ER of the zero gap directional coupler 16 dB for a refractive index of 1.6 and a value of -18 dB for a refractive index of 1.628, with a coupling length of about 500 μm while not using materials based on silicon photonics. The zero-gap coupler was studied using the combination of E7 and PDMS. In order to achieve the same results in terms of ER a 1.62 V and 1.76 V need to be applied for a refractive index of 1.6 and 1.628, respectively [3]. The results obtained through simulations suggested that it is possible to exploit the characteristics of LC:PDMS technology in a zero gap directional coupler for achieving ER values comparable to the standard materials used in optoelectronics.

Chapter 6: Multimode Interferometer

A multimodal interferometer is essentially made up of a guide whose core is able to support a large number of guided modes. Interference between the various modes within the region produces field distributions that change progressively during propagation and they are repeated periodically. This phenomenon is called the "principle of self-image". By appropriately dimensioning the lengths of the multimode region and placing the exit waveguides at suitable positions, it is possible to check the characteristics of the field in the waveguide Generally, it is always possible to realize MMI with NxM [131-134] guides in which N represents the incoming guides and M, the outgoing ones.

6.1 Theory

6.1.1 Self-Image Principle

Self-image [135-142] is a property of multimode guides whereby the incoming field profile reproduces in single or multiple copies at regular intervals along the direction of propagation of the waveguide. Mathematical treatment is usually based on the analysis of planar structures and is equivalent to both the TE and TM modes. As already mentioned, the operation is based on the displacement that occurs between the different modes during propagation. The first step is to calculate the analytical expression of phase constants. Since there is a large number of guided modes and it is necessary to apply the paraxial approximation, we have the following expression for the phase constant of the mode:

$$\beta_v \simeq \frac{2 \cdot \pi}{\lambda} \cdot n_{co} - (v+1)^2 \frac{\pi \cdot \lambda}{4 \cdot n_{co} \cdot W^2} \tag{6.1}$$

with $v = 0,1,2,\dots N-1$. According to eq. (6.1) we have:

$$\beta_0 - \beta_v \simeq \frac{v \cdot (v+2) \cdot \pi}{3 \cdot L_\pi} \tag{6.2}$$

where L_π indicates the length of beat of the fundamental mode with the first mode of higher order:

$$L_\pi = \frac{\pi}{\beta_0 - \beta_1} \simeq \frac{4 \cdot n_{co} \cdot W^2}{3 \cdot \lambda} \tag{6.3}$$

Neglecting the irradiating modes, an entirely legitimate hypothesis given the high number of guided modes and the field at the entrance to the waveguide, the field $\bar{e}_{ing} = \bar{e}_{ing}(x) \cdot \hat{\jmath}$ and his profile $\bar{e}_{ing}(x)$ can be decomposed into Nsections of all the guided modes:

$$e_{ing}(x) = \sum_{v=0}^{N-1} A_v \cdot \overline{E_v}(x) \tag{6.4}$$

with:

$$A_v = \frac{\int\limits_{-\infty}^{\infty} e_{ing}(x) \cdot \overline{E_v}(x) dx}{\int\limits_{-\infty}^{\infty} \overline{E_v}^2(x) dx} . \tag{6.5}$$

Due to the propagation of N modes, the field at a distance $z = L$ from the input section, it is valid that:

$$e(x, L) = \left(\sum_{v=0}^{N-1} A_v \cdot \overline{E_v}(x) \cdot e^{-j \cdot \beta_v \cdot L} \right) \tag{6.6}$$

Gathering the phase term of the fundamental mode as a common factor and exploiting eq. (6.2) we have:

$$e(x, L) = \left(\sum_{v=0}^{N-1} A_v \cdot \overline{E_v}(x) \cdot e^{-j(\beta_v - \beta_0) \cdot L} \right) \cdot e^{-j \cdot \beta_0 \cdot L} = \left(\sum_{v=0}^{N-1} A_v \cdot \overline{E_v}(x) \cdot e^{-j \frac{v \cdot (v+2) \cdot \pi}{3 \cdot L_\pi} \cdot L} \right) \cdot e^{-j \cdot \beta_0 \cdot L}$$

$$\tag{6.7}$$

The profile of the total field is therefore determined by the input field through the coefficients and the properties of the modal phase factor:

$$e^{-j\frac{v\cdot(v+2)\cdot\pi}{3\cdot L_\pi}\cdot L} \tag{6.8}$$

it is also possible to prove that:

$$v\cdot(v+2) \quad \begin{cases} even \text{ if } v \text{ is } even \\ odd \text{ if } v \text{ is } odd \end{cases} \tag{6.9}$$

and

$$\overline{E}_v(\text{-x}) = \begin{cases} \overline{E}_v(\text{x}) \text{ if } v \text{ is } even \\ -\overline{E}_v(\text{x}) \text{ if } v \text{ is } odd \end{cases} \tag{6.10}$$

that is, the function v is an even function if v is even, while it is an odd function if v is odd. Observing the eq. (6.7) it emerges that if:

$$e^{-j\frac{v\cdot(v+2)\cdot\pi}{3\cdot L_\pi}\cdot L} = 1 \tag{6.11}$$

with $v = 0,1,2,...N-1$ then the total field will be given by:

$$e(x,L) = \left(\sum_{v=0}^{N-1} A_v \cdot \overline{E}_v(x)\right) \cdot e^{-j\cdot\beta_0\cdot L} = e_{ing}(x) \cdot e^{-j\cdot\beta_0\cdot L} \tag{6.12}$$

Without a phase shift, a replica of the incoming field is obtained. The eq. (6.11) is satisfied if $\frac{L}{(3\pi)}$ is an even integer, that is:

$$L = p \cdot 3 \cdot L_\pi \tag{6.13}$$

with $p = 2,4,6$ ....The condition concerns the case in which all the phase-shifts related to the various modes are integer multiples of 2π. In this case, the modes interfere with each other with the same phase relationships of the input and therefore the generated field will be an exact replica of the input one. Instead:

$$e^{-j \cdot \frac{v \cdot (v+2) \cdot \pi}{3 \cdot L_\pi} \cdot L} = (-1)^v \tag{6.14}$$

with $v = 0,1,2,\ldots N-1$ then we have that:

$$e(x,L) = \left(\sum_{v=even} A_v \cdot \overline{E}_v(x) - \sum_{v=odd} A_v \cdot \overline{E}_v(x) \right) \cdot e^{-j \cdot \beta_0 \cdot L} \tag{6.15}$$

In this case according to eq. (6.10) we have that:

$$e(-x,L) = \left(\sum_{v=even} A_v \cdot \overline{E}_v(x) - \sum_{v=odd} A_v \cdot \overline{E}_v(x) \right) \cdot e^{-j \cdot \beta_0 \cdot L} = e_{ing}(x) \cdot e^{-j \cdot \beta_0 \cdot L} \tag{6.16}$$

Therefore, the profile of the field is a mirror image of the one in input with respect to the center of the multimodal region. This second condition is relative to the case in which the displacements are odd and even multiples of π. The even modes will therefore be all in phase with each other, even

the odd ones, but in phase opposition with respect to the peers. In order for the eq. (6.14) to be satisfied, it is necessary to have that:

$$v \cdot (v+2) \cdot \frac{L}{(3 \cdot L_\pi)} = \begin{cases} even \text{ if } v \text{ is } even \\ odd \text{ if } v \text{ is } odd \end{cases} \qquad (6.17)$$

Based on the properties of the product among natural numbers, it is equivalent to require that $\frac{L}{(3\pi)}$ be odd. This condition occurs when $L = p \cdot 3L$ with $p = 1,3,5$ .... identical replicas of the incoming field are presented alternatively along the multimodal region at distances from each other. In addition to the individual images, there are sections where multiple images of the input field can be observed. At half distance between the identical image and the mirror image, which we have for the condition:

$$L = \frac{p}{2} \cdot 3L_\pi \qquad (6.18)$$

for $p = 1,3,5$ .... the total field will therefore be:

$$e(x, \frac{p}{2} \cdot 3 \cdot L_\pi) = \left(\sum_{v=0}^{N-1} A_v \cdot \overline{E}_v(x) \cdot e^{-j \cdot v \cdot (v+2) \cdot p \cdot \frac{\pi}{2}} \right) \cdot e^{-j \cdot \phi_0} \qquad (6.20)$$

with $\Phi_0 = \beta_0 \cdot (\frac{p}{2}) \cdot 3L_\pi$ for $p = 1,3,5...$ According to eq. (6.9) and eq. (6.10) and is an odd integer and remembering that:

$$e\left(x, \frac{P}{2} \cdot 3 \cdot L_x\right) = (\sum_{v=even} A_v \cdot \bar{E}_v(x) + (-j)^p \sum_{v=odd} A_v \cdot \bar{E}_v(x)) \cdot e^{-i\phi_0} =$$

$$\left(\frac{1+(-j)^p}{2} \cdot e_{ing}(x) + \frac{1-(-j)^p}{2} \cdot e_{ing}(-x) \right) \cdot e^{-i\phi_0} \qquad (6.21)$$

The field is given by the sum of two pairs of amplitude $\frac{1}{\sqrt{2}}$ that are in quadrature between them. Each pair consists of two images of the input field in a mirror position with respect to the guide axis. For $p = 1$ or $L = \frac{3}{2L_\pi}$ we can obtain:

$$e(x, \frac{p}{2} \cdot 3 \cdot L_\pi) = \left(\frac{1-j}{2} \cdot e_{ing}(x) + \frac{1+j}{2} \cdot e_{ing}(-x) \right) \cdot e^{-j \cdot \phi_0} = \frac{1}{\sqrt{2}} \cdot \left(e_{ing}(x) + j \cdot e_{ing}(-x) \right) \cdot e^{-j \cdot (\phi_0 + \frac{\pi}{4})}$$

(6.22)

completely identical to the output field of a coupler with $L_{acc} = \frac{1}{2} L_c$. It is possible to prove that at this distance:

$$L = \frac{p}{N} \cdot 3 \cdot L_\pi \qquad (6.23)$$

with p and N integers without common dividers, the overall field is made up of N replicas of amplitude of $\frac{1}{\sqrt{N}}$. The relationships referring to a generic distribution of the input field do not imply any constraints or relation of coefficients A_v. In this case, there is talk of general interference. By appropriately exciting the multimode region it is also possible to check the values of the coefficients obtaining replicas of the input field at distances lower than those found so far, with evident advantage in terms of reducing the size of the component. In this case we talk about narrow interference. Note that if $v(v + 2)$ were divisible by an integer q namely $v \cdot (v + 2) = m \cdot q$ with m as integer, the modal phase factor would become:

$$e^{j \cdot v \cdot (v+2) \cdot \frac{\pi \cdot L}{3 \cdot L_\pi}} = e^{j \cdot m \cdot q \cdot \frac{\pi \cdot L}{3 \cdot L_\pi}} \qquad (6.24)$$

Its periodicity would pass from $6 \cdot L_\pi$ to $\frac{6 \cdot L_\pi}{q}$. It is easy to prove that all the previously highlighted properties would be obtained on the scale distances of $\frac{1}{q}$. Unfortunately, the divisibility for a common integer is not satisfied for all the possible values of ν but only for particular subsets. For example, if we consider a function f:

$$f(\nu \cdot (\nu + 2)) = 0 \tag{6.25}$$

with values of $\nu \neq 2, 5, 8$ it is sufficient to have $A_\nu = 0$ for $\nu = 2, 5, 8$. If the input field of the multimodal region is such as not to excite the modes with the period of $\nu = 2,5,8$, the modal phase factor is reduced by a factor of three. It follows that, in order to obtain $L = p \cdot L_\pi$, there will be specular and identical replicas of the input field, while for $L = \frac{p}{2} \cdot L_\pi$, pairs of images are formed in a mirror position and finally for $L = \frac{p}{N} \cdot L_\pi$, the replicas are N. One way to excite the selective modes of the type eq. (6.25) is to use a pair of guides centered in $x \pm \frac{W}{6}$. The modes with $\nu = 2, 5, 8$ have a zero with odd symmetry.
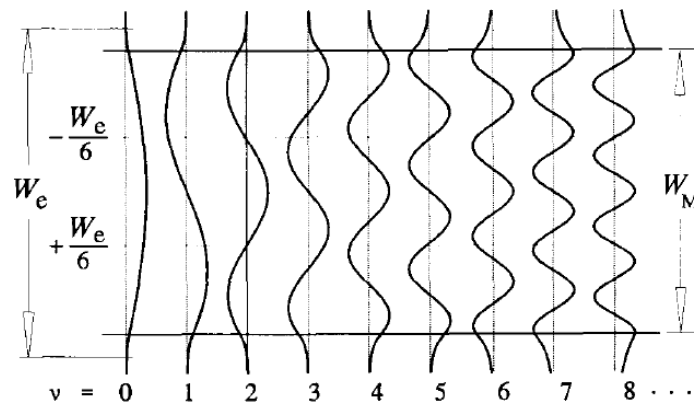
Fig. 6.1. In this picture the amplitude normalized of the 9 modes inside a step-index multimode waveguides is showed [5].

On the opposite side, the modes of the entrance waveguides present in these points have an even symmetry. The corresponding integrals eq. (6.5) will all be null. When the condition eq. (6.25) is satisfied, the mode pairs 0-1, 3-4, 6-7, ... all have the same phase relationships:

$$\beta_0 - \beta_1 = \frac{\pi}{L_\pi}, \ \beta_3 - \beta_4 = \frac{3 \cdot \pi}{L_\pi}, \ \beta_6 - \beta_7 = \frac{5 \cdot \pi}{L_\pi}, \tag{6.26}$$

We have $z = \frac{L_\pi}{2}$ in each pair of the phase shift of $\frac{\pi}{2}$ compared to the same mode, while $z = L_\pi$ in the phase difference is π. This defines that the output of the multimode region is positioned in $\pm \frac{W}{6}$ and a transfer matrix of the directional coupler is obtained with $L_{acc} = \frac{1}{2} L_c$, only with a smaller size and less sensitivity to the imperfections due to the production processes. As a result, $f \cdot (v \cdot (v + 2)) = 0$ for v indicates that the periodicity of the modal phase factor is reduced by a factor of four simply by placing the input guide at the center of the multimode region. In fact, all the modes with odd symmetry will not be excited. In this way, distributions are obtained with replicas of the input field, symmetrically arranged with respect to the axis of the multimodal region, equally spaced by a quantity of $\frac{W}{N}$, with amplitude of $\frac{1}{\sqrt{N}}$ at a distance from the input section of:

$$L = \frac{p}{N} \cdot \frac{3 \cdot L_\pi}{4} \tag{6.27}$$

In order for the number of guided modes to be at least N, it is necessary that you have:

$$v = \pi \cdot \frac{W}{\lambda} \cdot \sqrt{n_{co}^2 - n_{cl}^2} > (N-1) \cdot \frac{\pi}{2} \qquad (6.28)$$

with simple steps:

$$W > \frac{(N-1) \cdot \lambda}{2 \cdot \sqrt{n_{co}^2 - n_{cl}^2}} \qquad (6.29)$$

Replacing the eq. (6.29) in eq. (6.3) we have that:

$$L_\pi > \frac{\lambda}{3} \cdot (N-1)^2 \cdot \frac{n_{co}}{n_{co}^2 - n_{cl}^2} \qquad (6.30)$$

It is, however, possible to calculate through a matrix system *NxN* the amplitude of the signals output by an MMI in which M is equal to N.

6.2 Simulations of MMI in SiO$_2$–SiON

The simulations concerning multimodal interferometers were performed starting from a paper in the literature [143]. The paper refers to an MMI that works as a demultiplexer. It separates the two input wavelengths that are respectively 980 nm and 1550 nm. The MMI is simulated using unbalanced waveguides.
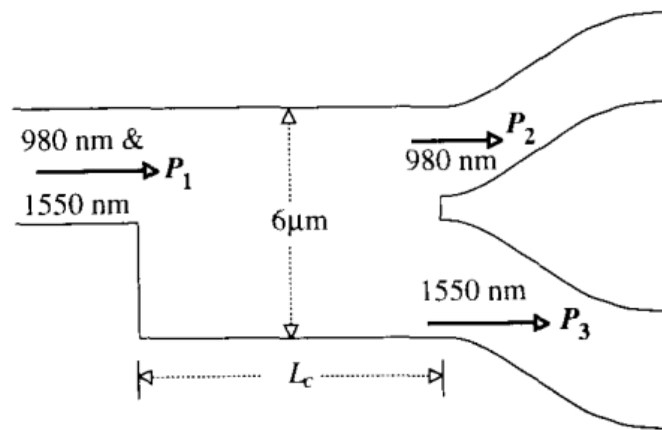
Fig. 6.2. Top view of a multimodal interferometer. Two different wavelengths of 980 nm and 1550 nm enter in the unbalanced input waveguide. The 980 nm wavelength is in a bar-coupled state and the 1550 nm wavelength is cross-state [143].

In this case, the unbalanced input serves to determine a greater excitement of the modes within the waveguide. In the paper [143], simulations have been done through a proprietary mathematical model. The results obtained between the simulation part and experimental characterization are not equivalent. In fig. 6.3 a) is depicted the contrast between the two wavelengths. The 1550 nm one's contrast is less than the 980 nm. After the realization of the prototype the characterization of the sample demonstrates that the two contrasts were shifted with respect to the simulations because of the presence of leaky waves, and they have been neglected in the model as depicted in fig. 6.2. In the model that I reconstructed faithfully following all the parameters of the device, I obtained a model equivalent to the one realized in ref [143]. In the representation of the results obtained, BeamPROP® also takes into account the leaky waves, thus obtaining a result which matches better with the experiments as shown in fig. 6.3.
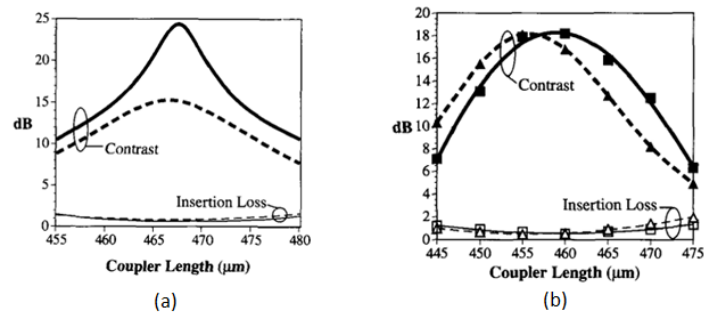
Fig. 6.3. Simulation of a multimodal interferometer in a), experimental results in b). With the ellipses the simulated and real values are indicated. We note the difference in values caused by the non-consideration of leaky waves [143].

6.3 Simulation of MMI in LC:PDMS technology

Starting from the model in which all possible light propagation phenomena are taken into consideration within the multimode interferometer, I simulated an MMI that acts as an optical demultiplexer using the LC: PDMS technology. The structure of an MMI consists of an input waveguide and two output waveguides, all in single mode connected by a multimode waveguide section, as depicted in fig. 6.4 .
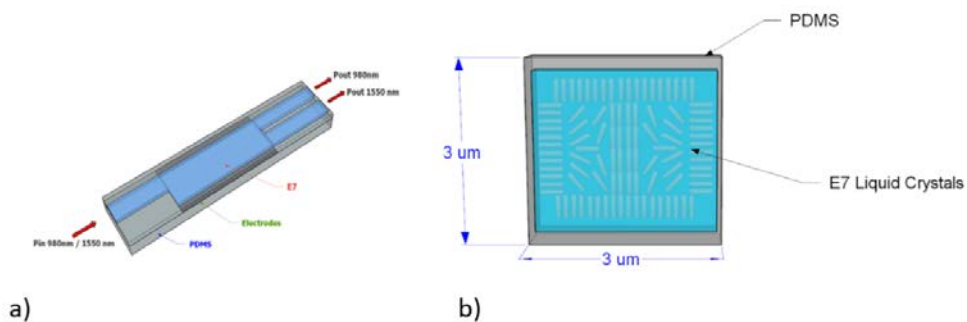
Fig. 6.4. a) Representation of multimodal interferometer working with two different wavelengths 980 and 1550. In this case the MMI works as a demultiplexer. The 980 nm signal leaves the left-hand guide, the 1550-signal goes out of the right-hand drive. The side electrodes are present to have an electro-optical control of the structure. b) Orientation of the LC molecules in the input waveguide [3].

156

The MMI in LC:PDMS technology was designed to operate at 980 nm and 1550 nm, wavelengths typically used in erbium-doped optical fiber optic amplifiers or can also be used to make compact optical sensors. Two coplanar electrodes are positioned along the multimode section to allow to tune the refractive index of the NLC core in order to maximize both the optical output power at the wavelength of 980 nm and 1550 nm. There are two output waveguides: one on the left-hand side with an output waveguide at the wavelength of 980 nm and one on the right-hand side with 1550 nm, as shown in fig. 6.4. In the designed structure, the height of all waveguides is 3 µm, the width of the input waveguide, the multi-mode section, the left output waveguide and the output waveguide right are 3, 6, 2.3 µm, respectively. The results of simulations performed are shown in fig. 6.5.
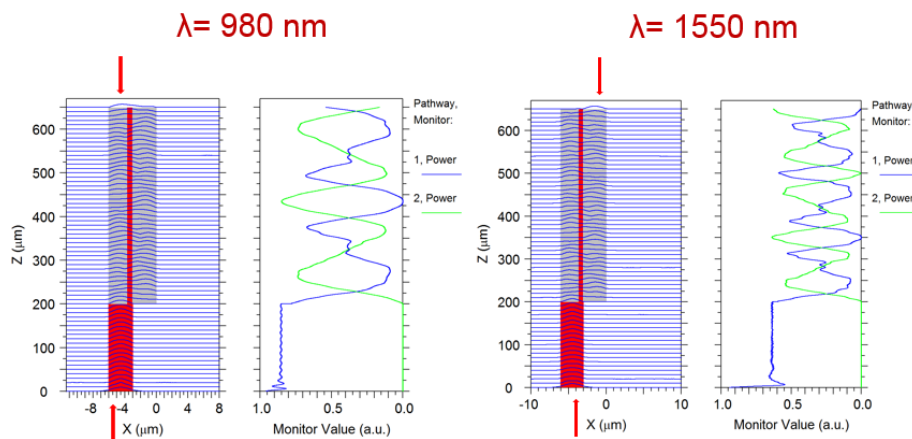
Fig. 6.5. Simulation performed through BeamPROP®. On the left-hand side figure the output power for the 980 nm, on the right-hand side the 1550 nm are represented respectively. The monitors plot the power level at 980 nm with blu color and 1550 nm at green color.

A Gaussian pulse centered at x= -4.5 µm was launched, which propagated in a 3 µm square guide for a length of 200 µm, and subsequently entered the multimode guide with dimensions of 6 µm in width and 3 µm in height. In this configuration 14 modes were excited at 980 nm and 12 modes at 1550 nm in the multimode section. This ratio was calculated as the ratio between the power at 1550 nm and the power at 980 nm both outgoing on the right-hand waveguide, represented by the red line. The blue dotted line is the ratio between the power at 980 nm and the power at 1550 nm on the left output waveguide. Fig. 6.6 a) and b) show the highest extinction values obtained respectively for refractive indices of the LC at 1.650 and 1.690. At the refractive index of 1.650 I obtained an ER of 11.40 dB for a length of 733 µm of the central part of the MMI and an ER of 10.50 dB at 743 µm for a refractive index of 1.690. In order to achieve the same results for an ER of 11.4 dB which corresponds of a refractive index of 1.650 is necessary to apply a voltage of about 7 V [3].
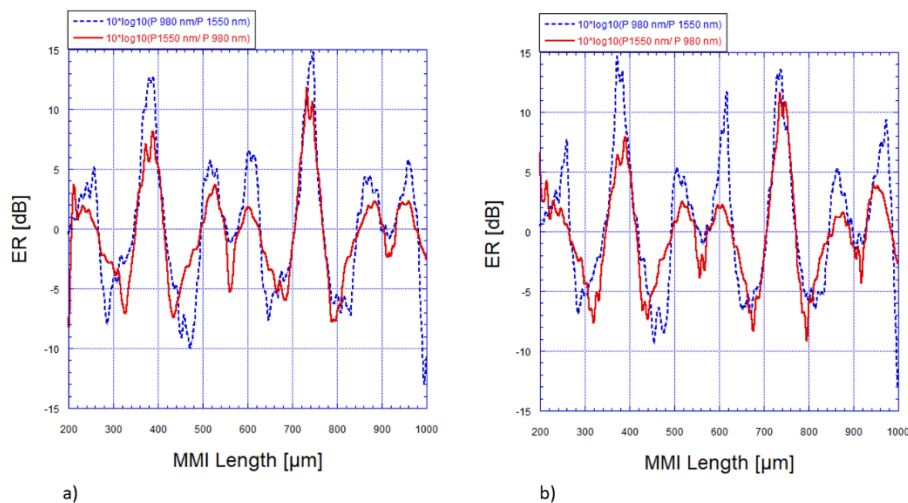
Fig. 6.6. Representation of MMI extinction values: a) At 733 µm for a refractive index of 1.650. the ER achieved was 11.40 dB. b) At 743 µm for a refractive index of 1.690 the ER calculated was 10.50 dB.

Conclusions

In literature there are many examples of MMI devices using the self-image principle [118], [144-146].

Many materials are used for the fabrication of the MMI, such as GaAS, GaAsP, InGaAsP to Si or Si on SiO_2 [147-153] up to photosensitive polymers and photonic crystals. The results obtained using these materials demonstrate power loss between 0.5 and 5 dB and a contrast starting from 13 dB to 18 dB [143], [154-156]. MMI device simulations led to an extinction ratio higher than 10 dB.

Chapter 7: Conclusions

LC: PDMS technology allows to fabricate and implement optofluidic devices for different research applications ranging from telecommunications to biosensing. Furthermore, this technology fulfills the low-cost requirements that are crucial for large-scale industrial production. Indeed, the natural distribution of LC molecules, homoeotropic arrangement, inside PDMS channels makes these devices easy to fabricate.

In the first stage of this PhD I dealt with the design, fabrication and testing of LC:PDMS waveguides. In the second stage I focused on theoretical simulations of the optofluidic devices such as directional couplers, zero gap directional couplers and multimode interferometers.

The minimization of the Oseen-Frank energy equation concerning the electromagnetic and mechanical response of LC was aimed to simulate the behaviors of the optofluidic devices. Starting from this equation in which I considered the contribution of the electric field applied to the LC molecules. A COMSOL Multiphysics® model was created through the use of the partial differential equation (PDE) module. Electrodes' models where added to the LC:PDMS channel model to reflect the performance of the real devices. The simulations aimed at getting a deeper insight on the LC refractive index behavior under the applied electric field. The results indicated that a minimum voltage of 4 V is required to realign the 5CB LC inserted into a rectangular 6 x 3 μm waveguide.

The LC:PDMS prototypes were fabricated and characterized by a setup composed of a DFB laser with a wavelength of 1560 nm, retarding plates,

and a power meter. Instruments were connected by using a single mode fiber. Light transmission proved to be independent of the polarization state. Propagation loss turned out to be 8 dB/cm which can improved in channel with improved edges.

Directional couplers were designed and simulated by using the E7 LC refractive index data imported from the calculations performed by using COMSOL Multiphysics®. These data were utilized as input data to calculate the extinction ratio (ER) of directional couplers for different gaps across the two waveguides Coupling lengths less than 100 µm were achieved. The maximum value of the ER attained was over 20 dB for a coupling length of 45 µm and a gap of 0.3 µm.

Zero-gap directional couplers were studied and simulated by using different cladding materials: BK7 and PDMS. The reported ER values for the BK7 cladding and E7 LC, varied according to the core size, (3 µm and 4 µm) between 9 and 10 dB. The LC:PDMS wave propagation simulations turned out be +18 dB and -16 dB at the two outputs for a core dimension of 3 x 3 µm.

The multimodal interferometer (MMI) represents another optoelectronic devices that I designed and simulated in LC:PDMS technology. Both theoretical and fabrication aspects needed to be studied in order to investigate the multimodal interferometer performance. In particular, BeamPROP® had to be implemented. Preliminary studies were performed by combining the refractive index of PDMS with the constant refractive index of the E7 LC. The ER attained was about 12 dB. To improve the ER value, it would be necessary to refine the MMI geometries.

The fabrication of co-planar electrodes integrated into the LC:PDMS devices to control LC orientation relied on different processes: thermal evaporation, RF magnetron sputtering, and electroplating. The PDMS high thermal expansion coefficient compared to sputtered or evaporated metals (Al, Cr and Ti-W) resulted into rough and non-adherent deposits. The evaporated samples were the most affected by delamination. The superficial ripples were visible even without any microscopic examination. Thereby, sputtering of ITO and Cr was evaluated as deposition techniques for the devices fabrications. ITO is routinely employed as optically transparent and electrically conductive material in optoelectronic devices such as solar cells and photodetectors. However, the surface roughness of the ITO film didn't allow for electrical characterization. Chromium, turned out to be the most suitable metal from a mechanical resilience and electrical conductivity stand point (e.g. R= 4945.63 [kΩ]). Although Chromium films showed promising results, physical masks are mandatory for their deposition. Hence, the fabrication of simple and low cost devices is precluded.

Electroplating is a simple process which doesn't require costly high vacuum equipment. Furthermore, it is easy to implement. The prototypes made by electroplating showed an excellent adhesion to the PDMS substrate. However, the current density during the electrodeposition process needed to be adjusted accurately. Indeed, hydrogen evolution during the electroplating might bring about delamination during the successive etching step. To mitigate this effect ammonium persulphate was used as the preferred etchant. The final devices proved to be a reliable waveguide capable of switching between two optical states according to the applied voltage. Such an effect is due to the re-orientation of the

molecules of the LC under the action of the electric field. Several experiments proved that almost 2 V is the threshold voltage to re-orientate the LC molecules. Hence, low-power consumption LC:PDMS devices can be fabricated and implemented.

Future work will focus on testing the prototypes for mechanical resilience and flexibility. Moreover, a detailed study to establish a correlation between the macroscopic stress induced on the sample and LCs orientation under the action of the electric field, is currently being performed.

Bibliography

[1] C. Khoo, "Liquid Crystals Physical Properties and Nonlinear Optical Phenomena", [2nd], *Wiley*, (1994).

[2] C. Khoo and S.T. Wu, "Optics and Nonlinear Optics of liquid crystals", [1st], *Word Scientific*, (1993).

[3] R. Asquini, C. Chiccoli, P. Pasini, L. Civita, A. d'Alessandro, "Low power photonic devices based on electrically controlled nematic liquid crystals embedded in poly(dimethylsiloxane)", *Liq. Cryst.*, vol. 45, no. 13-15, pp. 1-10, (2018).

[4] J. P. Lagerwall, G. Scalia, "A new era for liquid crystal research: Application of liquid in soft matternano,bio and microtechnology" *Curr. App. Phys.*, vol. 12, no. 6, pp. 1387-1412, (2012).

[5] S. Saliba, P. Davidson, M. I. Clerc, C. Mingotaud, L. K. Myrtil, J. D. Marty, "Facile direct synthesis of ZnO nanoparticles within lyotropic liquid crystals: towards organized hybrid materials", *J. Mater. Chem.*, vol. 45, no. 21, pp. 18191-18194, (2011).

[6] Y. F. Chen, L. Jiang, M. Mancuso, A. Jain, V. Oncescu, D. Erickson, "Optofluidic opportunities in global health, food, water and energy", *Nanoscale*, vol. 4, no. 16, pp. 4839-4857, (2012).

[7] A. d'Alessandro, L. Martini, L. Civita, R. Beccherelli, R. Asquini, "Liquid crystal waveguide technologies for a new generation of low power photonic integrated circuits", *Proc. Emerging Liquid Crystal Technologies X*, vol. 9384, pp. 93840-93848, (2015).

[8] R. Asquini, L. Civita, L. Martini, A. d'Alessandro, "Design of Optical Directional Couplers Made of Polydimethysiloxane liquid Crystal Channel Waveguides", *Mol. Cryst. Liq Cryst.*, vol 619, no 1, pp 12-18, (2015).

[9] L. Eldada, L. W. Shacklette, "Advances in Polymer Integrated Optics", *IEEE J. Quantum Electron.*, vol 6, no. 1, pp. 54-68, (2000).

[10] X. Fan, I.M. White, "Optofluidic microsystems for chemical and biological analysis", *Nat. Photonics*, vol. 5, no. 10, pp. 591-597, (2011).

[11] S. Mandal, J. M. Goddard, David Erickson, "A multiplexed optofluidic biomolecular sensor for low mass detection", *Lab Chip*, vol. 9, no. 20, pp. 2924–2932, (2009).

[12] C. Y. Chen, C. L. Chang, C. W. Chang, S.C. Lai, T. F. Chien, H. Y. Huang, J. C. Chiou, C. H. Luo, "A Low-Power Bio-Potential Acquisition System with Flexible PDMS Dry Electrodes for Portble Ubiquitous Healthcare Applications", *Sensors*, vol. 13, no. 3, pp. 3077-3091, (2013).

[13] R. H. Liu, J. Yang, R. Lenigk, J. Bonanno, P. Grodzinski, "Self-Contained, Fully Integrated Biochip for Sample Preparation, Polymerase Chain Reaction Amplification, and DNA Microarray Detection", *Anal. Chem.*, vol. 76, no. 7, pp. 1824-1831, (2004).

[14] L. Civita, R. Asquini, L. Martini, A. d'Alessandro, "Short Optofluidic Directional Couplers", *Proc. IEEE Xplore 18th Italian National Conference on Photonic Technologies*, pp. 1-4, (2016).

[15] R. Asquini, L. Martini, A. d'Alessandro, "Fabrication and Characterization of Liquid Crystal Waveguides in PDMS Channels for Optofluidic Applications", *Mol. Cryst. Liq. Cryst.*, vol. 614, no. 1, pp. 11-19, (2015).

[16] R. Asquini, L. Martini, G. Gilardi, R. Beccherelli, A. d'Alessandro, "Polarization independent optofluidic nematic liquid crystal channels", *Proc. IEEE Photonic Conference*, pp. 36-37, (2014).

[17] D. A.B. Miller, "Optical interconnects to electronic chips", *Appl. Opt.*, vol. 49, no. 25, pp. 59-70, (2010).

[18] D. A.B. Miller, "Rationale and Challenges for Optical Interconnects to Electronic Chips" *Proc. of the IEEE*, vol. 88, no. 6, pp. 728-749, (2000).

[19] D. A.B. Miller, "Device requirements for optical interconnects to silicon chips", *Proc. of the IEEE*, vol. 97, no. 7, pp. 1166-1185, (2009).

[20] J. M. Koo, S. I., L. Jiang, K. E. Goodson, "Integrated Microchannel Cooling for Three-Dimensional Electroni Circuit Architectures", *J. Heat Transfer*, vol. 127, no.1, pp. 49-58, (2005).

[21] K. Banerjee, A. Mehrotra, A. S. Vincentelli, C. Hu, "On Thermal Effects in Deep Sub-Micron VLSI Interconnects", *Proc. 36th Design Automation Conference*, pp. 885-891, (1999).

[22] K. Banerjee, M. Pedram, A. H. Ajami, "Analysis and Optimization of Thermal Issues in High-Performance VLSI", *Proc. of the 2001 International symposium on Physical Design*, pp. 230-237, (2001).

[23] M. Pedram, S. Nazarian, "Thermal Modeling, Analysis, and Management in VLSI Circuits: Principles and Methods", *Proc. of the IEEE*, vol. 94, no. 8, pp. 1487-1501, (2006).

[24] J. Missinne, S. Kalathimekkad, B. v. Hoe, E. Bosman, J. Vanfleteren, G. v. Steenberge, "Stretchable optical waveguides", *Opt. Express*, vol. 22, no. 4, pp. 4168-4179, (2014).

[25] J. Wu, M. Gu, "Microfluidic sensing: state of the art fabrication and detection techniques", *J. Biomed. Opt.*, vol. 16, no. 8, pp. 1-12, (2011).

[26] D. Ozcelik, J. W. Parks, T. A. Wall, M. A. Stott, H. Cai, J. W. Parks, A. R. Hawkins, H. Schmidt, "Optofluidic wavelength division multiplexing for single-virus detection", pp. 12933-12937, *PNAS*, vol. 42, no.112, (2015).

[27] A. Sudirman, W. Margulis, "All-Fiber Optofluidic Component to Combine Light and Fluid", *IEEE Photon. Technol. Lett.*, vol. 26, no.10, pp. 1031–1033, (2014).

[28] X. Yang, X. Guo, S. Li, D. Kong , Z. Liu, J. Yang, L. Yuan, "Lab-on-fiber electrophoretic trace mixture separating and detecting an optofluidic device based on a microstructured optical fiber", *Opt. Lett.*, vol. 41, no. 8, pp. 1873-1876, (2016).

[29] D. Psaltis, W. Song, A.E. Vasdekis, "Optofluidic devices and applications", *IEEE International Electron Devices Meeting (IEDM)*, pp.1-4, (2012).

[30] A. R. Hawkins, H. Schmidt, "Handbook of Optofluidics", [1 ed.], *CRC Press*, (2010).

[31] N. Chronis, G. L. Liu, K. H. Jeong, L. P. Lee, "Tunable liquid-filled microlens array integrated with microfluidic network", *Opt. Express*, vol. 11, no. 19, pp. 2370-2378, (2003).

[32] S. K. Y. Tang, C. A. Stan, G. M. Whitesides, "Dynamically reconfigurable liquid-core liquid-cladding lens in a microfluidic channel", *Lab Chip*, vol. 8, no. 3, pp. 395–401, (2008).

[33] S. Brückner, G. Allegra, M. Pegoraro, F. P. La Mantia, L.Di Landro,M. Malinconico,R. Scaffaro, S. Paoletti,I. Donati, "Scienza e Tecnologia dei Materiali Polimerici", [3 ed.] Edises, (2016)

[34] A. Zahid, B. Dai, R. Hong, D. Zhang, "Optical properties study of silicone polymer PDMS substrate surfaces modified by plasma treatment", *Mat. Res. Express*, vol. 4, no.10, pp 1-9, (2017).

[35] N.E. Stankovaa, P.A. Atanasova, Ru. G. Nikova, R.G. Nikova, N. N. Nedyalkova, T.R. Stoyanchova, N. Fukata b, K.N. Kolevc, E.I. Valovac, J.S. Georgievac, St.A. Armyanovc, "Optical properties of polydimethylsiloxane (PDMS) during nanosecond laser processing", *Appl. Surf. Sci.*, vol. 374, no. 96-103, pp. 96-103, (2016).

[36] I. Martinček, I. Turek, N. Tarjányi, "Effect of boundary on refractive

index of PDMS", *Opt. Mater. Express*, vol. 4, no.10, pp. 1997-2005, (1997).

[37] R. Gupta, "Fabrication of stretchable compliant electrodes on PDMS with Au nanoparticles" *Bullettin of Material Science*, vol. 41, no. 114, pp. 1-5, (2018).

[38] D. Bouchta, N. Izaoumen, H. Zejl, M. El Kaouti, K. R. Temsamani, "Electroanalytical Properties of a Novel PPY/γCyclodextrin Coated Electrode", *Anal. Lett.*, vol. 38, no. 6, pp. 1019-1036, (2007).

[39] L. Xu, M. Jia, Y. Li, S. Zhanga, X. Jin, "Design and synthesis of graphene/activated carbon/polypyrrole flexible supercapacitor electrodes", *RSC Adv.*, vol. 7, no. 50, pp. 31342–31351, (2017)

[40] J. Y. Kim, K. S. Jang, "Facile Fabrication of Stretchable Electrodes by Sedimentation of Ag Nanoparticles in PDMS Matrix", *J. Nanomater*, vol. 2018, no. 1-3, pp. 1-6, (2018).

[41] J.F. Algorri, D. Poudereux, B. García-Cámara, V. Urruchi, J.M.S. Pena, R. Vergaz, M. C.García, X. Quintana, M.A. Geday, J.M. Otón, "Metal nanoparticles-PDMS nanocomposites for tunable optical filters and sensors", *Optical Data Process*, vol. 2, no. 1, pp. 1-6, (2016).

[42] G. Testa, G. Persichetti, R. Bernini, "Liquid Core ARROW Waveguides: A Promising photonic Structure for Integrated Optofluidic Microsensors", *Micromachines*, vol. 7, no. 3, pp. 1-19, (2016).

[43] D. Yin, H. Schmidt, "Optical characterization of arch-shaped ARROW waveguides with liquid cores", *Opt. Express*, vol. 13, no. 26, pp. 10564-10570, (2005).

[44] S. K. Fan, H. P. Lee, C. C. Chien, Y. W. Lu, Y. Chiuc, F. Y. Lin, "Reconfigurable liquid-core/liquid-cladding optical waveguides with dielectrophoresis-driven virtual michrochannels on an electromicrofluidic platform", *Lab Chip*, vol. 16, no. 5, pp. 1-8, (2016).

[45] D. B. Wolfe, R. S. Conroy, P. Garstecki, B. T. Mayers, M. A. Fischbach, K. E. Paul, M. Prentiss, G. M. Whitesides, "Dynamic control of liquid-core / liquid-cladding optical waveguides", *PNAS*, vol. 34, no. 101, pp. 12434-12438, (2004).

[46] C. J. S. de Matos, C. M. B. Cordeiro, E. M. Santo, J. S. K. Ong, A. Bozolan, C. H. B. Cruz, "Liquid-core, liquid-cladding photonic crystal fibers", *Opt. Express*, vol. 15, no. 18, pp. 11207- 11212, (2007).

[47] K. S. Lee, S. B. Kim, K. H. Lee, H. J. Sung, S. S. Kim, "Three-dimensional microfluidic liquid-core/liquid-cladding waveguide", *App. Phys. Lett.*, vol. 10, no. 1, pp. 1-3, (2010).

[48] J. M. Lim, S. H. Kim, J. H. Choi, S. M. Yang, "Fluorescent liquid-core/air-cladding waveguides towards integrated", *Lab Chip*, vol. 8, no. 9, pp. 1580-1585, (2008).

[49] D. V. Vezenov, B. T. Mayers, R. S. Conroy, G. M. Whitesides, P. T. Snee, Y. Chan, D. G. Nocera, M. G. Bawendi, "A Low-Threshold, High-Efficiency Microfluidic Waveguide Laser", *J. Am. Chem. Soc.*, vol. 127, no. 25, pp. 8952-8953, (2005).

[50] Khoo. "Liquid Crystals", [2 ed.], *Wiley*, (2007).

[51] H. Hiwai, J. Fukusawa, T. Suzuki, "A liquid crystal application in skin care cosmetics", *Int. J. Cosmet. Sci.*, vol. 20, no. 2, pp. 87–102, (1997).

[52] W. Zhang, L. Liu, "Study on the Formation and Properties of Liquid Crystal Emulsion in Cosmetic", *JCDSA*, vol. 3, no. 2, pp. 139-144, (2013).

[53] D. Donisi, B. Bellini, R. Beccherelli, R. Asquini, G. Gilardi, M. Trotta, A. d'Alessandro, "A Switchable Liquid-Crystal Optical Channel Waveguide on Silicon", *IEEE J. Quantum Electron.*, vol. 46, no. 5, pp. 762-768, (2010).

[54] B. Maune, R. Lawson, C. Gunn, A. Scherer, L. Dalton, "Electrically tunable ring resonators incorporating nematic liquid crystals as cladding layers", *App. Phys. Lett.,* vol. 83, no. 23, pp. 4689-4691, (2003).

[55] M. Humar, M. Ravnik, S. Pajk, I. Musevic, "Electrically tunable liquid crystal optical microresonator", *Nat. Photonics,* vol.3, no. 10, pp. 595-600, (2009).

[56] W. D. Cort, J. Beeckman, T. Claes, K. Neyts, R. Baets, "Wide tuning of silicon-on-insulator ring resonators with a liquid crystal cladding", *Opt. Lett.,* vol. 36, no. 19, pp. 3876-3878, (2011).

[57] J. Pfeifle, L. Alloatti, W. Freude, J. Leuthold, C. Koos, "Silicon-organic hybrid phase shifter based on a slot waveguide with a liquid-crystal cladding", *Opt. Express*, vol. 20, no. 14, pp. 15359-15376, (2012).

[58] C. Levallois, B. Caillaud, J.-L. de Bougrenet de la Tocnaye, L. Dupont, A. Le Corre, "Long-wavelength vertical-cavity surface-emitting laser using an electrooptic index modulator with 10nm tuning range", *App. Phys. Lett.,* vol. 89, no. 1, pp 1-3, (2006).

[59] D. Donisi, R. Asquini, A. d'Alessandro, B. Bellini, R. Beccherelli, L. De Sio and C. Umeton, "Integration and Characterization of LC/Polymer Gratings on Glass and Silicon Platform", *Mol. Cryst. Liq. Cryst.,* vol. 516, no. 1, pp. 152-158, (2010).

[60] A. d'Alessandro, R. Asquini, M. Trotta, G. Gilardi, R. Beccherelli, I. C. Khoo, "All-optical intensity modulation of near infrared light in a liquid crystal channel waveguide", *App. Phys. Lett.,* vol. 97, no. 9, pp. 1-3, (2010).

[61] A. d'Alessandro, L. Martini, G. Gilardi, R. Beccherelli, R. Asquini, "Polarization independent nematic liquid crystal waveguides for optofluidic applications", *IEEE Photon. Technol. Lett.,* vol. 27, no. 16, pp. 1709-1712, (2015).

[62] C. Tsay, S. P. Lacour, S. Wagner, B. Morrison III, "Architecture, Fabrication, and Properties of Stretchable Micro-electrode Arrays", *Proc. IEEE Sensors*, pp. 1169-1172, (2005).

[63] D. Brosteaux, F. Axisa, M. Gonzalez, J. Vanfleteren, "Design and Fabrication of Elastic Interconnections for Stretchable Electronic Circuits", *IEEE Electron. Device Lett.*, vol. 28, no.7, pp. 552-554, (2007).

[64] T. Li, Z. Suo, "Deformability of thin metal films on elastomer substrates", *Int. J. Solids Struct.*, vol. 43, no. 7, pp. 2351-2363, (2006).

[65] T. Li, Z. Suo, "Ductility of thin metal films on polymer substrates modulated by interfacial adhesion", *Int. J. Solids Struct.*, vol. 44, no. 6, pp. 1696-1705, (2007).

[66] D. S. Gray, J. Tien, C. S. Chen, "High-Conductivity Elastomeric Electronics", *Adv. Mater.*, vol. 16, no. 5, pp. 393-397, (2004).

[67] J. A. Rogers, T. Someya, Y. Huang, "Materials and Mechanics for Stretchable Electronics", *Science*, vol. 327, no. 5973, pp. 1603-1607, (2010).

[68] S. Rosset, M. Niklaus, P. Dubois, H. R. Shea, "Metal Ion Implantation for the Fabrication of Stretchable Electrodes on Elastomers", *Adv. Funct. Mater.*, vol. 19, no. 6, pp. 470-478, (2009).

[69] P. J. Hung, K. Jeong, Gang L. Liu, L. P. Lee, "Microfabricated suspensions for electrical connections on the tunable elastomer membrane", *App. Phys. Lett.*, vol. 85, no. 24, pp. 6051-6053, (2004).

[70] C. X. Liu, Jin-Woo Choi, "Patterning conductive PDMS nanocomposite in an elastomer using microcontact printing", *J. Micromech. Microeng.*, vol. 19, no. 6, pp. 1-7, (2009).

[71] I. D. Johnston, D. K. Mc Cluskey, C. K. L. Tan M. C. Tracey, "Mechanical characterization of bulk Sylgard 184 for microfluidics and microengineering", *J. Micromech. Microeng.*, vol. 24, no. 3, pp. 1-7, (2014).

[72] Y. Shao, M. A. Brook, "Structured metal films on silicone elastomers", *J. Mater. Chem.*, vol. 20, no. 39, pp. 8548–8556, (2010).

[73] B. Moazzez, S. M. O'Brien, S. E. F. Merschrod, "Improved adhesion of gold thin films evaporated on polymer resin: applications for sensing surfaces and MEMS", *Sensors (Basel)*, vol. 13, no. 6, pp. 7021-7032, (2013).

[74] K. Wasa, I. Kanno, H. Kotera, "Handbook of Sputter Deposition Technology", [2nd], *Elsevier*, (2012).

[75] O. Tuna, Y. Selamet, G. Aygun, L.Ozyuzer, "High quality ITO thin films grown by dc and RF sputtering without oxygen", *J. Phys. D: Appl. Phys.*, vol. 43, no. 5, pp. 1-7, (2010).

[76] S. Ishibashi, Y. Higuchi, Y. Ota, and K. Nakamura, "Low resistivity indium–tin oxide transparent conductive films. I. Effect of introducing H_2O gas or H_2 gas during direct current magnetron sputtering", *J. Vac. Sci. Technol. A*, vol. 42, no.8-9, pp. 1399-1402, (1990).

[77] K. Utsumi, O. Matsunaga, T. Takahata, "Low resistivity ITO film prepared using the ultra high density ITO target", *Thin Solid Films*, vol. 334, no. 1-2, pp. 30-34, (1998).

[78] W. Zhang, G. Zhu, L. Zhi, H. Yang, Z. Yang, A. Yu, H. Xu, "Structural, electrical and optical properties of indium tin oxide thin films prepared by RF sputtering using different density ceramic targets", *Vacuum*, vol. 86, no. 8, pp. 1045-1047, (2012).

[79] F. Kurdesau, G. Khripunov, A.F. da Cunha, M. Kaelin, A.N. Tiwari, "Comparative study of ITO layers deposited by DC and RF magnetron sputtering at room temperature", *J. Non Cryst. Solids*, vol. 352, no. 9-20, pp. 1466-1470, (2006).

[80] D. R. Cairns, R. P. Witte II, D. K. Sparacin, Suzanne M. Sachsman, D. C. Paine, G. P. Crawford, "Strain-dependent electrical resistance of tin-

doped indium oxide on polymer substrates", *Appl. Phys. Lett.*, vol. 76, no. 11, pp. 1425-1427, (2000).

[81] M. Schlesinger, M. Paunovic, "Modern Electroplating", [5th], *Wiley*, (2014).

[82] C. E. Nwankire, A. Venkatanarayanan, R. J. Forster, J. Ducrée, "Enhanced gold to polymer adhesion for integrated electrochemicasl biosensing on cost efficient lab on a chip cartridges", *19th International Conference on Miniaturized Systems for Chemistry and Life Sciences*, pp. 1707-1709, (2015).

[83] O. Graudejus, P. Görrn, S. Wagner, "Controlling the Morphology of Gold Films on Poly(dimethylsiloxane)", *ACS Appl. Mater. Interface*, vol. 2, no. 7, pp. 1927-1933, (2010).

[84] A. Larmagnac, S. Eggenberger, H. Janossy Janos V*örö*s, "Stretchable electronics based on Ag-PDMS composites", *Sci. Rep.*, vol. 4, no. 1, pp. 1-7, (2014).

[85] T. Adrega, S. P. Lacour, "Stretchable gold conductors embedded in PDMS and patterned by photolithography: fabrication and electromechanical characterization", *J. Micromech. Microeng.*, vol. 20, no. 5, pp. 1-8, (2010).

[86] W. A. Strauss, "Partial Differential Equations", [8 ed.], *Wiley*, (2007).

[87] A. Quarteroni, "Modellistica Numerica per problemi differenziali", [6 ed.], *Springer*, (2016).

[88] A. Quarteroni, F. Saleri, "Calcolo scientifico: Esercizi e problemi risolti con Matlab ed Octave", [6 ed.], *Springer*, (2017).

[89] J. Chaskalovic, "Finite Element Methods for Engineering Sciences: Theoretical Approach and Problem Solving Techniques", [1 ed.], *Springer*, (2010).

[90] J. v. Roey, J. v. d. Donk, P. E. Lagasse, "Beam-propagation method: analysis and assessment", *J. Opt.*, vol. 71, no. 7, pp. 803-810, (1981).

[91] W. P. Huang, "Simulation of three-dimensional optical waveguides by a full-vector beam propagation method", *IEEE J. Quantum Electron.*, vol. 29, no. 10, pp. 2639-2649, (1993).

[92] Y. Chung, N. Dagli, "An assessment of finite difference beam propagation method", *IEEE J. Quantum Electron.*, vol. 20, no. 8, pp. 1335-1339, (1990).

[93] M. Doumic, F. Duboc, F. Golse, R. Sentis, "Simulation of laser beam propagation with a paraxial model in a tilted frame", *J. Comput. Phys.*, vol. 228, no. 3, pp. 861–880, (2009).

[94] R. Y. Rubinstein, "Simulation and Monte-Carlo method", [2 nd], *Wiley-Interscience*, (1991).

[95] A. d'Alessandro, R. Asquini, C. Chiccoli, L. Martini, P. Pasini C. Zannoni, "Liquid Crystal Channel Waveguides: A Monte Carlo Investigation of the Ordering", *Mol. Cryst. Liq. Cryst.*, vol. 619, no. 42-48, pp. 42-48, (2015).

[96] K. A. Rutkowska, T. R. Woliński, R. Asquini, L. Civita, L. Martini and Antonio d'Alessandro, "Electrical tuning of the LC:PDMS channels", *Photonics. Lett. Pol,* vol. 9, no. 2, pp. 48-50, (2017).

[97] http://web.mst.edu/~stutts/SupplementalNotes/Lagrange.pdf

[99] L. Civita, R. Asquini, S. Quaranta, A. d'Alessandro, *Mol. Cryst. Liq. Cryst.*, accepted to be published (2018).

[100] S. Selleri, L. Vincetti, A. Cucinotta, "Componenti Ottici e Fotonici", [1 ed.], *Società editrice Esculapio*, (2012).

[101] K. S. Chiang, "Theory of pulse propagation in optical directional couplers", *J. Non. Opt.*, vol. 14, no. 2, pp. 133-147, (2005).

[102] S. L. Chuang, "Application of the strongly coupled-mode theory to integrated optical devices", *IEEE J. Quantum Electron.*, vol. 23, no. 5, pp. 499-509, (1987).

[103] J Čtyroký, L. Thylén, "Analysis of a directional coupler by coupled modes of a single waveguide", *Opt. Lett.*, vol. 19, no. 20, pp. 1621-1623, (1994).

[104] N. Keil, H. H. Yao, C. Zawadzki, "Polymer waveguide optical switch with < -40 dB polarisation independent crosstalk", *Electron. Lett.*, vol. 32, no.7, pp. 655-657, (1996).

[105] W. H. Steier, A. Chen, S. S. Lee, S. Garner, H. Zhang, V. Chuyanov, L. R. Dalton, F. Wang, A. S. Ren, C. Zhang, G. Todorova, A. Harper, H. R. Fetterman, D. Chen, A. Udupa, D. Bhattachary, B. Tsa, "Polymer electro-optic devices for integrated optics", *Chem. Phys.*, vol. 245, no.1-3, pp. 487-506, (1998).

[106] T. Watanabe, N. Oba, S. Hayashida, T. Kurihara, S.Imamura, "Polymeric optical waveguide circuits formed using silicone resin", *J. of Lightwave Technol.*, vol. 16, no.6, pp. 1049-1055, (1998).

[107] B.M.A. Rahman, T. Wongcharoen, and K.T.V. Grattan, "Characterization of directional coupler-based optoelectronic devices", *Proc. IEEE High Performance Electron Devices for Microwave and Optoelectronic Applications*, pp. 38-42, (1996).

[108] E. v. Tomme, P. v. Daele, R. Baets, "Guided wave modulators and switches fabricated in electro-optic polymers", *J. Appl. Phys.*, vol. 69, no. 9, pp. 6273-6276, (1991).

[109] H. Ma, A.K.Y. Jen, L.R. Dalton, "Polymer-Based Optical Waveguides: Materials, Processing, and Devices", *Adv. Mat.*, vol. 14, no. 19, pp. 1339-1365, (2002).

[110] S. Somekh, E. Garmire, A. Yariv, H.L. Garvir, R.G. Hunsperger, "Channel optical waveguide directional couplers", *App. Phys. Lett.*, vol. 22, no. 2, pp. 46-47, (1973).

[111] C. P. Wen, "Coplanar-Waveguide Directional Couplers", *IEEE Trans. Microw. Theory Tech.*, vol. 18, no. 6, pp. 318-322, (1970).

[112] W. P. Huang, "Coupled-mode theory for optical waveguides: an overview", *J. Opt Soc. Am.*, vol. 11, no. 3, pp. 963-983, (1994).

[113] E. A. J. Marcatili, "Dielectric rectangular waveguide and directional coupler for integrated optics", *Bell System Techincal Journal*, pp. 2071-2102, (1969).

[114] H. Kogelnik, R. V. Schmidt, "Switched Directional Couplers with Alternating Δβ", *IEEE J. Quantum Electron.*, vol. 12, no. 7, pp. 396-401, (1976).

[115] H.F. Taylor, "Optical switching and modulation in parallel dielectric waveguides", *J. App. Phys.*, vol. 44, no. 7, pp. 3257-3262, (1973).

[116] C. T. Tsai, B. Kim, F. R. E. Akkari, "Optical channel waveguide switch and coupler using total internal reflection", *IEEE J. Quantum Electron.*, vol. 14, no. 7, pp. 513-517, (1978).

[117] R. C. Youngquist, L. F. Stokes, H. J. Shaw, "Effects of normal mode loss in dielectric waveguide directional couplers and interferometers", *IEEE J. Quantum Electron.*, vol. 19, no. 12, pp. 1888-1896, (1983).

[118] J. Leuthold, J. Eckner, E. Gamper, P. A. Besse, H. Melchior, "Multimode interference couplers for the conversion and combining of zero- and first-order modes", *J. Ligthwave Technol.*, vol. 16, no. 7, pp. 1228-1239, (1998).

[119] R. Asquini, A. Fratalocchi, A. d'Alessandro, G. Assanto, "Electro-optic routing in a nematic liquid-crystal waveguide", *App. Opt.*, vol. 44, no. 19, pp. 4136-4143, (2005).

[120] C. Z. Zhao, "Zero-gap directional coupler switch integrated into a silicon-on insulator for 1.3-μm operation", *Opt. Lett.*, vol. 21, no. 20, pp. 1664-1666, (1996).

[121] K. Goel, W. S.C. Chang, "Extinction ratio degradation due to asymmetry in zero-gap directional coupling and crossing channel switches", *IEEE J. Quantum Electron.*, vol. 23, no. 12, pp. 2216-2223, (1987).

[122] R. A. Forber, E. Marom, "Symmetric directional coupler switches", *IEEE J. Quantum Electron.*, vol. 22, no. 6, pp. 911-919, (1986).

[123] J. G. Grote, "Polymer Integrated Optic Zero-Gap Directional Coupler", *Mat. Res. Soc. Symp.*, vol. 413, pp. 231-240, (1995).

[124] B. K. Yang, S. Y. Shin, D. Zhang, "Ultrashort Polarization Splitter Using Two-Mode Interference in Silicon Photonic Wires, *IEEE Photon. Technol. Lett.*, vol. 21, no. 7, pp. 432-434, (2009).

[125] P. Ganguly, J. C. Biswas, S. K. Lahiri, "Analysis of Ti:LiNbO$_3$ zero-gap directional coupler for wavelength division multiplexer/demultiplexer", *Opt. Commun.*, vol. 208, no. 12, pp. 3269-3274, (2008).

[126] I. Kiyat, A. Aydinli, N. Dagli, "A compact silicon-on-insulator polarization splitter", *IEEE Photon. Technol. Lett.*, vol. 17, no. 1, pp. 100-102, (2005).

[127] K. Kubota, J. Noda, O. Mikami, "Traveling wave optical modulator using a directional coupler LiNbO$_3$ waveguide", *IEEE J. Quantum Electron.*, vol. 16, no. 7, pp. 754-760, (1980).

[128] Y. Shi, S. He, S. Anand, "Ultracompact directional couplers realized in InP by utilizing feature size dependent etching", *Opt. Lett.*, vol. 33, no. 17, pp. 1927-1929, (2008).

[129] F. J. Leonberger, J. P. Donnelly, C. O. Bozler, "GaAs p+n−n+ directional-coupler switch", *App. Phys. Lett.*, vol. 29, no. 10, pp. 652-654, (2008).

[130] H. Takeuchi, K. Nagata, H. Kawaguchi, K. Oe, "GaAs/AlGaAs directional coupler switch with submillimetre device length", *Electron. Lett.*, vol. 22, no. 23, pp. 1241-1243, (1986).

[131] J. Leuthold, C. H. Joyner, "Multimode interference couplers with tunable power splitting ratios", *J. Ligthwave Techn.*, vol. 19, no. 5, pp. 700-707, (2001).

[132] T.J. Tayag, D.M. Mackle, G.W. Bryant, "A manufacturable technique for implementing low-loss self-imaging waveguide beamsplitters", *IEEE Photon. Technol. Lett.*, vol. 7, no. 8, pp. 896-898, (1995).

[133] J. K. Hong, S.S. Lee, "1×2 Wavelength Multiplexer With High Transmittances Using Extraneous Self-Imaging Phenomenon", *J. Ligthwave Technol.*, vol. 25, no. 5, pp. 1264-1268, (2007).

[134] A. Mahmoodi, M. Khanzadeh, R. F. Moghaddam, K. Saito, M. Koshiba, "Design and modeling of ultrashort MMI-based couplers", *J. Mod. Opt.*, vol. 56, no. 15, pp. 1649-1658, (2009).

[135] L. B. Soldano, E.C. M. Pennings, "Optical multi-mode interference devices based on self-imaging: principles and applications", *J. Ligthwave Technol.*, vol. 13, no. 4, pp. 615-627, (1995).

[136] M. Blahut, D. Kasprzak, "Multimode interference structures properties and applications", *Opt. Appl.*, vol. 34, no. 4, pp. 573-587, (2004).

[137] J. M. Heaton, R. M. Jenkins, "General matrix theory of self-imaging in multimode interference (MMI) couplers", *IEEE Photon. Technol. Lett.*, vol. 11, no. 2, pp. 212-214, (1999).

[138] M. Bachmann, P. A. Besse, H. Melchior, "General self-imaging properties in N × N multimode interference couplers including phase relations", *App. Opt.*, vol. 33, no. 18, pp. 3905-3911, (1994).

[139] M. Blahut, A.Opliski, "Multimode interference structures - New way of passive elements technology for photonics", *Opto-Electronics Review*, vol. 9, no. 3, pp. 293-300, (2001).

[140] R. Ulrich, T. Kamiya, "Resolution of self-images in planar optical waveguides", *J. Opt. Soc. Am.*, vol. 68, no. 5, pp. 583-592, (1978).

[141] R. Ulrich, G. Ankele, "Self-imaging in homogeneous planar optical waveguides", *App. Phys. Lett.*, vol. 27, no. 6, pp. 337-339, (1975).

[142] A. Ferreras, F. Rodriguez, E. G. Salas, J. L. Miguel, F. H. Gil, "Useful formulas for multimode interference power splitter/combiner design", *IEEE Photon. Technol. Lett.*, vol. 5, no. 10, pp. 1224-1227, (1999).

[143] M. R. Paiam, C. F. Janz, R. I. MacDonald, J. N. Broughton, "Compact Planar 980/1550-nm Wavelength Multi/Demultiplexer Based on Multimode Interference", *IEEE Photon. Technol. Lett.*, vol. 7, no. 10, pp. 1180-1182, (1995).

[144] N. Najeeb, Y. Zhang, C. J. Mellor, T. M. Benson, "Design, Fabrication and Demonstration of a 1x20 Multimode Interference Splitter for Parallel Biosensing Applications", *J. Phys. Conf. Ser.*, vol. 679, pp. 1-10, (2016).

[145] D. Ozcelik, J. W. Parks, T. A. Wall, M.A. Stott, H. Cai, J. W. Parks, A. R. Hawkins, H. Schmidt, "Optofluidic wavelength division multiplexing for single-virus detection", *PNAS*, vol. 42, no. 112, pp. 12933-12937, (2015).

[146] S. Nagai, G. Morishima, H. Inayoshi, K. Utaka, "Multimode interference photonic switches (MIPS)", *J. Ligthwave Technol.*, vol. 20, no. 4, pp. 675-681, (2002).

[147] C. H. Lien, H. H. Lin, S. W. Weng, H. J. Wang, W. C. Chang, "A compact photonic switch based on multimode interference with partial index-modulation regions", *Microw. Opt. Technol. Lett.*, vol. 33, no. 3, pp. 174-176, (2001).

[148] P. A. Besse, M. Bachmann, H. Melchior, L. B. Soldano, M. K. Smit, "Optical bandwidth and fabrication tolerances of multimode interference couplers", *J. Ligthwave Technol.*, vol. 12, no. 6, pp. 1004-1009, (1994).

[149] H. Xiao, L. Deng, G. Zhao, Z. Liu, Y. Meng, X. Guo, G. Liu, S. Liu, J. Ding, Y. Tian, "Optical mode switch based on multimode interference couplers", *J. Opt.*, vol. 19, no. 2, pp. 1-6, (2017).

[150] L. Sirleto, G. Coppola, G. Breglio, "Optical multimode interference router based on a liquid crystal waveguide", *J. Opt. A: Pure App. Opt.*, vol. 5, no. 5, pp. 298-304, (2003).

[151] A. V. Mule, R. Villalaz, T. K. Gaylord, J. D. Meindl, "Photopolymer-based diffractive and MMI waveguide couplers", *IEEE Photon. Technol. Lett.*, vol. 16, no. 11, pp. 2490-2492, (2004).

[152] J. M. Hong, H. H. Ryu, S. R. Park, J. W. Jeong, S. G. Lee, E. H. Lee, S. G. Park, D. Woo, S. Kim, B. H. O, "Design and fabrication of a significantly shortened multimode interference coupler for polarization splitter application", *IEEE Photon. Technol. Lett.*, vol. 15, no. 1, pp. 72-74, (2003).

[153] D. Pustakhod, X. Jiang, E.M.V Vliet, K.A. Williams, X.J.M. Leijtens, "Characterization of 3x3 and 4x4 multimode interference couplers in InP generic photonic integration technology", *Proc. IEEE Photonics Benelux Chapter*, pp. 35-38, (2015).

[154] M. Rarajaran, B.M.A. Rahman, T. Wongcharoen, K.T.V. Grattan, "Rigorous characterization of MMI-based photonic device" *Proc. SPIE The International Society for Optical Engineering,* pp. 13-24, (1998).

[155] Q. Lai, M. Bachmann, H. Melchior, "Low-loss 1/spl times/N multimode interference couplers with homogeneous output power distributions realised in silica on Si material", *Electron. Lett.*, vol. 33, no. 20, pp. 1699-1700, (1997).

[156] J. Heaton, R. Jenkins, D. Wight, J. Parker, J. Birbeck, K. Hilton, "Novel 1-to-N way integrated optical beam splitters using symmetric mode mixing in GaAs/AlGaAs multimode waveguides", *App. Phys. Lett.*, vol. 61, no. 15, pp. 1754-1756, (1992).

Conferences

1. L. Civita, R. Asquini, A. d'Alessandro," Simulations of Low Power Switches in LC:PDMS Waveguides for Optofluidic Applications ", International summer school of Photonics, (2016).

2. d' Alessandro, R. Asquini, L. Civita, L. Martini, P. Pasini, C. Zannoni, "LC:PDMS optical waveguides: a new proposal for flexible photonics", 6th Workshop on Liquid Crystals for Photonics, (2016).

3. L. Civita, L. Martini, R. Asquini, A. d'Alessandro," Simulation of Optofluidic LC:PDMS Directional Couplers for Photonic Switching", 3rd Italian-Brazilian Workshop and 12th SICL national Conference, (2016).

4. d'Alessandro, L. Civita, L. Martini, R. Asquini,"Microoptofluidics using PDMS and liquid crystals: fabrication technology and devices", 8th Japanese-Italian Liquid Crystal Workshop, (2016).

5. L. Civita, Luca Martini, Rita Asquini and Antonio d'Alessandro, " Simulation of Optofluidic LC:PDMS Directional Couplers for Photonic Switching", IEEE Xplore, 48th Annual Meeting of the AEIT, (2016).

6. d'Alessandro, R. Asquini, L. Civita, L. Martini, P. Pasini, C. Zannoni, "LC:PDMS optical waveguides: a new proposal for flexible photonics", 6th Workshop on Liquid Crystals for Photonics, (2016).

7. R. Asquini, L. Civita, L. Martini, M. di Domenico, A. d'Alessandro, "Liquid crystal and polymer technologies for optoelectronic tunable and switching devices", Prog. In Electromagnetics Research Symposium, (2017).

8. L. Civita, K. Rutkowska, R. Asquini, A. d' Alessandro "Electrical tuning of optical LC:PDMS waveguides", Proceeding of SIE 49th Annual Meeting, (2017).

9. R. Asquini, L. Civita, L. Martini, K. Rutkowska, T. Wolinski, A. d' Alessandro, "Optoelectronic devices with liquid crystals and PDMS channels", 9th Management Committee Meeting of Cost action IC 1208, (2017).

10. R. Asquini, L. Civita, L. Martini, M. di Domenico, A. d'Alessandro, "Liquid crystal and polymer technologies for optoelectronic tunable and switching devices", PIERS, (2017).

11. R. Asquini, L. Civita, A. d'Alessandro, "Photonic Devices Based on Liquid Crystals for Low Power Applications", PIERS, (2018).

12. R. Asquini, L. Civita, C. Chiccoli, P. Pasini, C. Zannoni, A. d'Alessandro,"Liquid crystals embedded in poly(dimethylsiloxane) photonic devices: modeling and fabrication issues", 9th Italian-Japanese Workshop on Liquid Crystals, (2018).

Journals

1. L. Civita, S. Quaranta, R. Asquini, A. d'Alessandro, "Design of a Multi Mode Interferometer using LC:PDMS technology", *Mol. Cryst. Liq. Cryst.*, article in press, (2019).

2. R. Asquini, C. Chiccoli, P. Pasini, L. Civita, A. d'Alessandro, "Low power photonic devices based on electrically controlled nematic liquid crystals embedded in poly(dimethylsiloxane)", *Liq. Cryst.*, vol. 45, no. 13-15, (2018).

3. R. Asquini, L. Civita, A. d'Alessandro, "Electrical tuning of the LC:PDMS channels", *Phys. Lett. Pol.*, vol. 9, (2017).

4. R. Asquini, L. Civita, L. Martini, A. d' Alessandro, "Design of optical directional couplers made of polydimethysiloxane liquid crystal channel waveguides", *Mol. Cryst. Liq. Cryst.*, vol. 619, no. 1, (2015).

5. A. d'Alessandro, L. Martini, L. Civita, R. Beccherelli, R. Asquini, "Liquid crystal waveguide technologies for a new generation of low power photonic integrated circuits", *Emerging Liquid Crystal Technologies X*, vol. 9384 (2015).

Ringraziamenti

Desidero ringraziare prima di tutto i miei genitori, senza i quali non sarei mai arrivato a questo agognato traguardo, i miei Prof. Antonio d'Alessandro e la Prof.ssa Asquini per il supposto datomi in questi anni, ed tutti altri Professori del quarto piano del DIET: i Prof. Caputo, de Cesare, Olivieri, Balucani e la Prof.ssa Irrera.

In questi anni ho conosciuto molte persone all'interno del dipartimento, alcuni come studenti altri come tecnici. Ognuno di loro, consapevolmente e inconsapevolmente, ha in qualche modo contribuito a farmi arrivare alla fine del mio percorso. Per anzianità vorrei innanzitutto ringraziare il "trio delle meraviglie" Massimo, Rocco e Mario, con le loro discussioni degne di purtroppo tutti aventi un grave difetto, non tifano la squadra fondata nel 1927 a Roma.

Un grazie va sicuramente a Simone C. e un grosso in bocca al lupo per la sua nuova avventura al CERN e al Prof. Antonio M. per i momenti comici passati insieme durante questi anni.

Vorrei inoltre ringraziare in egual misura le persone con cui ho condiviso le esperienze e le attività di laboratorio durante questi anni, che chiamo affettuosamente "principesse" tra cui Valeria, Giulia P., Enrica, Chiara, Costanza e Giulia S., non me ne vogliano le altre studentesse a cui comunque va il mio ringraziamento tra cui Maria Vittoria, Antonia, Claudia, Chiara, Paola. Vorrei inoltre ringraziare tra gli altri Marco, gli "Alessios", Badrul, Andrea, Abdalla, Nicola, Angelo, Simone, Mattia e tutti gli altri che sono passati per la loro tesi nei laboratori del quarto piano.

Una menzione ed una frase apposita in questa tesi di dottorato va sicuramente a Simone Q. "l'alchimista" che mi ha introdotto come sostiene lui nell' "arte dell'elettroplating" da cui ho realizzato i campioni di laboratorio.

Un grazie va poi a Marco, Paolo e Andrea, Fabio e Stefano compagni da sempre sia fuori che dentro l'Università.